Structural Engineering Report No. 180

FINITE ELEMENT ANALYSIS OF COMPOSITE ICE RESISTING WALLS

by

R.A. LINK

and

A.E. ELWI

JUNE 1992

Structural Engineering Report No. 180

FINITE ELEMENT ANALYSIS OF COMPOSITE ICE RESISTING WALLS

by

R.A. Link

and

A.E. Elwi

Department of Civil Engineering

University of Alberta

Edmonton, Alberta

Canada

T6G 2G7

June 1992

ABSTRACT

This thesis presents the results of a study involving the ultimate and post-peak capacity of composite steel-concrete ice resisting walls subjected to transverse and longitudinal loadings. The main application of these composite walls lies in the design of arctic offshore structures subjected to large forces from moving sea ice.

Current design provisions in the Canadian fixed concrete offshore code (CSA S473-M89) require the computation of the ultimate capacity of the wall for strength, and the wall energy absorption (post-peak) characteristics. Currently, several methods exist for computation of the wall ultimate strength. However, nearly all approaches require an estimate of the concrete effectiveness factor, which is not readily available. In addition, no successful method has been derived which addresses the problem of post-peak behavior.

In this study, the finite element method is used to determine both ultimate strength and post-peak capacity of a selected composite wall system. Material nonlinearites in the concrete and steel are considered, and the frictional interface between steel and concrete is modelled. Numerical results are compared with those obtained from experiment for a variety of wall geometries and loading configurations.

ACKNOWLEDGEMENTS

The authors wish to acknowledge the interest and financial support provided by the Centre for Frontier Engineering Research. The authors acknowledge the information provided by the Centre for Frontier Engineering Research on test series CF, TF, and VTT. The work was also supported in part by the Natural Sciences and Engineering Research Council of Canada.

TABLE OF CONTENTS

LIST OF TABLES

LIST OF FIGURES

Figure **Page**

Figure **Page**

Figure **Page**

LIST OF SYMBOLS

A	Actual area loaded by ice.
a	Horizontal projection of shear crack. Also, constraint quantities.
A_0	Reference contact area.
$a_{0,1,2}$	Curve fit constants for Willam-Warnke surface.
A_c	Descending branch area obtained from a uniaxial compressive cylinder test.
$A_{ct,cd}$	Total and descending branch areas, respectively, for concrete in tension or compression.
A_s, B_s	Empirical constants for determining the fracture energy ratio.
b	Wall or specimen width.
$b_{0,1,2}$	Curve fit constants for Willam-Warnke surface.
$c_{0,s}$	Cohesive strength parameters.
C_{ijkl}	Constitutive tensor.
$C_{V,D,T}$	Volumetric, deviatoric, and tangential constitutive moduli respectively.
d	Beam depth. Also, midspan deflection for the analysed walls.
D,E,F	Empirical constants for frictional strength parameter, m_Q.
$d\sigma''$	Inelastic stress increment.
$E_{0,s}$	Initial and secant moduli of a uniaxial stress-strain curve, respectively.
$E_{1,2,3}$	Orthotropic moduli.
E_f	Strain softening modulus.

F	Yield surface.
$f(\mathbf{n})$	Anisotropic weighting factor.
$f'_{c,t}$	Uniaxial compressive cylinder and direct tensile strengths of concrete, respectively.
f_c	Effective concrete "yield" strength.
f_{cb}	Concrete biaxial strength.
$f_{cu,tu}$	Concrete uniaxial compressive and tensile strengths, respectively.
$f_{h1,h2}$	High compression strengths.
F_s	Softening yield surface.
f_y	Steel yield strength.
G_{12}	Shearing modulus.
$G_{f,cr}$	Fracture energy in tensile fracture and compressive crushing, respectively.
$G_f^{I,II}$	Fracture energies for splitting and shear band propagation, respectively.
$h_{1,2}$	Mesh spacings in specified directions "1" and "2".
$h_{c,t}$	Mesh spacings in compression and tension respectively.
k	Hardening parameter.
$k_{t,c}$	Tensile and compressive descending branch decay parameters, respectively.
$m_{0,\Omega,s}$	Frictional strength parameters.
n	Exponent for concrete cylinder curve fit.
N, T	Normal and tangential forces, respectively.

$n_{i,j,k}$	Direction cosines.
p	Ice contact pressure.
Q	Plastic potential surface. Also, global loads calculated from internal stresses.
q	Global displacements.
$r_{1,2}$	Maximum and minimum radii of the deviatoric trace, respectively.
s_{ij}	Deviatoric stress tensor.
u, v	Horizontal and vertical displacements, respectively.
V_u	Shear capacity of reinforced concrete beam.
w	Deformation in the fracture process zone.
α	Concrete effectiveness factor.
α_c	Proportionality constant for concrete cylinder curve fit.
δ_{ij}	Kroenecker delta.
$\Delta_{N,T}$	Accumulated normal and tangential nodal seperations, respectively.
ε_c	Equivalent uniaxial strain when the equivalent uniaxial compressive or tensile strength is reached.
ε_{ij}	Strain tensor.
$\varepsilon_{N,Ti}$	Normal and tangential strain components respectively.
ε_u	Equivalent uniaxial strain. Also, the strain at which the applied stress is zero.

$\varepsilon_{V,D,T}$	Volumetric, deviatoric, and tangential strain components respectively.
ϕ_c	Concrete performance factor.
γ_{12u}	Equivalent uniaxial shear strain.
λ	Constraint forces for interface element. Also, scaling factor for the displacement control method.
λ_{disp}	Relative displacement norm.
λ_{load}	Relative load norm.
μ	Frictional coefficient.
ν	Concrete effectiveness factor.
$\nu_{1,2,3}$	Orthotropic Poisson's ratios.
θ	Angle of similarity.
ρ	Beam reinforcing ratio.
ρ,ξ	Non-dimensional average stress coordinates.
$\sigma_{1,2,3}$	Principal stresses.
$\overline{\sigma}_a$	Average normal stress.
$\sigma_{c,t}$	Equivalent uniaxial compressive and tensile strengths, respectively.
σ_{ij}	Stress tensor.
$\sigma_{N,Ti}$	Normal and tangential stress components respectively.
σ_{ref}	Ice reference stress.
$\sigma_{V,D,T}$	Volumetric, deviatoric, and tangential stress components respectively.

$\sigma_{x,y}$	In-plane stresses in the horizontal and vertical directions, respectively.
σ_z	Out of plane stress.
τ_{12}	Shear stress.
$\bar{\tau}_a$	Average shear stress.
τ_{xy}	In-plane shear stress.
$[K]$	Stiffness matrix.
$[C]$	Constraint matrix.
$\{\Delta q\}^{I,II}$	Displacement control displacement vectors.
$\{R^*\}$	Displacement control reference load vector.
$\{\}^i$	Vector at iteration i.
$()^i$	Scalar quantity at iteration i.
$[]^i$	Matrix at iteration i.
$\{\}_{g,l}$	Vector in global and local space, respectively.
$[]_{g,l}$	Matrix in global and local space, respectively.

1.0 INTRODUCTION

1.1 General

The idea for using composite steel and concrete walls to resist ice loads was introduced in the late 1970's by Hitachi Shipbuilding and Engineering Company (Adams, 1987). It was found that the composite walls exhibited a high degree of strength and ductility, which are desirable characteristics for exterior walls on offshore structures.

Composite construction utilizing exterior steel plates with concrete infill was found to have many desirable attributes in comparison with all steel and all reinforced concrete construction. Sandwich composites can utilize thin steel members for construction, since local buckling of the steel is restrained by the concrete, resulting in easier fabrication and better quality control than all steel construction. Sandwich composites are fabricated with the steel plates on the exterior faces of the wall, which minimizes the problem of steel congestion that is prevalent in offshore structures constructed of reinforced concrete. Other features, such as ease of connections between structural members, increased load carrying efficiency due to concrete confinement from the steel plates, and the use of automation and advanced shipyard construction techniques, makes composite ice resisting walls competitive with other forms of construction (Gerwick and Berner, 1987).

Since then, a significant amount of research effort has been invested in determining the structural behaviour of these composite walls. A major part of this research has been conducted by the Center for Frontier Engineering Research (referred to in the following as C-FER), which has been investigating the behaviour of composite ice resisting walls since 1985. Initial work focused on the behaviour of studded steel plates with concrete infill (O'Flynn, 1987). Later work concentrated mainly on the one-way wall system shown in Figure 1.1. The two steel forming plates are connected along their length by a series of vertical diaphragm plates. Concrete infill is then placed in the cells between the diaphragm plates. The wall thicknesses are in the order of 1.0 m, and spans are in the order of 6.0 m. Extensive testing indicates that significant strength and ductility are available from this form of construction.

Several analytical techniques have been developed to predict the ultimate strength of this construction form. These techniques vary from the basic lower bound truss models (Rogowsky and MacGregor, 1983) to empirical equations based on dimensional analysis (Adams and Zimmerman, 1987). However, all methods suffer from lack of generality, which is discussed further in Chapter 2. In addition, since the governing Canadian design code for concrete offshore structures (CSA S474-M1989) requires that an estimate of member ductility be made, the difficult evaluation of post-peak strength must be made. No existing analytical technique is yet available to assess post-peak strength or ductility.

Composite ice walls generally have two distinct modes of failure. The first mode, denoted as flexural, involves significant yielding of the tension plate, and crushing occurs in the concrete at the point of maximum bending moment. The second mode, herein referred to as shear, involves crushing of concrete struts which carry load into the support region. The latter failure mode is of most interest here, since many experimental investigators have reported failures of this type, and no significant analytical effort has been made to investigate this failure mode.

In this study, the feasibility of using the finite element method for the evaluation of both ultimate strength and post-peak ductility is investigated. Constitutive models for both concrete and the interface between steel and concrete are developed and implemented in a finite element program. Numerical models are developed, analysed, and the resulting behaviour compared with results obtained from C-FER's extensive testing database.

It should be noted, herein, that a large portion of C-FER's test results are confidential. However, the writer is grateful for the open cooperation of C-FER in permitting the writer to present the test results of series CF, TF and VTT in this study.

1.2 Objectives of Study

The objectives of this study are as follows:

a) To conduct a literature review of all significant work done which pertains to composite ice resisting walls including design codes, testing, and classical and numerical analysis.

b) To identify the important factors which must be considered in the numerical modelling of the structural behaviour of composite ice resisting walls, and to develop a finite element model which incorporates these factors.

c) To verify the finite element model by analysis of actual tested wall configurations, and compare the numerical results to the experimentally obtained results.

d) To identify future work which is required to accurately predict the structural behaviour of composite ice resisting walls.

1.3 Organization of Thesis

This thesis is organized as follows. Chapter 2 is a literature review of all significant work performed pertaining to composite wall analysis and design, as well as some of the viable constitutive modelling techniques for concrete. Chapter 3 summarizes the important factors which must be included in the analytical model, and presents the development of the concrete constitutive model. In addition, the theory for both the interface, steel, and displacement control models are presented in Chapter 3. Chapter 4 includes the development of the finite element models, and Chapter 5 contains the comparison of analytical to experimental results. Finally, Chapter 6 summarizes the findings from the work performed in this thesis, and identifies future research that should be performed.

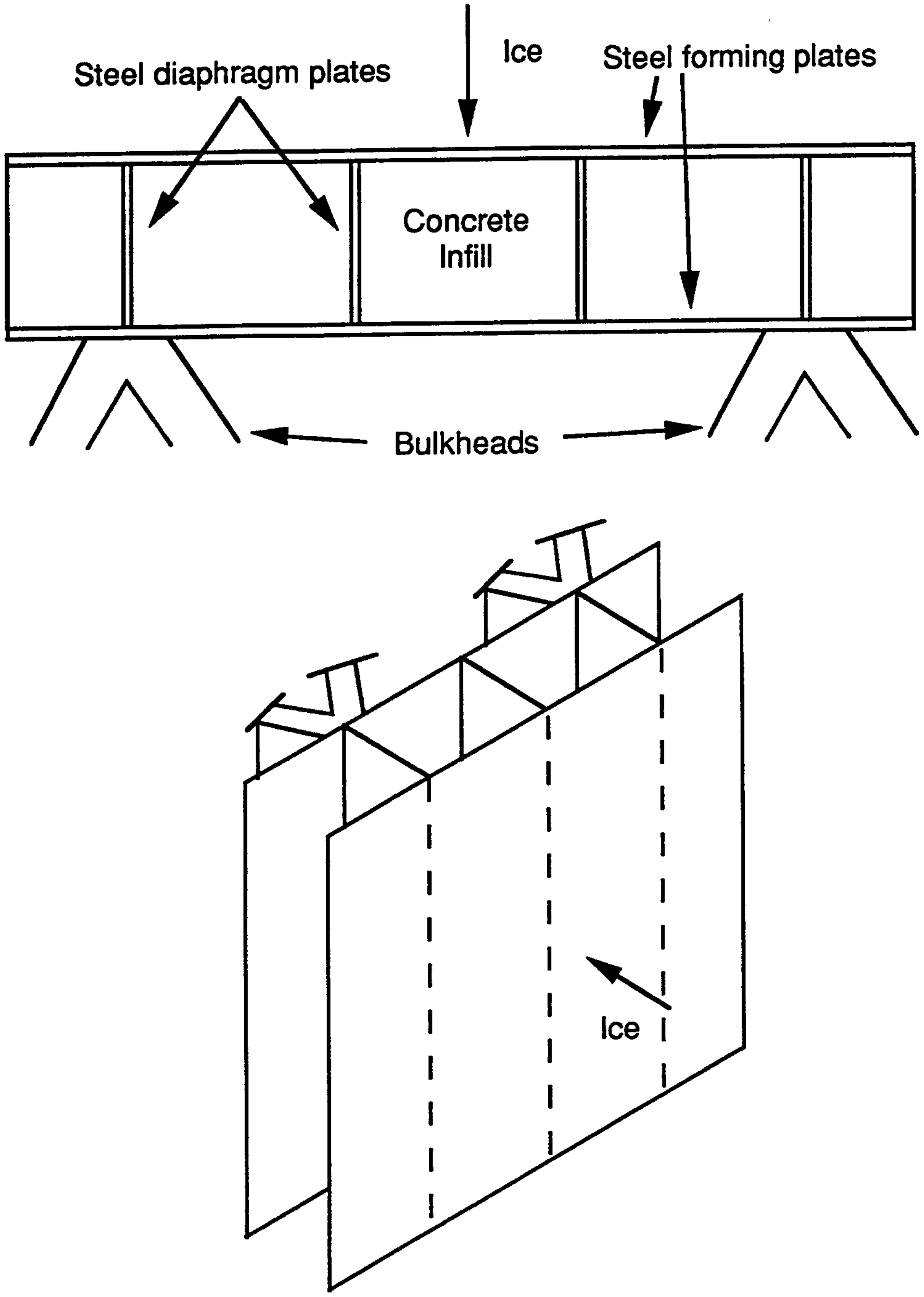

Figure 1.1 C-FER composite wall system

2.0 LITERATURE REVIEW

2.1 General Background

The design and analysis of composite walls to resist ice loadings in Canada is governed by CSA Standard S473-M1989 - Steel Structures - Part III of the Code for the Design, Construction, and Installation of Fixed Offshore Structures. However, the provisions for composite wall design contained here are general and vague in nature. More applicable design information was found in CSA S474-M1989 - Concrete Structures. The structural design considerations of interest here include the wall section forces and resistances, and the system ductility.

Wall section forces are determined through the use of Clause 8.2. Clause 8.2.1 states that a linear elastic analysis may be used to determine the sectional forces, with the provision in Clause 8.2.4 that second order (large deformation) effects be included where applicable. The secant modulus of concrete and the gross cross sectional area are recommended for use in the elastic analysis (Clause 8.2.1), with the option of reducing stiffness values due to cracking and other nonlinear effects.

Clause 8.3 deals with the determination of factored sectional resistances. Clause 8.2.1 of S474-M1989 states that the sectional forces throughout the structure may be determined through the use of an elastic analysis. The section at which these forces occur must then be checked for ultimate strength capacity. Two methods are given for ultimate strength checks; the standard design methods of CSA CAN3-A23.3 in Clause 8.3.2, and the more detailed design methods given in Clause 8.3.3. Clause 8.3.3 is the more economical design, since slab or shell action is considered, but is often more difficult to apply. This approach often requires the use of a finite element analysis to determine the sectional forces at appropriate checking points. The combined effect of all sectional forces must then be considered in checking the sectional strength.

Clause 8.4 considers the evaluation of system ductility in the structure. A typical offshore structure is designed to withstand loading from frequent ice events which occurs once every 100 years (probability of exceedance of 0.01) without significant permanent damage. Clause 8.4 requires that the structure be able to resist rare environmental loading events with a return period of 10000 years without a total collapse. Note that significant permanent damage may occur from these loading magnitudes. In order that structural integrity is maintained for this event, requirements are placed upon system ductility in two ways. The first requirement is to design the structure so that global collapse of the damaged structure does not occur after the event has occurred (Clause 8.4.1). This means that the damaged structure continues to stand under the action of permanent loadings (eg. gravity and hydrostatic loads). The second requirement ensures that individual members which could be overloaded are provided with detailing which maintains adequate energy absorption capabilities through large deformations. This provides additional energy dissipation while local areas of the structure are failing, which contributes to the overall protection of the structure. Clause 8.4.4 states that adequate energy absorption is defined as the ability of the members to sustain six times the yield deflection while maintaining 50% of the yield load. The yield load is defined as the ultimate load attained by the structure, and the yield deflection is defined as the deflection obtained at the intersection of the yield load and a line drawn from the origin with a slope equal to the initial tangent stiffness. Figure 2.1 illustrates the application of Clause 8.4.4.

For composite systems involving steel and concrete sandwich panels, the determination of member resistances and ductilities has been, almost exclusively, on the basis of experimental data. This is because numerical techniques developed for predicting the ultimate strength and ductility of composite wall systems have not been entirely successful. The difficulty in predicting the ultimate strength lies in the prediction of the failure mode of the wall, whether flexural or shear-compression. The evaluation of post-peak strength and ductility is extremely difficult, and no attempt has been made to predict composite wall post-peak response.

Considering the above discussion, it is the writer's opinion that a sophisticated numerical technique is necessary to evaluate composite wall strengths and ductilities. The finite element method is ideally suited for these predictions. Both pre- and post-peak structural response can be easily incorporated into the finite element model. Once confidence through comparison with experimental results is obtained, the need for expensive testing would be reduced significantly.

This chapter is a summary of the significant work that has been performed in composite ice wall technology. For the purposes of clearly defining the loads that are resisted by ice-resisting walls, a brief summary of ice loading is presented in Section 2.2 Section 2.3 is a brief summary of significant testing programs performed over the last ten years. Section 2.4 examines the various analytical techniques used to predict wall ultimate strengths. Section 2.5 summarizes the finite element analytical work done on composite ice walls. Finally, as an introduction to Chapter 3, critical reviews of the most recent concrete constitutive models are contained in Section 2.6.

2.2 Ice Loading

This section serves as a brief overview of the approach adopted for computing design ice loads in CSA S471-M1989 - General Requirements, Design Criteria, the Environment, and Loads, which serves as the governing design standard for ice load calculation in Canada. The above mentioned code closely follows the recommendations made by Sanderson (1988) on design ice load calculation.

Two basic types of ice loads are considered in offshore design: static and dynamic.

Static loads refer to loads applied by ice initially in stationary contact with the structure. Loading occurs as a result of ice movement due to natural driving forces applied to the ice. Typical examples include winter landfast ice conditions, in which a structure is surrounded by uniform first-year ice, and "winter blocking" conditions, where a large ice feature becomes lodged against the structure. Wind and current drag generate the loads which act on the offshore structure.

Dynamic loads refer to the state in which the ice feature is not initially in contact with the structure, but arrives, and strikes it with significant velocity. Examples include impact by multi-year ice floes, and collisions by icebergs or ice islands.

Calculation of ice loads involves the extensive use of probablistic methods, since ice contact pressure and thickness have been experimentally determined to be random variables. A general procedure is proposed by Sanderson (1988), and proceeds as follows:

1) Determine the number of ice loading events of the specified type which will occur in a specific year.

2) Determine an ice thickness probability distribution by using available ice thickness data and the information from 1).

3) Determine a peak contact pressure probability distribution. A normal distribution is generally adopted.

4) From 2) and 3), for a given contact area, determine a contact force probability distribution. From this distribution, it is possible to obtain design loads for a given exceedence level.

Points 3 and 4 require more elaboration. The peak contact pressure generated by ice is found to be highly variable, and is dependent upon the loaded area. From an accumulation of pressure versus contact area data, Sanderson (1988) proposed the following relationship between pressure and contact area

$$p = \sigma_{ref}\sqrt{\frac{A}{A_0}}, \qquad [2.1]$$

where σ_{ref} is the reference stress for a reference contact area, A_0, of 100 m^2, and A is the actual loaded area. From statistical analysis of large scale pressure measurements, the reference stress, σ_{ref}, has been determined to be 0.92 MPa, with a standard deviation of 0.45 MPa. These quantities are assumed to apply for global structural loading only. For highly localized ice loads, Sanderson (1988) suggests increasing the pressure value, p, to account for uncertainty in the occurence frequency of such conditions.

Once the probability distribution curve has been obtained for the given ice event, the loads are computed based on a specified level of exceedence. The Canadian standard CSA S471-M1989 specifies exceedence levels of 10^{-2} for frequent ice events, and 10^{-4} for rare ice events. Frequent events are defined in S471 as events which have an annual rate of occurence greater than 0.5/year. An important example is the loading caused by first year ice, which may occur up to several thousand times per year. Rare events are defined as events which have an annual rate of occurence less than 0.5/year. A typical example may be iceberg loading.

2.3 Testing Programs

This section serves only as a brief overview of the existing test programs performed in the last ten years. A much more comprehensive review is available in Kennedy and Cheng (1987).

Over the last ten years, over 160 composite wall specimens of various configurations have been tested as one or two span beams under a variety of loading patterns (Kennedy and Cheng, 1987). Structural configurations included shear connectors on top and bottom plates, vertical diaphragm plates, and longitudinal steel stiffener plates. Span to depth ratios varied from 2 to 10.

Composite wall failures typically occurred as a result of either flexural or tied arch behaviour. Flexural failures were initiated by the yielding of the tension plate, which was followed by localized crushing in the maximum moment region. Figure 2.2 illustrates a typical flexural failure. Tied arch failures occurred as a result of localized crushing of a compressive strut in the wall. This type of failure is illustrated in Figure 2.3.

In most of the test programs, post-failure ductility was either not measured, or not reported. Notable exceptions were the test program of C-FER, which is mentioned in more detail in Chapter 4, and the program carried out by Kennedy and Cheng (1987). In the C-FER tests, failure occurred as a result of shear compression failure at the support region in nearly all of the tests. The span to depth ratios in the tests varied from 4 to 6, which is near the limits of deep beam behaviour (MacGregor, 1988). In the Kennedy and Cheng tests, failure occurred as a result of plate tearing, which was induced by membrane action as the composite wall experienced large deformations. The span to depth ratios of these tests were fairly large, varying from 18 to 30.

2.4 Analytical and Design Methods

There are currently three different methods commonly in use for predicting the strength of composite ice resisting walls:

a) Reinforced concrete design methods

b) Empirical design equations based on curve fits of experimental data

c) Plasticity methods, both lower and upper bound

Traditional reinforced concrete design equations contained in CSA A23.3-M84 for flexural/shear members such as beams involve checking the capacity of the section for both bending moments and shear forces. The CSA Standard S474-M1989 code for concrete offshore structures further considers the combined effects of coincidental bending, shear, and axial loading on section capacity. The flexural capacity method assumes the existence of strain compatibility between the tensile reinforcing steel and the concrete, and that the beam is slender so that no deep beam action exists. The former assumption is certainly not true in the case of concrete sandwich panels, since significant slip and separation occurs between the steel plate and concrete infill. The latter assumption is not always true, since deep beam action becomes important for span to depth ratios less than 5 (MacGregor, 1988). Proposed full scale designs tend to be even stockier. In addition, it was concluded by the Center for Frontier Engineering Research (Stephens and Zimmerman, 1990) that the simplified method for shear contained in CSA A23.3-M89 was inappropriate for use with composite members. Therefore, it can be seen that traditional reinforced concrete design methods are inapplicable to the design of composite sandwich panels.

Two empirical design equations have been proposed by Zsutty (1968), and the Center for Frontier Engineering

Research (Adams and Zimmerman, 1987). These equations were derived by applying the techniques of dimensional analysis and statistical regression to multiple sets of test data. The equations calculate the shear capacity, V_u, of a member which fails along a diagonal crack with a horizontal projection, a, as shown in Figure 2.4. The simplified C-FER equation is written as follows:

$$V_u = \frac{1.35\, f_c^{'}\, b\, d\, \rho}{(a/d)^{1.3}}, \qquad [2.2]$$

where $f_c^{'}$ is the uniaxial cylinder compressive strength, and ρ is the mechanical reinforcing ratio. The dimensions b and d represent the wall width and depth respectively (see Figure 2.4).

Although potentially useful in the range of parameters tested, the applicability of these equations outside that range is unknown, and the effects of changes in loading or structural configuration (eg. in-plane loadings, studs, multiaxial stress states) is also unknown. Further testing is required to ascertain these effects. In addition, the empirical approach provides no visualization of the flow of forces or the mechanism of failure.

Lower bound plasticity methods include the strut and tie models recommended by CSA A23.3-M84, and used by other authors (Rogowski and MacGregor, 1986, O'Flynn, 1987) to predict the ultimate strength of deep flexural members. The lower bound plasticity models assume the existence of a statically admissible stress field in the member. The internal stresses in the member do not exceed the yield strength of the material anywhere, and the material is assumed to be of sufficient ductility to develop the specified stress field. If these conditions are met, then a lower bound estimate of the load is obtained. Figure 2.5 shows a typical strut and tie model for a concrete corbel. The concrete strut carries the vertical load, P, and the top reinforcing steel carries the horizontal component of the concrete strut.

Similar models can be developed for reinforced concrete beams and composite wall systems. However, there are three main problems with using strut and tie models for predicting ultimate strengths of composite walls. Firstly, since the model represents a lower bound of the exact failure load, undue conservativity can be realized by an incorrect selection of the strut and tie model. Secondly, due to the condition of enforcing a statically admissible stress field, the reinforcing steel must be at the centroid of the biaxially confined concrete, termed the "nodal zones". This is usually not the case for a composite sandwich panel, where the steel is on the outside of the concrete. Finally, for lower bound plasticity models, the concrete and steel is assumed to be rigid plastic material. Since concrete is not rigidly plastic by nature, the concrete "yield" strength, f_c, is usually defined as the uniaxial concrete strength, f'_c, multiplied by a reduction factor to account for the lack of ductility:

$$f_c = \nu f'_c. \qquad [2.3]$$

The quantity ν, termed an "effectiveness" factor, attempts to replace the brittle concrete stress strain curve with that of a ductile material (see Figure 2.6). The effectiveness factor is influenced by many variables, such as concrete confinement due to plane strain conditions, tensile steel running through the strut, etc. Uncertainty in the effectiveness factor makes it difficult to estimate the design concrete strength.

Upper bound plasticity methods for concrete sandwich panels include the diagonal crack mechanism models developed originally for concrete beams with no shear reinforcement by Nielsen and Braestrup (1978), and subsequently modified by Kemp and El-Safi (1982). The upper bound plasticity methods assume a kinematically admissible failure mechanism for the member. Energy considerations are then used to determine the upper bound failure load. The assumed failure mechanism is a diagonal crack which extends from the support region to the top of the concrete beam, which is shown in Figure 2.7. In the

Nielsen and Braestrup model, discussed here for brevity, the bottom concrete piece is assumed to translate in a direction denoted by the displacement vector v in Figure 2.7. It was found from energy considerations that the reinforcing ratio had a significant influence on the shear strength of the beam. If the reinforcing ratio is sufficiently high, it would force the bottom concrete piece to translate vertically, and the longitudinal steel would have no influence on the shear strength of the beam. Kemp and El-Safi (1982) modified the failure mechanism by including rotations of the end blocks, and Stephens and Zimmerman (1989) included the effects of in-plane loads applied at the end of the beam. All three investigators claimed good correlation with experimental results.

The upper bound plasticity methods seem to show the most promise in predicting ultimate strengths of composite ice walls. However, their applicability is far from general, especially for two way behaviour such as slab assemblies. Also, the effectiveness factor is used in upper bound theory as well as lower bound theory, and, for reasons mentioned above, makes the determination of design compressive strength difficult.

It is also noted here that there is no particularly successful analytical tool available at present which evaluates the post-peak strength of composite ice resisting walls.

2.5 Finite Element Analyses

Although extensive work has been performed regarding finite element analysis of reinforced concrete, relatively little effort has been placed into finite element analysis of concrete sandwich panels. A handful of investigators have examined the response of these composite members in the pre-peak response region. No investigation regarding the post-peak behaviour of composite ice walls has been undertaken.

Perhaps the most significant finite element analyses of sandwich panels were performed by Matsuishi et al. (1978), who analysed beam sandwich specimens consisting of top and bottom plates fastened together by a number of vertical stiffeners spaced at regular intervals. An elastic plastic constitutive model was adopted for the concrete, and the interface between the steel and concrete was simulated by use of a spring linkage element. Good correlation was observed between experiment and analysis for load-deflection and ultimate load predictions. As well, cracking patterns were similar to those observed experimentally. The observed failure was in flexure, and no post-peak response was reported for either experiment or analysis. Similar analyses were conducted by Matsuishi and Iwata (1987) on a composite wall configuration which included longitudinal stiffeners. Again, good correlation was observed between experiment and analysis. The failure was also flexural.

Bangs (1988) performed a nonlinear analysis of composite ice walls tested by Matsuishi et al. (1978) and Nojiri and Koseki (1986). The concrete was idealized as elastic plastic material with a tension cutoff, and perfect bond was assumed between steel and concrete. The analysis results were similar to those of the test results, but, again, the failure was flexural in nature.

Other crude approximations using linear elastic concrete models have been reported by Corder and Wang (1990), and Bangs and Machemehl (1989).

It is noted here that no finite element analysis was reported that was able to simulate a shear compression failure in a composite ice wall, even though many test results were reported in which this was the observed failure mode.

2.6 Concrete Constitutive Models

An important aspect of predicting the structural behaviour of composite ice walls using the finite element method is the use of an appropriate concrete constitutive model. For reasons explained in Chapter 3, the model must be able to consider the three dimensional constitutive response of concrete. In order to predict response in the post-failure region, appropriate softening rules must be utilized. The model should also be robust in nature ie. numerical instability should be minimized.

A large number of concrete constitutive models have appeared in the last 15 years. Many models appeared for use with reinforced concrete, and some were suited to the analysis of unreinforced concrete in tension. However, there were few models capable of simulating the three dimensional constitutive response of unreinforced concrete in both the pre- and post-peak regions with considerable numerical stability.

Concrete constitutive models can be divided into two major categories: smeared crack models, and discrete crack models. The former is suited to identification of the general behaviour of the structure, while the latter is suited to following the history of certain major discrete crack propagation. In this study, the smeared crack approach is adopted.

A large variety of constitutive models have been published in this category. Historically, orthotropic and hypoelastic models (Darwin and Pecknold, 1974, Elwi and Murray, 1980) have been and continue to be the most popular approach. Their popularity stems from simplicity and the ability to account for the more recent advances regarding fracture energy, nonlocal effects, etc. Other models such as elastic plastic models are making a recent comeback (Pramono and Willam, 1989, De Borst, 1984), and appear to be quite promising. In addition, the microplane model advocated by Bazant (1984) is notable because of the micromechanical treatment of stresses and strains.

The work presented in this report is based on an orthotropic model built on the equivalent uniaxial strain concept advocated by Darwin and Pecknold (1974) and used successfully by Elwi and Murray (1980), Link et al. (1988), and Link and Elwi (1990). A full development of the model is presented in Chapter 3. However, in this section, two of the most recent generalized models are reviewed. These include the microplane model proposed by Bazant and Prat (1988), and an elastic-plastic model based on fracture energy considerations (Pramono and Willam, 1989).

2.6.1 Microplane Model

The microplane model represents a micromechanics approach to modelling concrete behaviour. Originally presented by Bazant (1984), the fundamental assumption is that the stress-strain relation can be specified independently on various planes in the material, assuming that the strain components on the plane are the resolved components of the strain tensor. The constitutive behaviour of each plane is governed by the volumetric, deviatoric, and tangential components of total strain ε_V , ε_D, and ε_{Ti} respectively. The tangential component of strain, ε_{Ti}, is a strain vector on the tangent plane to the normal component, ε_N. The normal and tangential components of strain are shown in Figure 2.8.

The total volumetric, deviatoric, and tangential stress components σ_V, σ_D, and σ_{Ti} are assumed to be functions of the total strain components

$$\sigma_V = C_V\varepsilon_V, \tag{2.3a}$$

$$\sigma_D = C_D\varepsilon_D, \tag{2.3b}$$

$$\sigma_T = C_T\varepsilon_T. \tag{2.3c}$$

Here, σ_T and ε_T are the magnitudes of the tangential stress and strain vectors, σ_{Ti} and ε_{Ti}, respectively. Differentiating Equations 2.3, the incremental constitutive relationship for the microplane is formed as

$$d\sigma_V = C_V d\varepsilon_V + \varepsilon_V dC_V \tag{2.4a}$$

$$d\sigma_D = C_D d\varepsilon_D + \varepsilon_D dC_D \tag{2.4b}$$

$$d\sigma_T = C_T d\varepsilon_T + \varepsilon_T dC_T \tag{2.4c}$$

The second term on the right hand side in Equations 2.4 represents stress increments due to inelastic behaviour, and can be denoted as $-d\sigma_j''$, where j is a stress identifier which is either V, D, or T for volumetric, deviatoric, or tangential respectively.

Using the principle of virtual work, it is possible to relate the work done on the microscale to the macroscopic work as

$$\frac{4\pi}{3} d\sigma_{ij} \delta\varepsilon_{ij} = \int_S (d\sigma_N \delta\varepsilon_N + d\sigma_{Ti} \delta\varepsilon_{Ti}) f(\mathbf{n}) \, dS. \qquad [2.5]$$

The surface integral in Equation 2.5 represents the integral over a unit sphere. The quantity $f(\mathbf{n})$ is a weighting function to account for initial anisotropy in the material. This function is equal to 1 in the case of isotropic material.

The derivation for the incremental constitutive relationship is given in detail in Bazant and Prat (1988). Using Equation 2.5 in conjunction with the constitutive relationships given in Equations 2.4, and the definitions of the microplane strain (shown in Figure 2.8), the following constitutive relationship is obtained

$$d\sigma_{ij} = C_{ijkm} d\varepsilon_{km} - d\sigma''_{ij}, \qquad [2.6]$$

where

$$C_{ijkm} = \frac{3}{2\pi} \int_S \Big((C_D - C_T) n_i n_j n_k n_m + \frac{1}{3}(C_V - C_D) n_i n_j \delta_{km} \qquad [2.7]$$
$$+ \frac{1}{4} C_T (n_i n_k \delta_{jm} + n_i n_m \delta_{jk} + n_j n_k \delta_{im} + n_j n_m \delta_{ik}) \Big) f(\mathbf{n}) \, dS,$$

and

$$d\sigma''_{ij} = \frac{3}{2\pi}\int_S \left(n_i n_j d\sigma''_N + \frac{1}{2}(n_i\delta_{rj} + n_j\delta_{ri} - 2n_i n_j n_r)\, d\sigma''_{Tr}\right) f(\mathbf{n})\, dS. \qquad [2.8]$$

The subscripted "n" quantities are the components of the microplane unit normals, and δ_{ij} is the Kronecker delta. Thus, the macroscopic constitutive response of concrete is equivalent to the summation of the constitutive response on all microplanes.

Bazant and Prat (1988) assumed exponential forms of the constitutive moduli C_V, C_D, and C_T as a decaying function of their corresponding strains. The decay coefficients were obtained from curve fitting results of multiaxial tests. Good correlation was obtained between analysis and experiment. Further implementation of a nonlocal softening model into the microplane model was performed by Bazant and Ozbolt (1990).

Although the microplane model shows good promise for general multiaxial simulation of concrete constitutive response, much more development work needs to be undertaken. The decay parameters used to determine the constitutive moduli are not calibrated sufficiently against macroscopic strength values (eg. compressive and tensile strengths) and no attempt is made by Bazant in this area. The spherical integrals in Equations 2.7 and

2.8 require the use of several integration points on the hemisphere per Gauss point, which increases solution time dramatically. These shortcomings make the microplane model unwieldy for the analysis of general concrete structures. Indeed, the writer is not aware of any publications which utilize the microplane model to analyse full scale structures.

2.6.2 Elastic Plastic Fracture Energy Model

The elastic plastic fracture model developed by Pramono and Willam (1989) attempts to incorporate the mode of failure into the determination of descending branch properties by the use of fracture mechanics. The model incorporates isotropic hardening and softening rules, using a modified form of the failure criteria developed by Leon (1936), expressed as

$$F(\sigma_1,\sigma_3,k) = \left[(1-k)\frac{\sigma_1^2}{f_c'^2} + \frac{\sigma_1-\sigma_3}{f_c'}\right]^2 - k^2 m_0 \frac{\sigma_1}{f_c'} - k^2 c_0, \qquad [2.9]$$

where σ_1 and σ_3 are major and minor principal stresses, k is a hardening parameter which varies in value from 0 to 1, c_0 is a cohesion parameter which assumes a value of 1.0 at peak stress, and m_0 is a frictional strength parameter which is expressed in terms of the material cohesion, c, as

$$m_0 = \frac{c f_c'^2 - f_t'^2}{f_t' f_c'}. \qquad [2.10]$$

Equation 2.9 represents a closed surface which expands uniformly for hardening. The authors claim that the performance of the constitutive model is extremely sensitive to the existence of non-associative flow behaviour. A plastic potential function, Q, is proposed of similar form to the failure criterion, F

$$Q(\sigma_1, \sigma_3, k) = \left[(1-k)\frac{\sigma_1^2}{f_c'^2} + \frac{\sigma_1 - \sigma_3}{f_c'} \right]^2 - k^2 m_Q \frac{\sigma_1}{f_c'} - k^2 c_0, \qquad [2.11]$$

where the frictional strength parameter, m_Q, is expressed as a function of the major principal stress, σ_1, as

$$\frac{\partial m_Q}{\partial \sigma_1} = D \exp\left(E\left(\frac{\sigma_1 + f_t'}{f_c'} \right) \right) + F. \qquad [2.12]$$

The quantities D, E, and F are empirical constants obtained from curve fits of test data.

Softening initiates in the model when the hardening parameter, k, reaches one. The softening surface, F_s, reduces to (setting k equal to one in Equation 2.9)

$$F_s(\sigma_1, \sigma_3) = \left[\frac{\sigma_1 - \sigma_3}{f_c'} \right]^2 - m_s \frac{\sigma_1}{f_c'} - c_s, \qquad [2.13]$$

where m_s and c_s are the frictional strength parameter and cohesion in the softening region. Values are chosen for m_s and c_s such that the failure surface decreases in size in a region defined by two transitional points. The transitional points denote the hydrostatic stress which is necessary to change the mode of failure from brittle to ductile (plastic). These transitional points are shown in a deviatoric plot in Figure 2.9. At a cohesion value of zero, only frictional resistance is mobilized, and the surface collapses to that of a granular material with zero cohesion (see Figure 2.9).

The rate of softening is governed by a material strain softening modulus, denoted E_f. Since macroscopic softening is a structural property rather than a continuum property, equivalent continuum concepts must be utilized in order to avoid mesh non-objectivity. The strain softening modulus is then a function of the compressive shear band spacing, h_c. The approach of Bazant and Oh (1983) is adopted for hydrostatic tension. In compression, the authors claim that compressive failures are due to the result of shear band formation, therefore, the fracture energy release rate for shear, G_f^{II}, must be included in evaluating E_f for compression. From the equivalence of strain energy in splitting compression, an expression is derived relating the shear band spacing in compression, h_c, to the tensile band spacing in tension, h_t

$$h_c = \frac{G_f^{I}}{G_f^{II}} h_t . \qquad [2.14]$$

The ratio of fracture energies in Equation 2.14 is assumed to be a function of the degree of confinement. This ratio is expressed as

$$\frac{G_f^{II}}{G_f^{I}} = A_s\left(\frac{\sigma_1}{f_c'} - \frac{f_t'}{f_c'}\right)^4 + B_s\left(\frac{\sigma_1}{f_c'} - \frac{f_t'}{f_c'}\right)^2 + 1, \qquad [2.15]$$

where A_s and B_s are empirical constants determined from confinement tests. The overall effect of Equation 2.15 is to decrease the effective shear band spacing, h_c, which will decrease the slope of the compressive descending branch, E_f. This results in a more ductile (plastic) failure as the confinement increases.

Pramono and Willam (1989) compared analytical results of a series of concrete cylinders subjected to varying levels of confinement. Good general agreement was found between experiment and analysis. The mesh used for the model was not reported, and the authors did not mention whether any parametric studies were performed regarding mesh objectivity.

The constitutive model shows good promise in analysing structures which undergo compressive strain softening, since a rational procedure was used to incorporate failure modes in the model. However, the concept of isotropic hardening and softening in concrete seems dubious. This would imply no compressive strength in any direction after the tensile strength decreased to zero, which does not make physical sense. Since the model is relatively new, it has not been used to analyse any full scale structures, which makes it difficult to evaluate in terms of solution stability.

To summarize, the microplane model derived by Bazant and Prat (1988) is unwieldy to use because of the lack of calibration of microproperties to the macroscale and the excessive computational effort required, and the elastic plastic fracture model reported by Pramono and Willam (1990) has dubious assumptions regarding softening and hardening. Both models have not been extensively used in the analysis of full scale structures, making the evaluation of solution stability difficult.

As mentioned in the introduction, the constitutive model required should be able to consider the effects of triaxial stresses in both the hardening and softening ranges. The model must also be numerically stable, and simplicity is an added benefit. It is felt that the hypoelastic constitutive model presented in Chapter 3 meets these requirements.

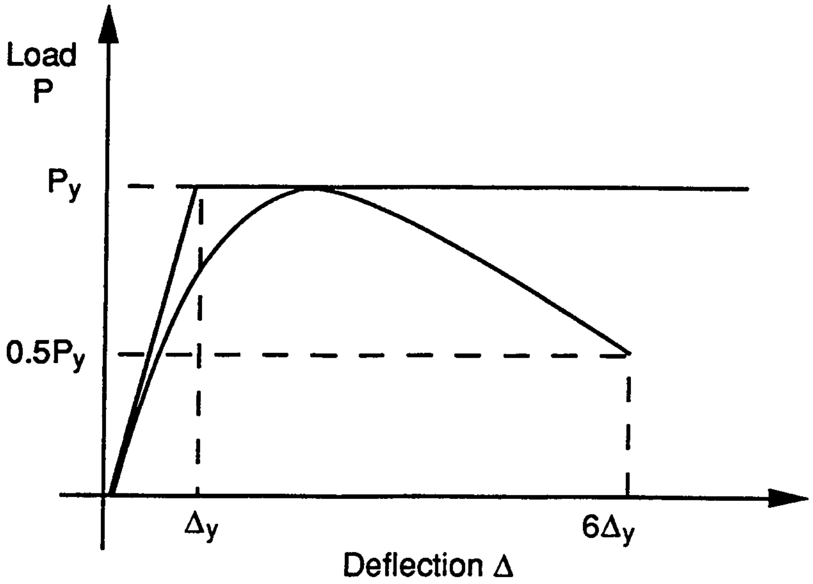

Figure 2.1 Application of Clause 8.4.4

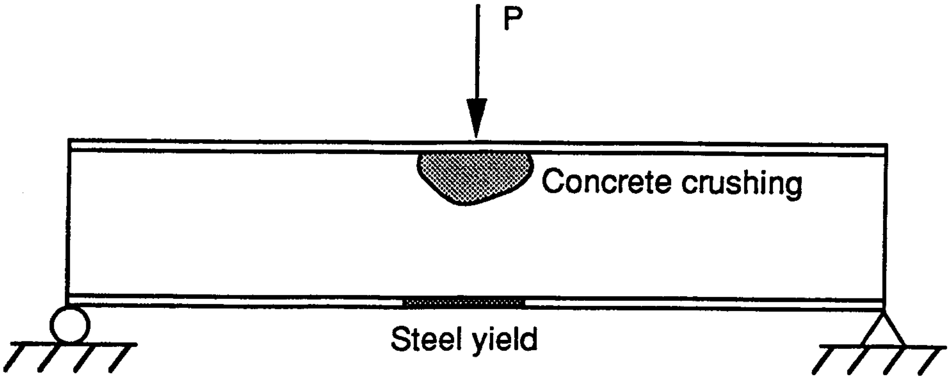

Figure 2.2 Flexural failure illustration

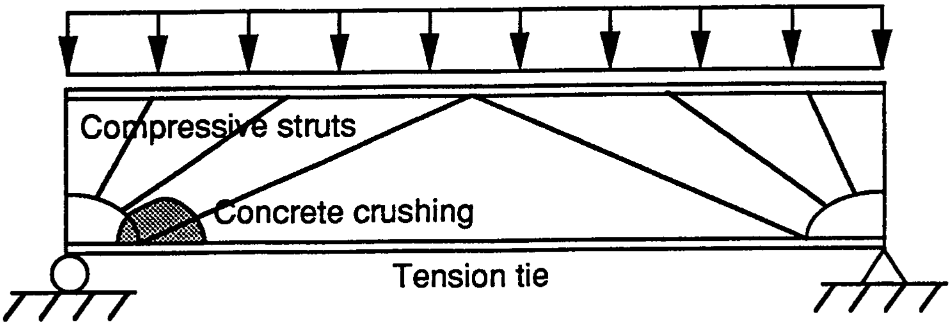

Figure 2.3 Shear compression failure (tied arch)

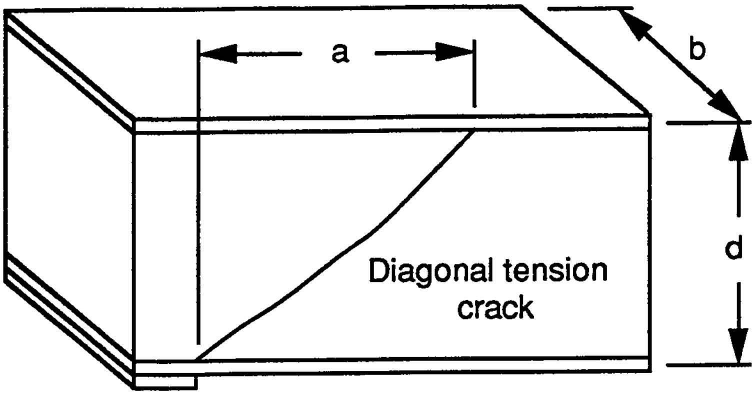

Figure 2.4 Shear failure convention

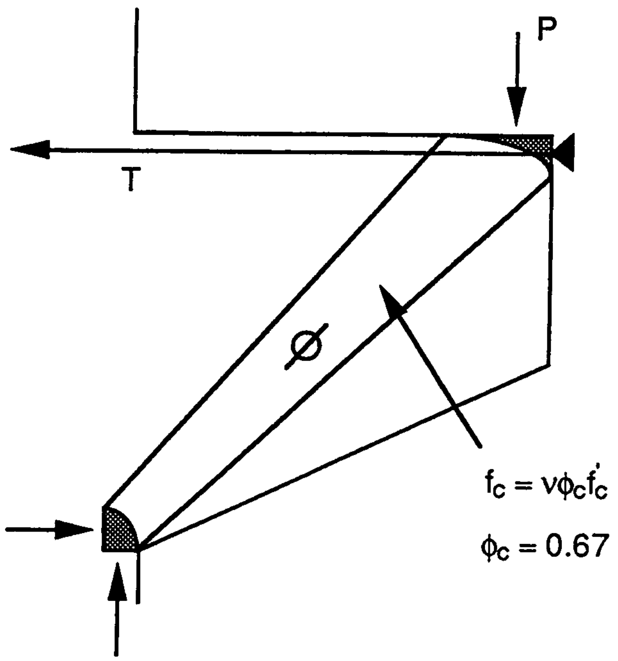

Figure 2.5 Strut and tie model for reinforced concrete corbel

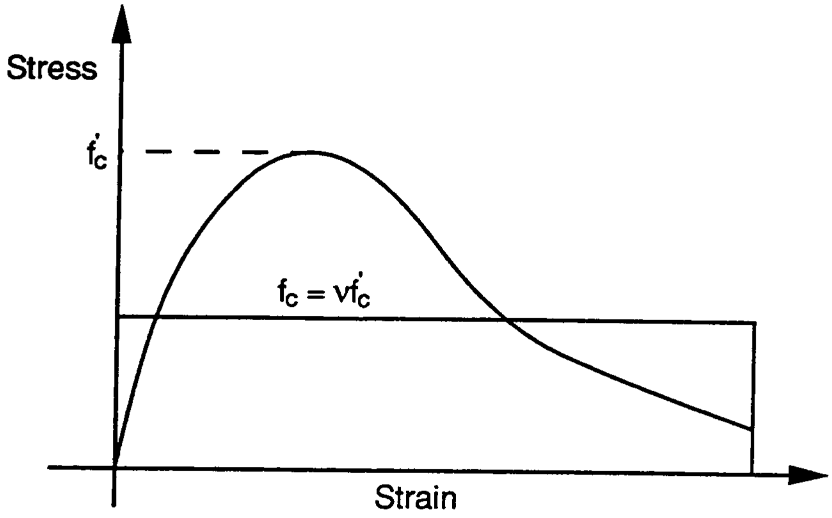

Figure 2.6 Effectiveness factor

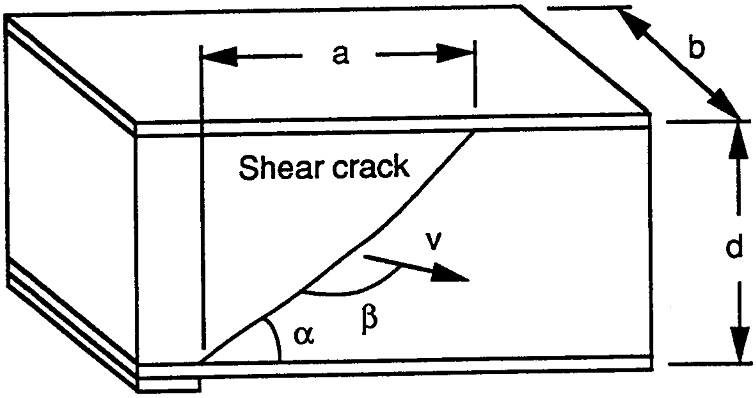

Figure 2.7 Diagonal crack mechanism

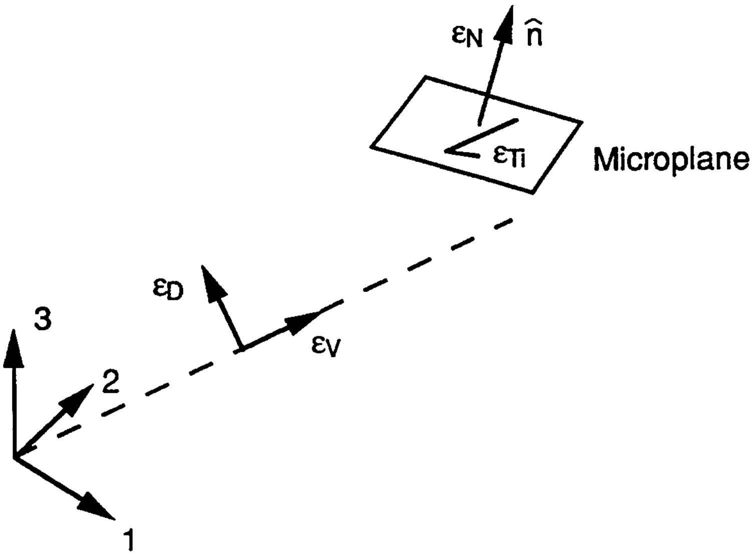

Figure 2.8 Microplane model convention

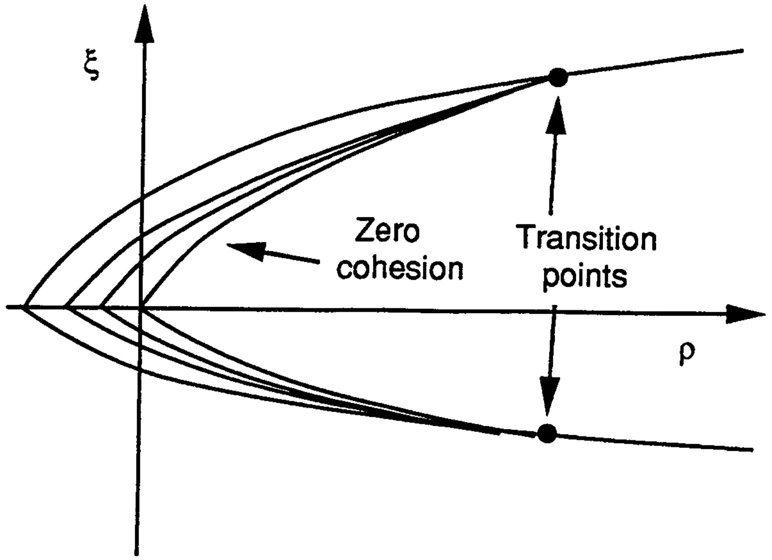

Figure 2.9 Isotropic softening

3.0 MODELLING CONSIDERATIONS

3.1 General

To accurately predict the load-deformation behaviour of composite ice resisting walls, it is important to identify the main characteristics which must be considered in the finite element model. Figure 3.1 shows a typical composite ice wall specimen which was tested by the Center for Frontier Engineering Research, Edmonton (Zimmerman, 1987). The wall consists of a sandwich of two horizontal steel plates which are fastened together by a series of vertical web plates. Concrete infill is then placed in the wall cavities. In some configurations (not considered in this study), steel studs are placed along the top and bottom plates in order to enhance the composite behaviour of the wall system (O' Flynn, 1987).

On offshore drilling platforms, the walls are subjected to highly concentrated loads imposed by ice sheets. The ice pressure magnitudes are in the order of 15 MPa for small areas (less than 1 m^2), diminishing to 3 MPa for larger areas (5-10 m^2). Typically, the cells are 1.0 m deep, and the span between the bulkheads is 4.0 to 6.0 m long. At low load levels, and for this aspect ratio, shear deformation would dominate the behaviour of the concrete cells adjacent to the supports. The principal tensile stresses are diagonally oriented in the cells adjacent to the supports, and are more or less longitudinally oriented in the midspan cells.

As the load increases within the service load range, the concrete loses adhesion with the steel, and slip occurs in the steel cells at certain interfaces. Cracking then takes place, allowing the composite wall system to carry the load into the support bulkheads utilizing truss action as shown in Figure 3.2. The concrete infill in the cells acts as compressive struts, while the web and bottom plates act as tension ties. This stage is represented by line O-A in Figure 3.3, which shows a typical load vs. midspan deflection plot.

As the load/deformation level is further increased, two different modes of behaviour can be identified. If the bottom steel plate yields before the concrete crushes, a load plateau results, which is denoted by Line A-B in Figure 3.3. If the concrete crushing strength is reached in the strut areas before the bottom steel plate yields, the load level will decrease to some residual level, which is shown by Line A-C in Figure 3.3. This load level is typically in the order of 50% of the peak load, and represents the ability of the structure to assume a different load path configuration. Concrete crushing can also occur after the steel plate yields, which results in plate yielding and loading decrease (line B-D in Figure 3.3)

Aside from wall proportions and geometry, the structural factors which control the load-deformation response of composite ice resisting walls are as follows:

a) **Concrete constitutive behaviour** - the uniaxial tensile and compressive strengths determine the wall cracking and crushing loads. If the wall is restrained from out of plane strain, the concrete is confined, and the strut strength is increased. The post-peak response of the concrete is important in determining the level of residual load reached once the compressive struts crush.

b) **Steel-concrete interface behaviour** - the amount of slip that occurs between the steel and concrete determines the stiffness of the structure. If there is no slip, the wall will behave in the manner of a reinforced concrete beam in flexure. If significant slip is introduced, strain compatibility between the steel and concrete is lost, and significant load redistribution occurs. In addition, it has been observed experimentally that the steel plates separate from the concrete in certain places (Zimmerman, 1987). These boundary effects must be included in the finite element analysis in order to obtain an accurate model.

c) **Steel constitutive behaviour** - steel yielding increases ductility of the composite wall system. If yielding is suppressed, the concrete crushes first, and the full flexural plastic capacity of the wall cannot be reached. Therefore, the existence/absence of steel yielding must be detected to allow for an accurate prediction of failure load and system ductility.

This chapter is outlined as follows. Firstly, the concrete constitutive model used here is described. The model adopted is incremental orthotropic, utilizing a secant modulus approach. Next, the method used to simulate the behaviour of the steel concrete interface is described. The model assumes Coulomb friction, and utilizes constraint equations to enforce stick, slip, and separation states (Katona, 1984). A brief description of the steel constitutive model is then given. Finally, the displacement control method used to capture post-peak load deformation behavior is explained.

3.2 Concrete Constitutive Model

3.2.1 General

It is proposed to use a constitutive model of the hypoelastic form to model the stress-strain behaviour of concrete subjected to two dimensional (axisymmetric, plane stress, and plane strain) geometry configurations. The model is limited to the small strain - small displacement formulation, and no creep, thermal or rate effects are considered. Stated simply, hypoelastic materials are those whose rate of stress is a function of the rate of deformation and stress history (Truesdell, 1955).

The constitutive equation for hypoelastic materials can be written in the form

$$d\sigma_{ij} = C_{ijkl} d\varepsilon_{kl}, \qquad [3.1]$$

where the constitutive tensor, C_{ijkl}, is a function of the stress history. In this study, the orthotropic form of hypoelasticity is chosen because of its flexibility and simplicity in modelling salient features of concrete behaviour, such as inclusion of multiaxial stress states, and rotation of average principal cracking and crushing axes. The concept of equivalent uniaxial strain is used as a damage measure in order to decouple the triaxial stress-strain behaviour into a series of uniaxial responses.

The model adopted and implemented here is based, in part, on that used by Elwi and Murray (1979) in analysing the nonlinear response of nuclear containment structures. The form of the orthotropic constitutive equations is described first. Next, the equivalent uniaxial responses of concrete are outlined as functions of stress ratios, failure modes, and mesh refinement. The effect of cracking/crushing on the elastic moduli, Poisson's ratio, and the shear stiffness are then examined. Finally, implementation of the constitutive model is described.

3.2.2 The Constitutive Equations

An orthotropic material contains nine independent variables in the constitutive matrix. If the constitutive relationship is referred to the principal axes of orthotropy, there is no interaction between shear stresses /strains, and normal strains/stresses. Since the material model is intended for use in two dimensional problems, the constitutive matrix reduces to 4X4 in size.

Using the form of an incremental Hooke's law and inverting, the constitutive matrix can be written in the form (Elwi and Murray, 1980)

$$\begin{Bmatrix} d\sigma_1 \\ d\sigma_2 \\ d\sigma_3 \\ d\tau_{12} \end{Bmatrix} = \begin{bmatrix} E_1(1-\eta_{23}^2) & \sqrt{E_1E_2}(\eta_{31}\eta_{23}+\eta_{12}) & \sqrt{E_1E_3}(\eta_{12}\eta_{23}+\eta_{31}) & 0 \\ & E_2(1-\eta_{31}^2) & \sqrt{E_2E_3}(\eta_{12}\eta_{31}+\eta_{23}) & 0 \\ & \text{Sym.} & E_3(1-\eta_{12}^2) & 0 \\ & & & G_{12}\phi \end{bmatrix} \begin{Bmatrix} d\varepsilon_1 \\ d\varepsilon_2 \\ d\varepsilon_3 \\ d\gamma_{12} \end{Bmatrix}, \quad [3.2]$$

where η_{12}, η_{23}, and η_{31} are equivalent Poisson's ratios based on an estimate of Poisson's ratios in the principal planes of orthotropy, ν_1, ν_2, and ν_3:

$$\eta_{12}^2 = \nu_1\nu_2, \qquad [3.3a]$$

$$\eta_{23}^2 = \nu_2\nu_3, \qquad [3.3b]$$

$$\eta_{31}^2 = \nu_3\nu_1, \qquad [3.3c]$$

$$\phi = 1 - \eta_{12}^2 - \eta_{23}^2 - \eta_{31}^2 - 2\eta_{31}\eta_{31}\eta_{31}. \qquad [3.3d]$$

Equations 3.2 can be written in the form

$$\begin{Bmatrix} d\sigma_1 \\ d\sigma_2 \\ d\sigma_3 \\ d\tau_{12} \end{Bmatrix} = \begin{bmatrix} E_1B_{11} & E_1B_{12} & E_1B_{13} & 0 \\ E_2B_{21} & E_2B_{22} & E_2B_{23} & 0 \\ E_3B_{13} & E_3B_{23} & E_3B_{33} & 0 \\ 0 & 0 & 0 & G_{12} \end{bmatrix} \begin{Bmatrix} d\varepsilon_1 \\ d\varepsilon_2 \\ d\varepsilon_3 \\ d\gamma_{12} \end{Bmatrix}, \qquad [3.4]$$

or

$$d\sigma_i = E_i(B_{i1}d\varepsilon_1 + B_{i2}d\varepsilon_2 + B_{i3}d\varepsilon_3), \qquad [3.5a]$$

(no sum)

$$d\tau_{12} = G_{12}d\gamma_{12}. \qquad [3.5b]$$

Note that no summation is implied in Equations 3.5a and b. It is now possible to express the stress increment components in terms of damage measures referred to as equivalent uniaxial strain increments, $d\varepsilon_{iu}$. Rewriting Equation 3.5 in terms of $d\varepsilon_{iu}$ yields

$$d\sigma_i = E_i d\varepsilon_{iu}, \qquad [3.6a]$$

(no sum)

$$d\tau_{12} = G_{12}d\gamma_{12u}, \qquad [3.6b]$$

where

$$d\varepsilon_{iu} = E_i(B_{i1}d\varepsilon_1 + B_{i2}d\varepsilon_2 + B_{i3}d\varepsilon_3), \qquad [3.7a]$$

(no sum)

$$d\gamma_{12u} = d\gamma_{12}. \qquad [3.7b]$$

Again, no summation is implied for Equations 3.6a and b, and Equations 3.7a and b. Total equivalent uniaxial strains can be found by rearranging equation 3.6 and integrating over the loading path

$$\varepsilon_{iu} = \int_{\text{load path}} d\sigma_i/E_i \qquad \text{(no sum)}. \qquad [3.8]$$

Equation 3.8 defines a damage measure at the orientation of the axes of orthotropy. This makes it possible to decouple the axes, and treat the constitutive behaviour of each direction as an equivalent uniaxial response. This uniaxial behaviour in any given direction is primarily a function of confinement (stress ratios) and type of failure mode, which is discussed in more detail in subsequent sections.

It remains to define the axes of orthotropy in the material. Previous definitions have included fixed crack models, where the axes of orthotropy remain fixed in the direction of the first crack formation, and rotating crack models, where the orthotropic axes follow the direction of principal stresses or strains. Fixed crack models are applicable when the principal axes of stress/strain do not rotate appreciably, such as the case where flexural behaviour dominates (Balakrishnan, et al., 1988). This study is primarily directed to structures which undergo significant rotation of the principal axes of stresses and strains. A rotating crack/crush model is, therefore, adopted here. The axes of orthotropy are assumed to follow the principal strain axes, and co-axiality of stresses and strains is maintained. This assumption has implications on the integral of Eq. 3.8, and will be discussed in the implementation section (Section 3.2.8).

An incremental constitutive relationship is next defined for the principal axes of orthotropy. It is now necessary to describe the basic uniaxial curves adopted for compression and tension, and to identify and evaluate the factors which change these curves.

3.2.3 Basic Uniaxial Stress-Strain Curves

Before describing the models adopted for uniaxial compression and tension, it is necessary to define the parameters which describe the shape of the stress-strain curve. Figure 3.4 shows a typical uniaxial stress-strain curve for concrete in compression and tension. The quantities which are required for a complete description of the stress-strain curve are the uniaxial compressive strength, σ_c, the strain at which the compressive strength is reached, ε_c, and the descending branch decay parameters in tension and compression, k_t and k_c respectively.

The Saenz (1964) curve has been widely adopted as an adequate description for a uniaxial stress strain curve. This curve is used here for the pre-peak regions in both tension and compression,and is written as follows

$$\sigma = E_o\varepsilon_u/(1 + (R_e - 2)(\varepsilon_u/\varepsilon_c) + (\varepsilon_u/\varepsilon_c)^2), \qquad [3.9]$$

in which

$$R_e = E_o/E_s, \qquad [3.10]$$

where the quantities E_o and E_s are, respectively, the initial slope of the curve, and the secant slope measured at the peak of the curve.

The descending branches in tension and compression are described by exponential decay parameters, k_t and k_c respectively. The stress-strain relationships for tension and compression are written as

$$\sigma = \sigma_t e^{-k_t(\varepsilon_u - \varepsilon_c)}, \qquad [3.11a]$$

$$\sigma = \sigma_c e^{-k_c(\varepsilon_u - \varepsilon_c)}, \qquad [3.11b]$$

where σ_t and σ_c are tensile and compressive strengths respectively.

Equations 3.11 assures that the stress level reduces to zero at infinite strain.

The equivalent uniaxial description of concrete in compression and tension is now complete. It remains to apply this uniaxial curve in a triaxial stress field, taking into consideration the effects of stress ratios and failure modes. As stress levels are increased, degradation in elastic constants occurs which affects deformation levels in the structure. In addition, once the stress state reaches the descending portion of the curve, stress results are non-objective with respect to mesh refinement. These factors must be dealt with for a complete description of the concrete material model.

3.2.4 Concrete Ultimate Surface

In order to evaluate stress levels and elastic moduli, the effects of changing stress ratios on the ultimate uniaxial parameters mentioned in the previous section must be considered. This is done by using a triaxial ultimate strength surface for both principal stresses and equivalent uniaxial strains. The triaxial strength surface of Willam and Warnke (1975) is herein adopted as an accurate description of concrete behaviour under triaxial stresses. The triaxial strength surface evaluates the average nondimensional shear stress, $\bar{\tau}_a$, as a function of the average nondimensional normal stress, $\bar{\sigma}_a$, and the angle of similarity, θ, which are defined as

$$\bar{\sigma}_a = \sigma_{ii}/3f_{cu}, \qquad [3.12a]$$

$$\bar{\tau}_a = \sqrt{s_{ij}s_{ij}/5f_{cu}^2}, \qquad [3.12b]$$

$$\cos\theta = (\sigma_1+\sigma_2-2\sigma_3)/\sqrt{2}\,((\sigma_1-\sigma_2)^2+(\sigma_2-\sigma_3)^2+(\sigma_3-\sigma_1)^2)^{1/2}, \qquad [3.13]$$

in which s_{ij} is the deviatoric stress tensor which is written as

$$s_{ij} = \sigma_{ij} - \sigma_{kk}\delta_{ij}/3. \qquad [3.14]$$

Physically, the strength surface intersects the deviatoric plane in three symmetrical segments, forming a closed and continuous surface. Figure 3.5 shows a deviatoric trace of the strength surface, which is described in the devatoric plane by a radius function, r. The relationship between the average shear stress, $\bar{\tau}_a$, and the radius function, r, may be written as

$$\bar{\tau}_a = r(\theta,\bar{\sigma}_a). \qquad [3.15]$$

The expression for the radius function is written as follows

$$r = \frac{2r_1r_2\cos\theta + r_2(2r_1-r_2)(4r_{12}\cos^2\theta + 5r_1^2 - 4r_1r_2)^{1/2}}{4r_{12}\cos^2\theta + (r_2-2r_1)^2}, \qquad [3.16]$$

where

$$r_{12} = r_2^2 - r_1^2. \qquad [3.17]$$

The variables r_1 and r_2 are the minimum and maximum radii of the deviatoric trace respectively. These radii vary parabolically with the average stress, $\bar{\sigma}_a$, and are expressed as

$$r_1 = a_0 + a_1\bar{\sigma}_a + a_2\bar{\sigma}_a^2, \tag{3.18a}$$

$$r_2 = b_0 + b_1\bar{\sigma}_a + b_2\bar{\sigma}_a^2. \tag{3.18b}$$

Figure 3.6 is a plot of $\bar{\tau}_a$ vs $\bar{\sigma}_a$ on the rendulic plane. It is seen that r_1 and r_2 are the bottom and top curves respectively. The coefficients a_i and b_i are chosen so that the variables r_1 and r_2 pass through a set of control points on the rendulic plane. In the five parameter Willam and Warnke (1975) model, these points are the uniaxial compressive strength, f_{cu}, biaxial compressive strength, f_{cb}, uniaxial tensile strength, f_{tu}, and one arbitrary high compression point on each rendulic trace, f_{h1} and f_{h2}. In addition, the two radii traces must intersect at the same point in average tension ($\bar{\tau}_a = 0$). These points are marked on Figure 3.6.

It is now possible to evaluate the three σ_{ic} values required in Sections 3.2.1 and 3.2.2. It now remains to evaluate three equivalent uniaxial strains associated with σ_{ic}. The procedure adopted by Elwi and Murray (1980) is used here. An equivalent uniaxial strain surface is assumed, which is similar in form to the strength surface. Values on the surface correspond to equivalent uniaxial strains at ultimate strength.

The procedure used to determine the equivalent uniaxial strength is fairly simple in nature. If incremental proportionality of loading is assumed, it is possible to draw a straight line from the origin to any stress/strain point and obtain the required ultimate strengths/strains. This approach allows for the assessment of damage in at least one direction. But, it may not be adequate in all cases, since the mode of failure becomes important in tensile stress states.

3.2.5 Modes of Failure

For some stress states, the assumption of incremental proportionality may not yield the correct uniaxial stresses/strains. An important example is the biaxial case of high uniaxial tension with low compression in the perpendicular direction, which results in low compressive strength predictions. However, the low strength is probably unrealistic, because the tensile damage due to cracking causes relatively little damage in the perpendicular direction. This also applies in the case of both biaxial tension-compression and triaxial tension.

However, compressive crushing causes significant damage in all perpendicular directions. This is because high compressive stresses cause distributed microcracking in the concrete matrix, which would tend to weaken the concrete in all directions. A simple biaxial example of this is the reduction in tensile strength due to high uniaxial compression.

Taking into consideration the above discussion, the following rules are stipulated for mixed modes (Elwi and Murray, 1980)

a) Triaxial compression - the uniaxial stress/strain parameters are determined from the ultimate surfaces described in Section 3.2.4.

b) Compression-tension modes - the tensile stress/strain parameters are determined from the ultimate surfaces. The compressive strength/strain is set equal to the uniaxial strength/strain, f_{cu} or ε_{cu} if the calculated values from the ultimate surfaces are greater than these quantities.

c) Triaxial tension - the tensile stress/strain parameters are set equal to σ_{tu} or ε_{tu} if the calculated values from the ultimate surfaces are less than these quantities.

The equivalent uniaxial parameters for the three orthotropic directions are now completely defined. It is next necessary to examine the change in elastic moduli which occurs with increasing strain levels.

3.2.6 Change in Elastic Moduli

Figure 3.7 shows two typical loading/unloading segments on a uniaxial compressive stress/strain curve. Before the ultimate strength is reached (Path A-B), the concrete unloads along the initial modulus, E. However, once the descending branch portion of the curve is reached (Path B-C), extensive microcracking in the concrete matrix causes degradation in the elastic modulus, and the material unloads along a reduced modulus, E_r. Similar effects occur for concrete in tension.

Early attempts to model this stiffness decrease with increasing strain levels have mainly concentrated on using the tangent moduli of the uniaxial stress-strain curve. However, this approach can cause numerical instabilities, especially when negative moduli are used in the descending branch portion (Elwi and Murray, 1979). Later attempts used zero moduli (Massicotte et al., 1990, and Ramm and Kompfner, 1984). In this study, in order to maintain numerical stability, the concrete is modelled as a fracturing material. And for simplicity, no plastic strain is introduced. This is done by utilizing the secant modulus of the uniaxial stress-strain curve as the strain level increases.

Values of Poisson's ratio are affected significantly by the direction of applied uniaxial strain. If the uniaxial strain is compressive, the subsequent microcracking in the concrete results in significant lateral expansion. The curve fit from Elwi and Murray (1980) of uniaxial data from Kupfer, Hilsdorf, and Rusch (1969) is adopted as an adequate description of Poisson's ratio variation in compression

$$\nu = \nu_0(1 + 1.3763\alpha - 5.36\alpha^2 + 8.5860\alpha^3), \qquad [3.19a]$$

where

$$\alpha = \varepsilon_{iu}/\varepsilon_{ic}. \qquad [3.19b]$$

A thermodynamic limit of 0.5 is placed upon Poisson's ratio in compression, although there is a possibility of dilatation which corresponds to unstable microcrack propagation (Kotsovos and Newman, 1977). This dilatation would result in a decrease in Poisson's ratio after the concrete ultimate strength is reached. Due to the lack of experimental data pertaining to Poisson's ratio in the post-peak range, the incompressible limit of 0.5 is retained here.

In tension, Poisson's ratio remains constant until a definite pattern of microcracks in the mortar forms. This occurs at approxiamtely 50% of the ultimate tensile strength. After this point, Poisson's ratio gradually decreases as the microcracking becomes more extensive until a macrocrack forms across the cracking plane. The crack is then wide enough so that no lateral movement occurs due to the applied stress. The expressions used by Elwi and Murray (1980) are adopted for Poisson's ratio in tension

$$\nu_i = \nu_0 \qquad 0 < \varepsilon_{iu}/\varepsilon_{ic} \leq 0.5, \qquad [3.20a]$$

$$\nu_i = 2\nu_0(1 - \varepsilon_{iu}/\varepsilon_{ic}) \qquad 0.5 < \varepsilon_{iu}/\varepsilon_{ic} \leq 1.0, \qquad [3.20b]$$

$$\nu_i = 0.0 \qquad 1.0 < \varepsilon_{iu}/\varepsilon_{ic}. \qquad [3.20c]$$

Note that Equation 3.20b implies a linear reduction in Poisson's ratio between 50% and 100% of ε_{ic}.

The shear modulus, G_{12}, is reduced as tensile and compressive strains are increased. In tension, this is due to the reduction in shear interface transfer stiffness as the crack widens, whereas in compression the shear modulus reduction is due to the proliferation of microcracks throughout the concrete matrix Many investigators (eg. Balakrishnan et.al, 1987) have proposed stiffness reductions with increasing tensile strain. In this study, a simple linear modulus reduction with increasing tensile and compressive strain is assumed. The strategy used for the shear modulus reduction is to determine the direction of greatest damage, and use that direction as a basis for reducing the modulus. The estimate of damage used here is the reduction in normal moduli, E_i, relative to the initial Young's modulus. The reduction in shear modulus can be written as

$$G_{12} = G_{12o}\left(\frac{E_i}{E_{io}}\right), \qquad [3.21]$$

where the modular ratio, E_i/E_{io}, is taken as the smallest value for the in-plane directions, namely i = 1 and 2.

It was mentioned previously that co-axiality between principal stresses and strains was maintained. Previous studies have concentrated on expressing the shear modulus as a function of the total normal stresses and strains which maintains automatic co-axiality. In this study, it is assumed that the principal stress model accurately describes concrete constitutive behaviour. In other words, the influence of shear stresses on the orthotropic planes is small. For this reason, the total shear stresses are set to zero for each stress increment.

The local constitutive description for the concrete material is now complete. It is next necessary to describe and evaluate the nonlocal (mesh dependent) behaviour which occurs due to strain localization in compression and tension.

3.2.7 Nonlocal Softening Behaviour

In the recent past, the phenomenon of strain softening in concrete under tensile stresses beyond the ultimate tensile strength has been extensively investigated. It is generally agreed that the post peak response of concrete using point (constitutive) models can not be objective with respect to mesh refinement unless the descending branch of the tensile stress strain curve is chosen to account for strain localization in the crack process zone (Bazant and Oh, 1983).

Although extensive work has been carried out on concrete in tension, the problem of strain localization for concrete in compression has yet to be addressed. Many different constitutive models utilize uniaxial compressive stress-strain curves that include softening branches. Using such a constitutive model will result in non-objective behaviour in compression similar to that developed in tensile models. In addition, there is experimental evidence of strain localization in compressive cylinders from the results of tests performed by Chen and Yamaguchi (1985), who found that the slope of the descending branch in compression was strongly influenced by the cylinder length.

It is proposed here to use a unified approach for both tension and compression localization following the approach adopted by Bazant and Oh (1983). The area under the descending branch is related to a fracture crushing energy which is assumed to be a material constant.

Although readily available for uniaxial tension, crushing energies in compression have not yet been defined.

In order to describe the strain softening phenomenon, it is best to use a simple uniaxial model such as that used by De Borst (1985). Figure 3.8a shows a tensile specimen discretized with **m** elements along its length. These elements can be idealized as a series of springs along the length of the specimen, shown in Figure 3.8a. The material stress-strain curve is approximated by two linear segments (see Figure 3.8b). The descending branch of the curve reaches zero stress at a multiple of the strain at which peak stress occurs, $\mathbf{n}\varepsilon_c$. If all springs have identical properties and loading is uniform, the springs deform uniformly, and the output stress-strain curve matches the input stress-strain curve everywhere. However, if one spring is deformed more than the others (representing a fracture process zone) in the descending branch of the stress-strain curve, this spring will follow path A (loading) in Figure 3.8b, while the other springs will follow path B (unloading). The cumulative effect of this structural response gives rise to the incremental stress-strain relationship of the descending branch, which can be expressed as (De Borst, 1985)

$$\Delta\sigma = \frac{1}{\frac{n}{m} - 1} E\Delta\varepsilon. \qquad [3.22]$$

It is readily seen from Equation 3.22 that as the number of elements, m, increases, the decrement in stress, $\Delta\sigma$, increases for constant n and $\Delta\varepsilon$. This results in a higher rate of softening with increasing mesh refinement.

The crack band theory as proposed by Bazant and Oh (1983) removes this localization by utilizing the fracture mechanics model proposed by Hillerborg (1985) in a smeared sense. Figure 3.9 is a plot of stress versus crack displacement for a tensile specimen. It is found from experiment that this curve is invariant with respect to specimen size.

The area under the stress versus crack displacement curve is defined as the fracture energy, G_f, which is the amount of energy consumed by crack formation per unit area of the crack plane. This can be expressed as

$$G_f = \int_0^{w_{max}} \sigma dw, \qquad [3.23]$$

where dw is the crack elongation in the fracture zone, and w_{max} is the crack displacement at zero stress.

The deformation in the crack zone, w, can be viewed as being caused by strains within the fracture zone

$$w = \int_0^{h_c} \varepsilon dl, \qquad [3.24]$$

where h_c is the width of the fracture zone. If the strain is uniformly distributed along the width of the fracture zone, Equation 3.24 can be rearranged to form

$$\frac{G_f}{h_c} = \int_0^{\varepsilon_u} \sigma d\varepsilon. \qquad [3.25]$$

The quantity ε_u is the strain at which the stress level is zero. Stated simply, the area under the descending branch of the input uniaxial stress strain is equal to the fracture energy divided by the fracture zone width. In theory, this fracture width reduces to zero in the limit. However, due to inhomogeneities in the material, this width is several times the aggregate size (Bazant, 1985). In conventional finite element analysis, the width of the fracture zone is restricted to the spacing of the Gauss sampling points.

As mentioned in Section 3.2.3, tensile and compressive uniaxial descending branches are described by exponential decay parameters, k_t and k_c respectively.. It is necessary to determine the required value of the decay parameters for a given mesh refinement and fracture or crushing energy. The method of determining k_t will be discussed first; the expressions that result can then be used to determine k_c.

The area under the input uniaxial descending branch for tension or compression, A_{cd}, is given by the expression

$$A_{cd} = \int_0^{\infty} \sigma d\varepsilon. \qquad [3.26]$$

Note that A_{cd} is used to describe the uniaxial descending branch in both tension and compression. The upper limit of the integral is infinity because the stress is zero at infinite strain. Substituting Equation 3.11a into Equation 3.26 and integrating yields

$$A_{cd} = \frac{\sigma_c}{k_t}. \qquad [3.27]$$

But, for tension

$$A_{cd} = \frac{G_f}{h_c}. \qquad [3.28]$$

Equating Equations 3.27 and 3.28 yields the following expression for k_t

$$k_t = \frac{\sigma_t h_c}{G_f}. \qquad [3.29]$$

Values of fracture energies, G_f, are readily available for concrete in tension.

As discussed earlier, it is proposed to use a unified method to describe the strain localization which occurs in both tension and compression. It is assumed in this study that a crushing energy in compression, G_{cr}, exists, which is independent of specimen size. From Equation 3.29, it is then possible to relate the compressive decay parameter, k_c, to the crushing energy, G_{cr}

$$k_c = \frac{\sigma_c h_c}{G_{cr}}. \qquad [3.30]$$

However, unlike the case of uniaxial tension there are no known values for crushing energies. Link and Elwi (1989) performed a parametric study of uniaxial concrete cylinders, attempting to relate A_{cd} to the area obtained from a concrete cylinder test, A_c. The study included three different mesh refinements, two different concrete strengths, and four different input areas for a total of 24 analyses. From the parametric study, it was possible to relate the crushing energy, G_{cr}, to A_c

$$G_{cr} = 209.2A_c^{1.25}. \qquad [3.31]$$

Details of the study are given in Appendix A. It remains to obtain the descending branch area for concrete cylinders of different strengths.

Figure 3.10 is a plot of effectiveness factors, α, at 1.5% strain versus concrete strengths obtained from Neilson (1984). The effectiveness factor is an attempt to estimate strength reductions due to lack of ductile behaviour in concrete. Figure 3.11 shows that the effectiveness factor is a measure of the stress level of a perfectly plastic stress block with the same area as a concrete cylinder specimen. From this plot, descending branch areas can easily be obtained. The total area underneath the plastic stress block is calculated as

$$A_{ct} = \alpha \sigma_c \varepsilon_u . \qquad [3.32]$$

If the area under the ascending branch, A_{ca}, is subtracted from Equation 3.32, the area under the descending branch, A_c, is left. Assuming the ascending portion of the stress-strain curve to be parabolic, A_c can be written as

$$A_c = \alpha \sigma_c \varepsilon_u - \frac{2}{3} \sigma_c \varepsilon_c . \qquad [3.33]$$

Data for the effectiveness factor, α, is available to a maximum strain of 1.5%. Setting ε_u equal to 0.015, substituting Equation 3.33 into 3.31, and 3.31 into 3.30, the following expression for k_c is obtained

$$k_c = \frac{h_c}{209.2 \sigma_c^{0.25} (0.015\alpha - 0.667\varepsilon_c)} . \qquad [3.34]$$

Equations 3.30 and 3.34 complete the description of the concrete constitutive model.

3.2.8 Implementation of Constitutive Model

Figure 3.12 is a flowchart of the proposed constitutive model. Given global stresses $\{\sigma\}_g^i$, global strains $\{\varepsilon\}_g^i$, and local orthotropic moduli $\{E\}^i$ at the start of an iteration, it is desired to obtain updated quantities $\{\sigma\}_g^{i+1}$, $\{\varepsilon\}_g^{i+1}$, and $\{E\}^{i+1}$ at the end of the iteration.

In step 1, the global strains are updated; in step 2, the principal strain components and transformation angle, β, are determined. Since the principal strains are used as reference for the orthotropic axes, the global stresses, $\{\sigma\}_g^i$, the global strain increment, $\{\Delta\varepsilon\}_g^i$, and the global constitutive matrix, $[C]_g^i$, are transformed to these local axes. A trial local stress tensor, $\{\sigma\}_{lt}^{i+1}$ is then calculated in step 3.

Equivalent uniaxial strains, $\{\varepsilon\}_{lu}^{i+1}$, are obtained in step 4 by dividing the trial stresses by the orthotropic secant moduli, $\{E\}^i$. This method of calculating equivalent uniaxial strains is in contrast to previous calculation methods, in which the stress increment was divided by the tangent modulus to obtain the equivalent uniaxial strain increment. This strain increment was accumulated over the loading path to obtain the total equivalent uniaxial strain measures (Darwin and Pecknold, 1974). However, as mentioned earlier, the use of tangent moduli in the softening region can cause numerical instabilities in the solution. The calculation procedure adopted here is consistent with the use of secant methods, which have proven stability.

Using Equations 3.12-3.18, it is then possible to evaluate the uniaxial curve parameters, $\{\sigma\}_c$ and $\{\varepsilon\}_c$ in step 5. In step 6, the stress tensor and elastic properties are updated in each of the orthotropic directions. Figure 3.13 shows an example of the updating process for uniaxial compression. The trial stress level, σ_{1t}^{i+1}, is checked against the stress level computed by using Equations 3.9-3.11. If the material is loading (increasing compressive strain), the stress level is updated to σ_1^{i+1}, which falls on the calculated stress-strain curve. This is denoted by path A in Figure 3.13. The orthotropic elastic modulus, E^i, is also updated as a secant modulus to E^{i+1}. If the material unloads, the orthotropic modulus retains its original value, and the stress is decreased along this line, which is denoted by path B. Orthotropic Poisson's ratios and the shear modulus are updated by using Equations 3.19-3.21. The new local constitutive matrix, $[C]_l^{i+1}$, is formed by the new elastic properties in step 7. Finally, the stresses, strains, and constitutive matrix are transformed back to the global axes in Step 8.

3.3 Interface Element Description

3.3.1 General

As previously mentioned in Section 3.1, a proper finite element model of composite ice resisting walls must include the effects of frictional slippage and separation along the steel-concrete interface. Many attempts have been made in the past to obtain a contact algorithm which converges quickly and provides accurate results. Two main methods have been researched; these are the penalty function method, and the Lagrangian multiplier method.

The penalty function method attempts to enforce conditions of contact by the use of stiff springs (Herrman, 1977) or thin layer elements placed between the contact surfaces (Desai, 1982). The method has the advantage of easy finite element implementation; in addition, no extra degrees of freedom are introduced in the stiffness equations as for the Lagrangian multiplier method. However, overly stiff springs or thin layers may cause ill conditioning in the stiffness equations, resulting in a substantial loss of accuracy.

The Lagrangian multiplier method enforces conditions of contact by using Lagrangian multipliers as extra degrees of freedom in the stiffness equations. These multipliers represent the constraint forces which are necessary to maintain contact. The augmented set of equations has no conditioning problems, hence, accuracy is increased over that of the penalty function method. However, the extra degrees of freedom increase the size of the stiffness matrix, resulting in increased solution times. It was decided that accuracy was of paramount importance, and that the extra solution time required by the Lagrangian multiplier method was negligible, hence the Lagrangian multiplier method was chosen.

Several variations of this method are available, including node to surface contact (Bathe and Chaudhary, 1985), and node to node contact (Katona, 1984). The former method is more suitable for large deformation contact problems, and since the composite ice wall problem can be adequately described with small displacement theory, the node to node contact algorithm derived by Katona (1984) was adopted. A brief description of this method follows.

3.3.2 Constraint Equations

The contact algorithm utilizes the classical Lagrangian multiplier equations derived from virtual work principles. The augmented stiffness equations can be written in the form (Katona, 1984)

$$\begin{bmatrix} K & C^T \\ C & 0 \end{bmatrix} \begin{Bmatrix} \Delta q \\ \Delta \lambda \end{Bmatrix} = \begin{Bmatrix} \Delta Q \\ \Delta a \end{Bmatrix}, \qquad [3.35]$$

where $[K]$ is the usual finite element stiffness matrix, and $[C]$ is a matrix which enforces constraint conditions between displacements. The constraint condition can be written as

$$[C]\{\Delta q\} = \{\Delta a\}. \qquad [3.36]$$

For the contact problem, the quantities $\{\Delta a\}$ and $\{\Delta\lambda\}$ represent incremental nodal separations and contact forces, respectively. Since the node to node contact method does not introduce any stiffness terms in $[K]$, the constraint equations can be separated from the augmented stiffness matrix and assembled in the global stiffness matrix as separate interface elements. The "stiffness" matrix of the interface elements can be written as

$$[K]_{int} = \begin{bmatrix} 0 & C^T \\ C & 0 \end{bmatrix}. \qquad [3.37]$$

These elements, hereinafter referred to as the "gap elements", also have analogous "load" vectors which can be expressed as

$$\{\Delta Q\}_{int} = \begin{Bmatrix} 0 \\ \Delta a \end{Bmatrix}. \qquad [3.38]$$

"Stiffness" matrices and "load" vectors can be written for three basic states of interface behaviour; fixed, slip, and free.

3.3.3 Interface States

Before describing the interface states of behaviour in terms of finite element matrices, it is necessary to define the convention used to describe the interface geometry. Figure 3.14 shows the nodes which are assumed to be contact pairs. The normal to the interface is inclined at an angle ϕ with the global axis, and the nodes are separated in the local coordinate directions by distances Δ_N and Δ_T, respectively.

For the fixed state, two constraint equations are required to describe the relative movement between nodes. These are expressed in terms of global axes as

$$\begin{bmatrix} -\cos\phi & -\sin\phi & \cos\phi & \sin\phi \\ \sin\phi & -\cos\phi & -\sin\phi & \cos\phi \end{bmatrix} \begin{Bmatrix} \Delta u_1 \\ \Delta v_1 \\ \Delta u_2 \\ \Delta v_2 \end{Bmatrix} = \begin{Bmatrix} \Delta a \\ \Delta b \end{Bmatrix}, \qquad [3.39]$$

where Δa and Δb are, respectively, the relative normal and tangential movements to be imposed on nodes 1 and 2. If the nodes are coincident, the quantities Δa and Δb are zero. However, if overlap exists, these movements can be nonzero.

The slip state requires one constraint equation restraining relative normal movement and the specification of the incremental tangential constraint force

$$\left\langle -\cos\phi \quad -\sin\phi \quad \cos\phi \quad \sin\phi \right\rangle \begin{Bmatrix} \Delta u_1 \\ \Delta v_1 \\ \Delta u_2 \\ \Delta v_2 \end{Bmatrix} = \Delta a, \qquad [3.40a]$$

$$\Delta\lambda_T = T. \qquad [3.40b]$$

In this case, the quantity T represents the tangential force in excess of the allowable sliding force. Assuming Coulomb friction, T is written as

$$T = \lambda_T - \mu\lambda_N, \qquad [3.41]$$

where μ is the friction coefficient, and λ_N and λ_T are the accumulated normal and tangential forces respectively at the nodes.

The free state requires the specification of both incremental constraint forces as follows

$$\Delta\lambda_N = N, \qquad [3.42a]$$

$$\Delta\lambda_T = T, \qquad [3.42b]$$

where N and T are the negative total accumulated interface forces, and are given by

$$N = -\lambda_N, \qquad [3.43a]$$

$$T = -\lambda_T. \qquad [3.43b]$$

The "stiffness" and "load" matrices used for each state are shown in Table 3.1. The values N and T are the specified normal and tangential forces to be used in calculating the "load" vector. Criteria for changing states within an iterate, such as fixed to free, are next described.

3.3.4 Criteria for Changing Interface States

As the interface forces and displacements are updated, it becomes necessary to update the interface state for changes in loading. For example, if a fixed interface node pair is placed under tensile loading, the nodes separate, and the state is then free.

Table 3.2 is a decision matrix which gives criteria for changing states within an iteration. In order to change from fixed to slip, the frictional force $\mu\lambda_N$ must be overcome. The change in fixed or slip to free occurs when tensile contact loads are encountered. Note that there is no slip to fix state change. Once an interface pair slips, it is assumed to maintain the slip state until the end of the load step. If additional load steps are imposed, all slipped points are reset to fixed. In order to change from free to fixed, the nodes must penetrate each other. Table 3.3 shows the specified values required in the "load" vector to maintain the given state changes.

The description of the interface element is now complete. It remains to describe the implementation procedure.

3.3.5 Implementation Procedure

Figure 3.15 is a schematic of the procedure used in the finite element implementation of the interface model.

Given the following values at the start of a load increment; the contact forces λ_N^i and λ_T^i, the accumulated nodal separations, Δ_N^i and Δ_T^i, the interface "stiffness" matrix $[K]_{int}^i$, and the interface "load" vector $\{\Delta Q\}_{int}^i$, it is desired to obtain updated quantities λ_N^{i+1}, λ_T^{i+1}, Δ_N^{i+1}, Δ_T^{i+1}, $[K]_{int}^{i+1}$, and $\{\Delta Q\}_{int}^{i+1}$ at the end of the load increment.

In step 1, the contact forces and nodal separations are updated. The interface state is then checked in Step 2 by using Table 3.2 to see if a change in state is necessary. Table 3.1 is used to update the interface "stiffness" matrix, and the "load" vector is updated in Step 3 by using Table 3.3. Convergence to the correct states is measured by using the convergence criteria for the global finite element system.

3.4 Steel Constitutive Model

A simple bilinear Von Mises isotropic hardening steel model was adopted to represent the loading-unloading behaviour in the steel plates. The isotropic hardening model assumes that the yield surface expands uniformly with plastic deformation. This was felt to be adequate, since significant loading-unloading phenomena, such as hysteresis loops due to cyclic loading, were not considered in the study. In these cases, kinematic hardening, where the yield surface translates with increasing plastic deformation, would be more appropriate.

The theory and implementation of Von Mises hardening models is well documented in the literature (Owen and Hinton, (1985), Chen (1982), Bathe (1982)) and, therefore, will not be repeated here.

3.5 The Displacement Control Method

As described earlier, the evaluation of structural ductility in ice-resisting walls requires the determination of load-deformation behavior after the peak load has been reached. Traditional methods, such as the Newton-Rhapson algorithm, fail if the applied load decreases with increasing deformation. It is therefore necessary to adopt a solution strategy which can capture this important regime of behavior.

Two methods are commonly used to compute post-peak response in structures; the constant arc length method, and the displacement control method (Ramm, 1980). The displacement control method is adopted here because of its simplicity, and the availability of a stable displacement control point (the midspan of the tested specimens).

The strategy of the displacement control method is best described through the use of a simple example. Figure 3.17 shows the case of a beam which deflects from its initial configuration at A to a new configuration at B under a load increment, ΔP. The displacement increment between A and B at midspan is denoted by Δq_{AB}. It is desired to apply a specified displacement increment at this location, and evaluate the change in load, ΔP, that is consistent with this displacement increment.

To achieve this, it is necessary to decompose the displacement increment, $\{\Delta q\}$, into two parts; one part based on the unbalanced loads, $\{\Delta q\}^{(i)II}$, and one based on a reference load vector, $\{\Delta q\}^{(i)I}$, which is parallel to the applied load vector

$$\{\Delta q\} = \Delta\lambda^{i}\{\Delta q\}^{(i)I} + \{\Delta q\}^{(i)II}. \qquad [3.44]$$

The superscripts "i" represent the iteration number, since the strategy is iterative. The quantity $\Delta\lambda^{(i)}$ is a scaling factor, which represents the amount that the reference load vector displacement must be scaled to obtain the correct control displacement, Δq_{AB}. The quantities $\{\Delta q\}^{(i)I}$ and $\{\Delta q\}^{(i)II}$ are obtained from (Ramm, 1980)

$$[K]^{(i)}\{\Delta q\}^{(i)II} = \{\Delta Q\}^{(i)}, \qquad [3.45]$$

$$[K]^{(i)}\{\Delta q\}^{(i)I} = \{R*\}^{(i)}. \qquad [3.46]$$

The load vectors $\{\Delta Q\}$ and $\{R*\}$ are unbalanced load and reference load vectors respectively. Figure 3.16 graphically illustrates the two displacement components in Equation 3.44 in global displacement space.

It now remains to compute a scaling factor, $\Delta\lambda^{(i)}$, which gives the correct control displacement, Δq_{AB}. Equation 3.44 must hold for the control displacement as well as the global displacement, ie.

$$\Delta q_{AB} = \Delta\lambda^{(i)} \Delta q_{AB}^{(i)I} + \Delta q_{AB}^{(i)II}. \qquad [3.47]$$

An expression for $\Delta\lambda^{(i)}$ is obtained by rearranging Equation 3.47

$$\Delta\lambda^{(i)} = \frac{\Delta q_{AB} - \Delta q_{AB}^{(i)II}}{\Delta q_{AB}^{(i)I}}. \qquad [3.48]$$

Figure 3.17 graphically illustrates the procedure. On the first iteration (from point A to point 1 in Figure 3.17), the unbalanced loads are theoretically zero. Equation 3.48 then reduces to

$$\Delta\lambda^{(1)} = \frac{\Delta q_{AB}}{\Delta q_{AB}^{(1)I}}. \qquad [3.49]$$

For all subsequent iterations, the control displacement has already been applied. This means that Δq_{AB} is zero, and Equation 3.48 then becomes

$$\Delta\lambda^{(i)} = - \frac{\Delta q_{AB}^{(i)II}}{\Delta q_{AB}^{(i)I}}. \qquad [3.50]$$

Figure 3.18 is a flowchart of the procedure used in implementing the displacement control method. Given the reference load vector, $\{R^*\}$, and the specified control displacement, Δq_{AB}, it is desired to obtain the updated load and displacement levels, {P} and {q}, which are consistent with the control displacement level.

In steps 1 and 2, the scaling factor for the first iterate, $\Delta\lambda^{(1)}$, is obtained from Equation 3.49. The load and displacement vectors, {P} and {q}, are updated in step 3. These three steps represent the movement to Point 1 in Figures 3.16 and 3.17. In step 4, the unbalanced load vector, $\{\Delta Q\}^{(i)}$, and stiffness matrix, $[K]^{(i)}$, are updated. These quantities are then used to determine the displacement components $\{\Delta q\}^{(i)I}$ and $\{\Delta q\}^{(i)II}$ in step 5. The correct scaling factor, $\Delta\lambda^{(i)}$, is determined in step 6 by using Equation 3.50. Finally, the load and displacement vectors are updated in steps 8 and 9, and represent the movement from Point 1 to Point 3 in Figures 3.16 and 3.17. Iteration is performed until the desired solution accuracy is obtained.

	"Stiffness"						
State	u_1	v_1	u_2	v_2	λ_N	λ_T	"Load"
Fixed	0	0	0	0	-C	-S	0
	0	0	0	0	-S	-C	0
	0	0	0	0	C	-S	0
	0	0	0	0	S	C	0
	-C	-S	C	S	0	0	Δa
	S	-C	-S	C	0	0	Δb
Slip	0	0	0	0	-C	0	-ST
	0	0	0	0	-S	0	CT
	0	0	0	0	C	0	ST
	0	0	0	0	S	0	-CT
	-C	-S	C	S	0	0	Δa
	0	0	0	0	0	1	T
Free	0	0	0	0	0	0	CN - ST
	0	0	0	0	0	0	SN + CT
	0	0	0	0	0	0	-CN + ST
	0	0	0	0	0	0	-SN - CT
	0	0	0	0	1	0	N
	0	0	0	0	0	1	T

$C = \cos\phi$

$S = \sin\phi$

Table 3.1 "Stiffness" and "load" quantities for interface states

Iteration i + 1 i	Fix	Slip	Free
Fix	$\lambda_N < 0$ $\lambda_T < \mu \lambda_N$	$\lambda_N < 0$ $\lambda_T > \mu \lambda_N$	$\lambda_N > 0$
Slip	——	$\lambda_N < 0$	$\lambda_N > 0$
Free	$\Delta_N < 0$	——	$\Delta_N > 0$

Table 3.2 Decision matrix for interface states

Iteration i + 1 i	Fix	Slip	Free
Fix	$\Delta a = 0$ $\Delta b = 0$	$\Delta a = 0$ $T = \mu \lambda_N - \lambda_T$	$N = -\lambda_N$ $T = -\lambda_T$
Slip	——	$\Delta a = 0$ $T = \mu \lambda_N - \lambda_T$	$N = -\lambda_N$ $T = -\lambda_T$
Free	$\Delta a = -\Delta_N$ $\Delta b = 0$	——	$N = 0$ $T = 0$

Table 3.3 Specified values for "load" vector

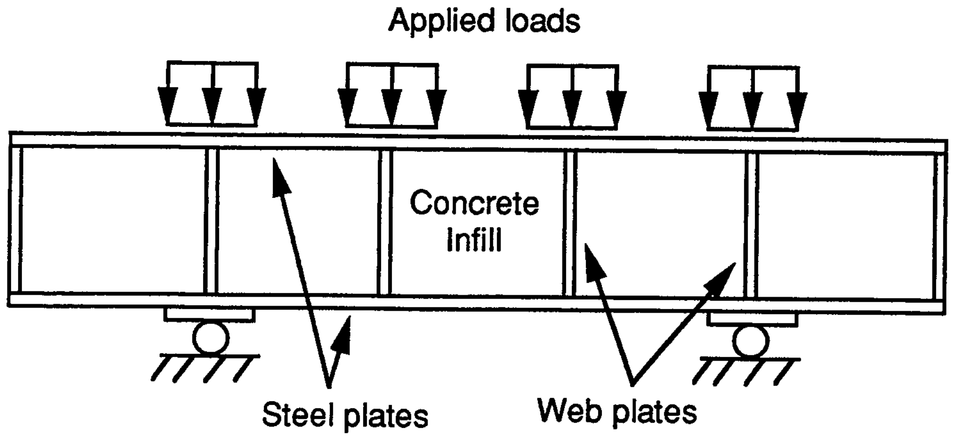

Figure 3.1 Typical C-FER composite ice wall specimen

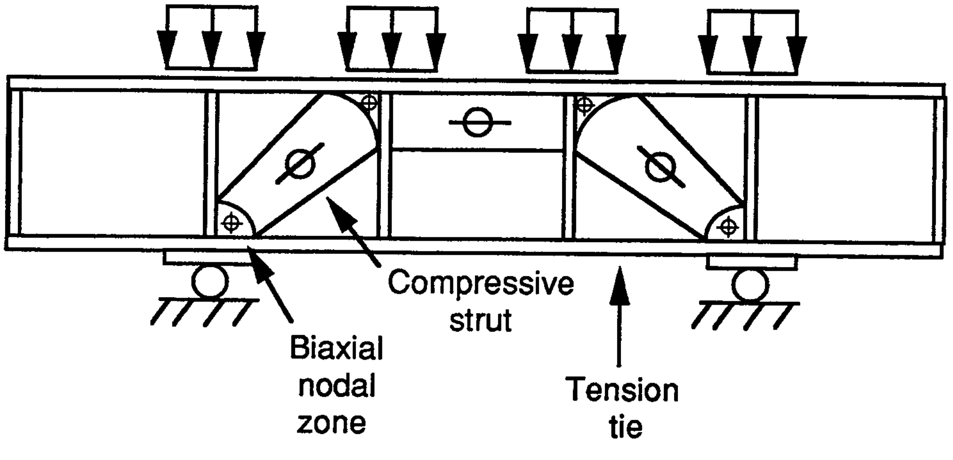

Figure 3.2 Strut and tie action in a composite wall

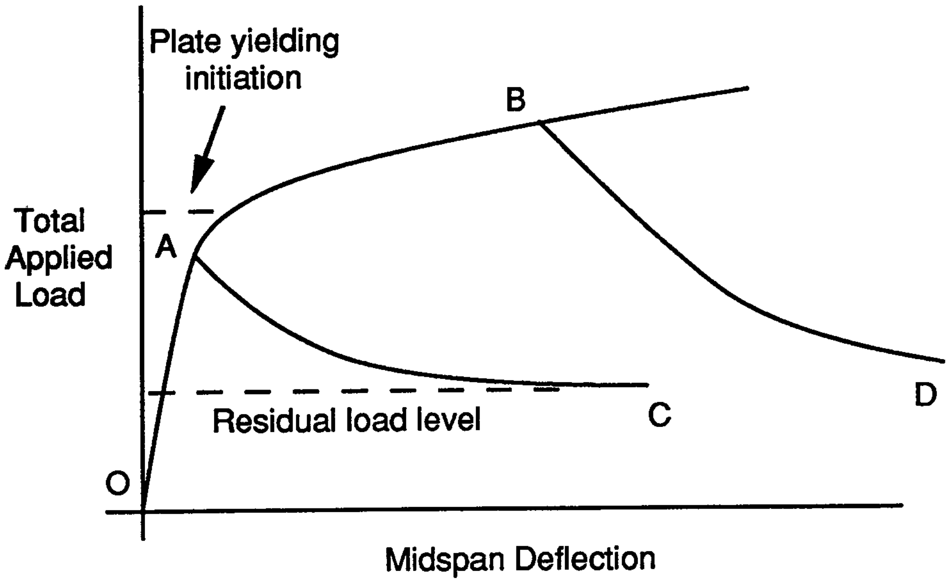

Figure 3.3 Load vs. midspan deflection of composite ice wall

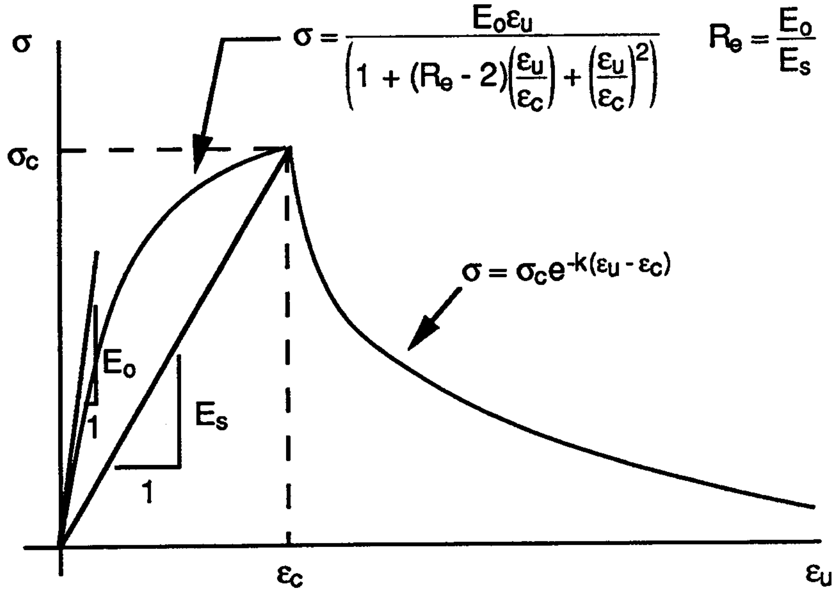

Figure 3.4 Proposed uniaxial stress-strain curve for concrete

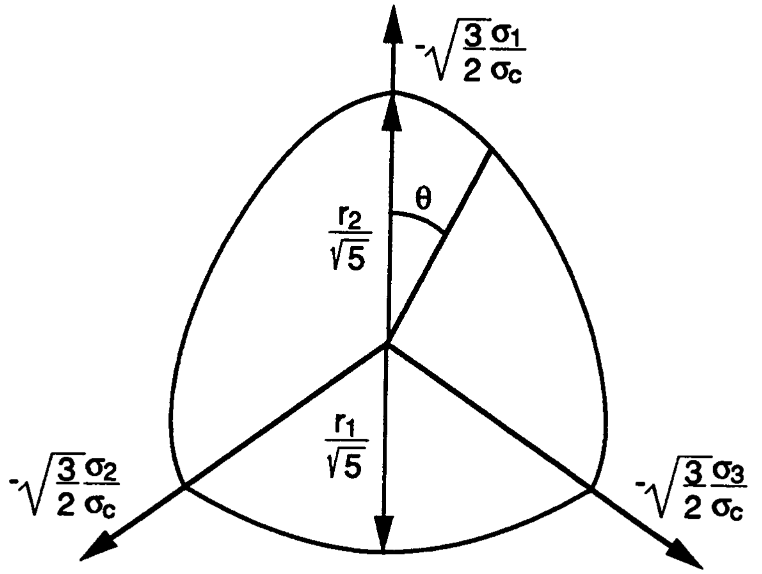

Figure 3.5 Deviatoric trace of Willam-Warnke strength surface

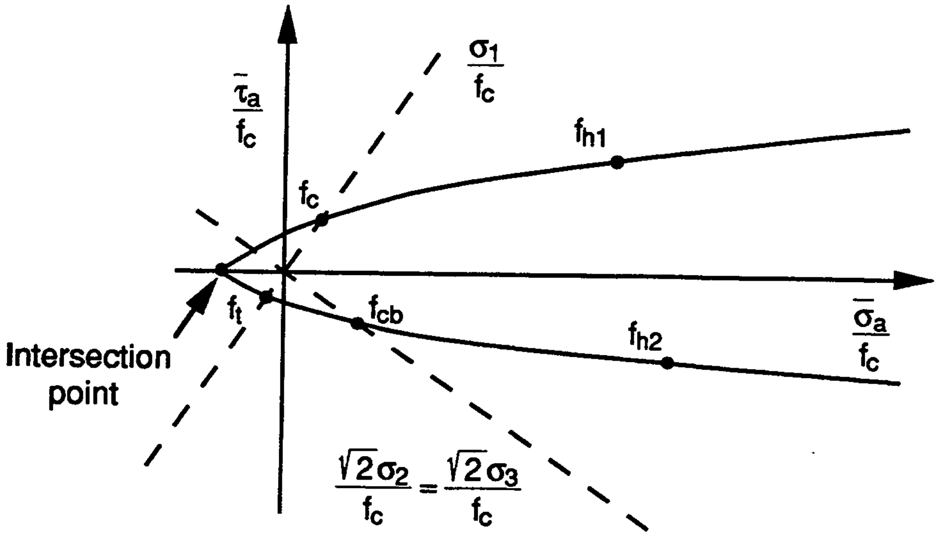

Figure 3.6 Rendulic trace of Willam-Warnke strength surface

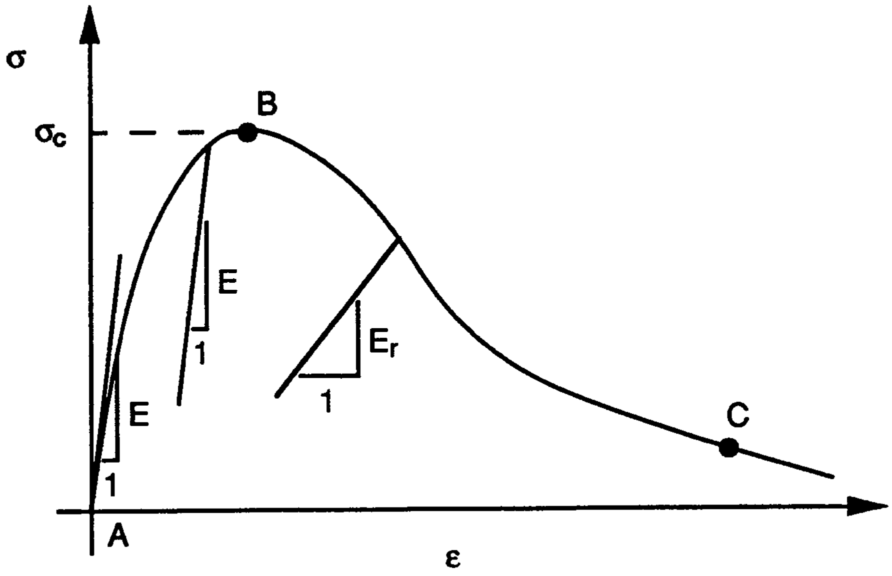

Figure 3.7 Elastic modulus degradation

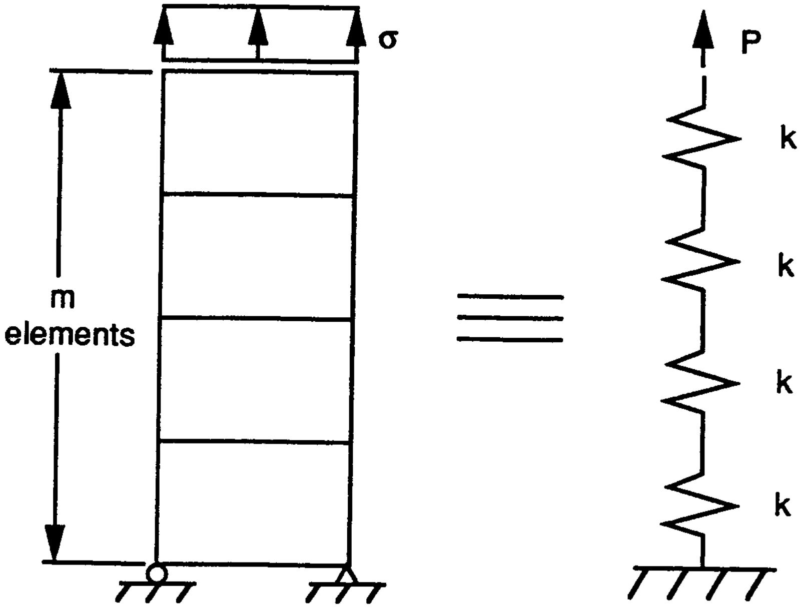

Figure 3.8a Spring analogy for strain localization

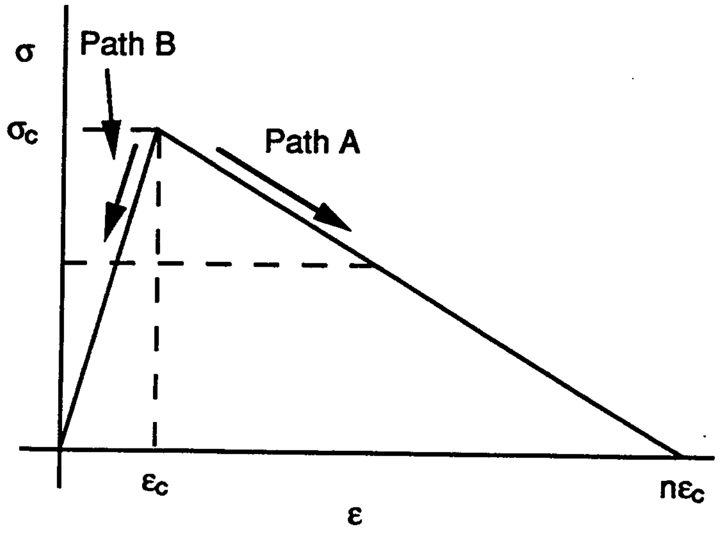

Figure 3.8b Stress-strain paths for strain localization

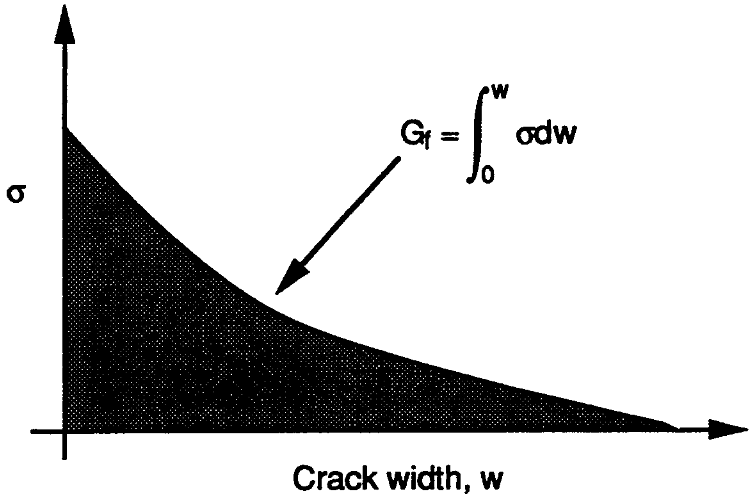

Figure 3.9 Fracture energy definition

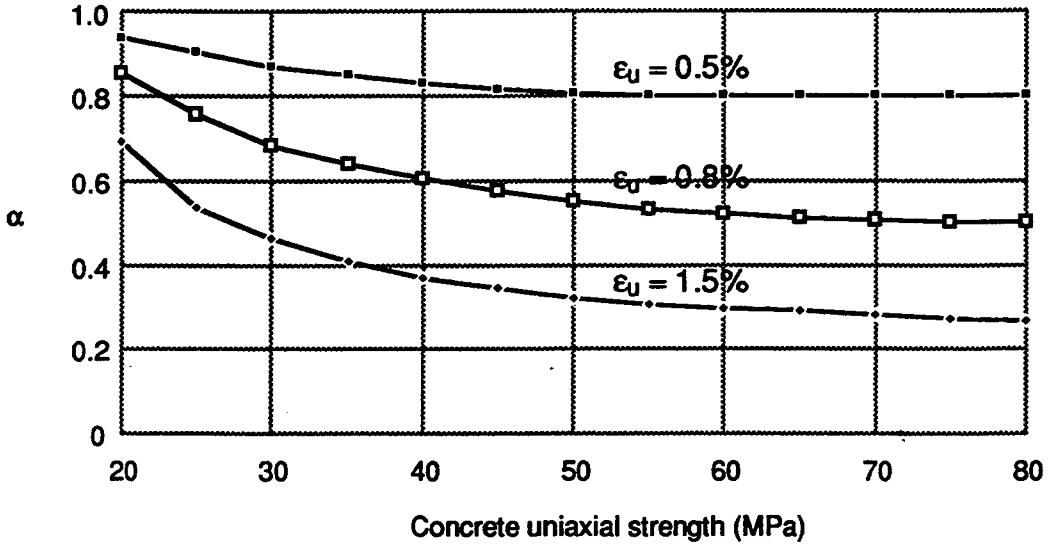

Figure 3.10 Effectiveness factor versus concrete strength

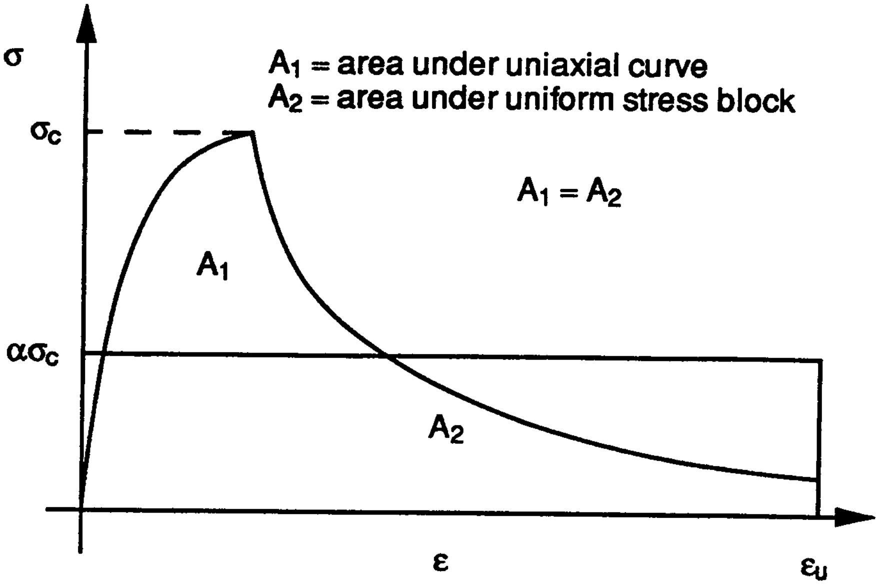

Figure 3.11 Effectiveness factor definition

Given $\{\sigma\}_g^i$, $\{\varepsilon\}_g^i$, $\{\Delta\varepsilon\}_g$, $[C]_g$, $\{E\}^i$, $\{\nu\}^i$, G_{12}^i

1) Update global strains

$$\{\varepsilon\}_g^{i+1} = \{\varepsilon\}_g^i + \{\Delta\varepsilon\}_g$$

2) Refer $\{\varepsilon\}_g^{i+1}$, $\{\sigma\}_g^i$, $[C]_g^i$ to local coordinate system

$$\{\varepsilon\}_g^{i+1} \Rightarrow \{\varepsilon\}_l^{i+1},\ \beta$$

β = transformation angle used in transformation matrix [T]

$$\{\sigma\}_l^i = [T]\{\sigma\}_g^i$$

$$[C]_l^i = [T]^T[C]_g^i[T]$$

3) Obtain a trial local stress tensor

$$\{\Delta\sigma\}_l = [C]_l^i\{\Delta\varepsilon\}_l$$

$$\{\sigma\}_{lt}^{i+1} = \{\sigma\}_l^i + \{\Delta\sigma\}_l$$

4) Calculate equivalent uniaxial strains

$$\{\varepsilon\}_{lu}^{i+1} = \{\sigma\}_{lt}^{i+1}/\{E\}_i$$

$\{E\}_i$ = orthotropic direction moduli

5) Define uniaxial curve parameters σ_c, ε_c

$\{\sigma\}_l^{i+1} \Rightarrow \sigma_c$ **Equations [3.13]-[3.18], Section 3.2.4**

Figure 3.12 Flow chart for constitutive model

$$\{\varepsilon\}_{lu}^{i+1} \Rightarrow \varepsilon_c$$

6) Update stress tensor $\{\sigma\}_l^{i+1}$, direction moduli $\{E\}^{i+1}$, Poisson's ratio $\{\nu\}^{i+1}$, and shear modulus G_{12}^i

$\{\sigma\}_{lt}^{i+1} \Rightarrow \{\sigma\}_l^{i+1}$ **Equations [3.9]-[3.11]**

$\{E\}^i \Rightarrow \{E\}^{i+1}$ **Secant modulus update**

$\{\nu\}^i \Rightarrow \{\nu\}^{i+1}$ **Equations [3.19]-[3.20]**

$G_{12}^i \Rightarrow G_{12}^{i+1}$ **Equation [3.21]**

7) Compute $[C]_l^{i+1}$

$$\{E\}^{i+1},\ \{\nu\}^{i+1},\ G_{12}^{i+1} \Rightarrow [C]_l^{i+1}$$

8) Refer quantities back to global system

$$\{\sigma\}_g^{i+1} = [T]^T\{\sigma\}_l^{i+1}$$

$$[C\}_g^{i+1} = [T][C]_l^{i+1}[T]^T$$

Steps 1-8 obtain

$$\{\sigma\}_g^{i+1},\ \{\varepsilon\}_g^{i+1},\ [C]_g^{i+1},\ \{E\}^{i+1},\ \{\nu\}^{i+1},\ G_{12}^{i+1}$$

Figure 3.12 (cont'd) Flow chart for constitutive model

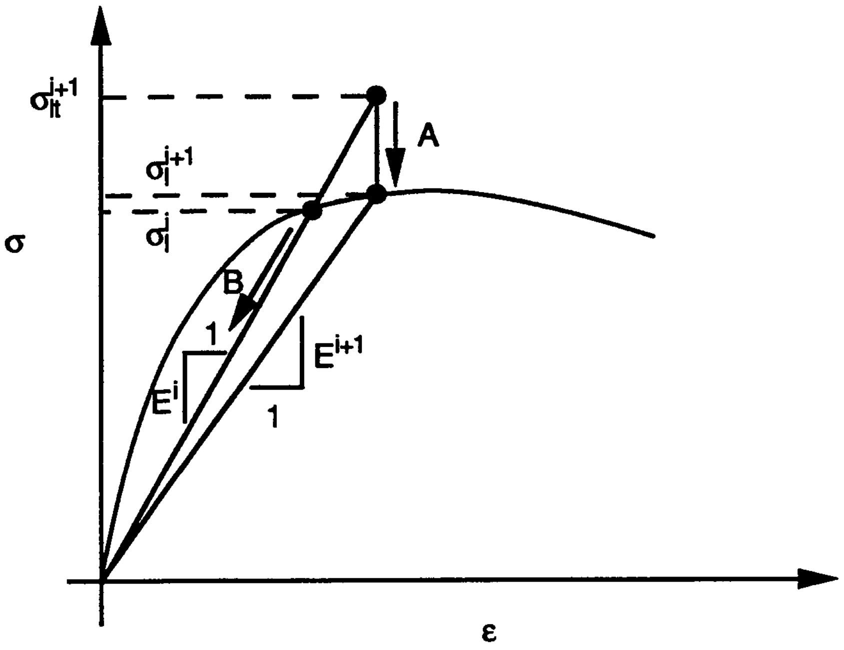

Figure 3.13 Stress updating example

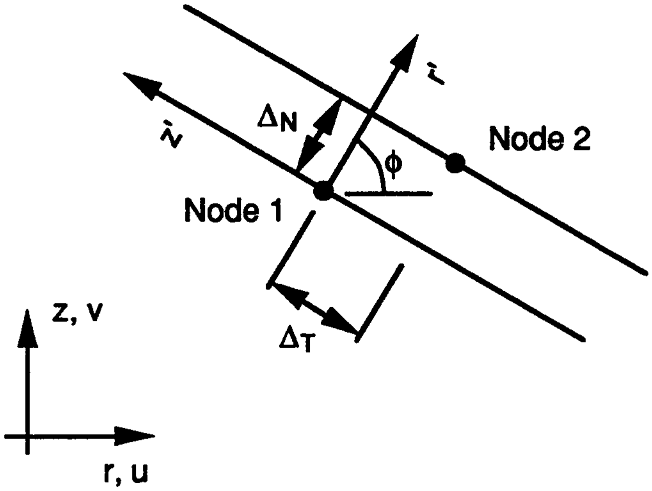

Figure 3.14 Interface geometric description

Given λ_N^i, λ_T^i, $\Delta\lambda_N$, $\Delta\lambda_T$, Δ_N^i, Δ_T^i, $d\Delta_N$, $d\Delta_T$, $[K]_{int}^i$, $\{\Delta Q\}_{int}^i$

1) Obtain trial constraint forces and gap displacements

$$\lambda_N^{i+1} = \lambda_N^i + \Delta\lambda_N$$

$$\lambda_T^{i+1} = \lambda_T^i + \Delta\lambda_T$$

$$\Delta_N^{i+1} = \Delta_N^i + d\Delta_N$$

$$\Delta_T^{i+1} = \Delta_T^i + d\Delta_T$$

2) Update interface state and "stiffness" matrix

$[K]_{int}^i \Rightarrow [K]_{int}^{i+1}$ **Tables 3.1, 3.2**

3) Update "load" vector

$\{\Delta Q\}_{int}^i \Rightarrow \{\Delta Q\}_{int}^{i+1}$ **Table 3.3**

Steps 1-3 obtain λ_N^{i+1}, λ_T^{i+1}, Δ_N^{i+1}, Δ_T^{i+1}, $[K]_{int}^{i+1}$, $\{\Delta Q\}_{int}^{i+1}$

Figure 3.15 Implementation procedure for interface element

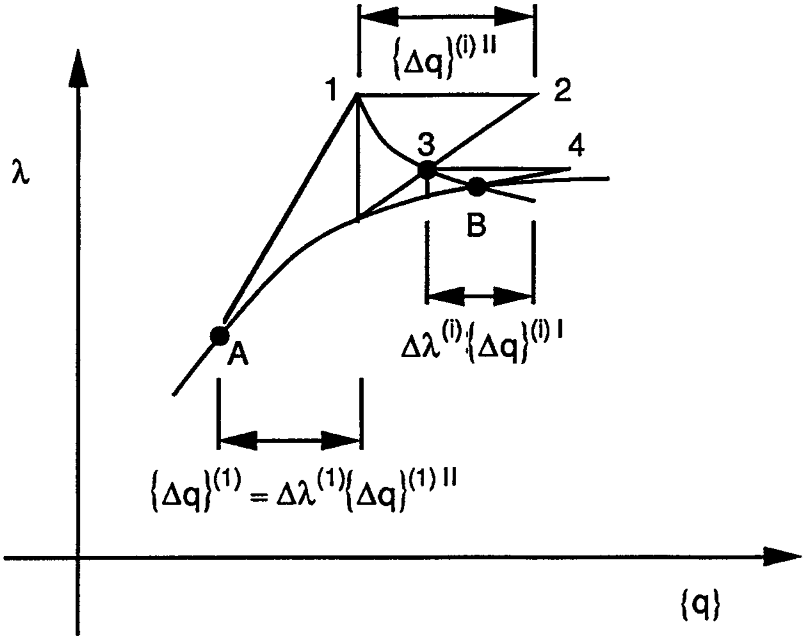

Figure 3.16 Displacement control method in global displacement space

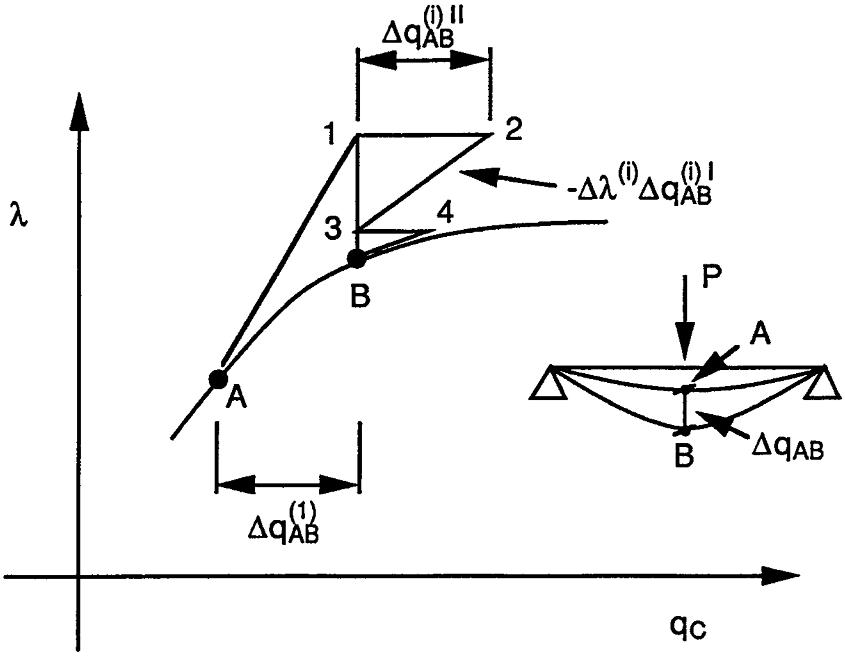

Figure 3.17 Displacement control method in local displacement space

Given $\{R^*\}$, Δq_{AB}

1) $[K]^{(1)}\{\Delta q\}^{(1)I} = \{R^*\} \Rightarrow \Delta q_{AB}^{(1)I}$

2) $\Delta\lambda^{(1)} = \dfrac{\Delta q_{AB}}{\Delta q_{AB}^{(1)I}}$ **Equation 3.49**

3) $\{P\} = \{P\} + \Delta\lambda^{(1)}\{R^*\}$

$\{q\} = \{q\} + \Delta\lambda^{(1)}\{\Delta q\}^{(1)I}$

4) **Update** $[K]^{i}$, $\{\Delta Q\}^{(i)}$

5) $[K]^{(i)}\{\Delta q\}^{(i)I} = \{R^*\} \Rightarrow \Delta q_{AB}^{(i)I}$

6) $[K]^{(i)}\{\Delta q\}^{(i)II} = \{\Delta Q\}^{(i)} \Rightarrow \Delta q_{AB}^{(i)II}$

7) $\Delta\lambda^{(i)} = -\dfrac{\Delta q_{AB}^{(i)II}}{\Delta q_{AB}^{(i)I}}$ **Equation 3.50**

8) $\{P\} = \{P\} + \Delta\lambda^{(i)}\{R^*\}$

9) $\{q\} = \{q\} + \Delta\lambda^{(i)}\{\Delta q\}^{(i)I} + \{\Delta q\}^{(i)II}$

10) **Go to 3. Iterate until desired accuracy is obtained.**

Obtain $\{P\}$, $\{Q\}$.

Figure 3.18 Flowchart of displacement control method

4.0 FINITE ELEMENT ANALYSIS OF ICE RESISTING WALLS

4.1 Introduction

The constitutive models for steel, concrete, and interface elements have been implemented into a finite element code for two dimensional structural analysis. The finite element code, SINAAPS, (an acronym for the Static Incremental Nonlinear Analysis of Axisymmetric and Planar Structures) represents a modification of the previous FEPARCS (Finite Element Program for the Analysis of Reinforced Concrete Structures) code developed by Elwi and Murray (1980). Major enhancements have been added to the code, including the ability to trace post-peak load-deformation responses by using the displacement control method (Elwi, 1990).

Three different test series were chosen for the verification of the finite element model. These included the C-FER CF test series, the C-FER TF test series (Zimmerman and Stephens, 1990), and the VTT test series (Hassinen, et al., 1989). The combination of the three test series encompasses a variety of loading types and boundary conditions which may be encountered in the field.

The chapter layout is as follows. Firstly, the three test series are described in greater detail. Next, the finite element models of selected walls from each series are presented. Results from the analyses are then described and compared with test results in Chapter 5.

4.2 Test Series Description

4.2.1 CF Series

The CF series represents a total of fourteen 1/4 scale beam specimens which were tested by Mr. Tom Zimmerman of C-FER, as part of his Ph.D. thesis research at the Department of Civil Engineering, University of Alberta. Figure 4.1 shows the general configuration of a typical test specimen. The top and bottom plates are connected by welds to a series of continuous vertical diaphragm plates. Concrete infill was then placed between the shear cells to form the composite wall.

Figure 4.2 shows the test frame used to load the beam specimens. The specimen is loaded along the bottom plate by a series of 45 tonne hydraulic loading jacks which bear against a large concrete reaction beam. The beam is then supported at two points against a steel reaction head tied down to the concrete block. Loading jacks were placed along the ends of the specimens in order to simulate continuity at the supports. Roller bearings were used for the loading jacks so that the loading would stay normal to the top plate surface. Roller bearings were used at reaction points so that the reactions were vertical at all times.

Figure 4.3 shows the basic configuration of all the specimens in the CF series, and Table 4.1 is a brief summary of all the series results. The series represents a variety of different concrete strengths, plate thicknesses, and span to depth ratios. As the specimens were loaded, large diagonal cracks appeared in the cells adjacent to the supports. These shear cracks caused little degradation in the wall stiffness. As well, a flexural crack occured in the midspan region. Shear failures, reported for all specimens except CF-2, were initiated by concrete crushing in the support vicinity, followed by general crushing and cracking distributed throughout the cells adjacent to the support. After the peak load was reached, the load gradually decreased until a residual load level was reached. Figure 4.4 shows a typical failed specimen, and Figure 4.5 is a typical load versus midspan deflection plot. The ultimate load for all walls except Specimen CF-8 was reached before the bottom steel plate yielded. Residual strengths after the peak load was reached varied from 50-98%.

After examination of the test results, it was decided to perform analyses on specimens CF-4, CF-5, CF-8, and CF-13. Specimen CF-4 was the first wall analysed, and is similar in loading and geometry to specimens CF-6 and CF-7. Specimen CF-5, which had a relatively low compressive strength of 36.3 MPa, was chosen to see whether the model could accurately determine the influence of concrete strength on the peak load. Specimen CF-8 represents a change in stiffener spacing near the support, and has properties which are similar to specimen CF-11. Lastly, specimen CF-13 represents a change in loading geometry, and is similar to specimen CF-14.

A number of walls were not considered for analysis. Specimens CF-1 to CF-3 were excluded because the beam rollers were set on Teflon pads, which provided in-plane restraint. The magnitude of these restraint forces would be difficult to estimate. Specimen CF-10 was rejected since extra shear reinforcement was provided in the shear cells, rendering the modelling difficult. Since the models were restricted to symmetric loading, specimen CF-9 was excluded. It was felt that CF-8 would be representative of the effect of stiffener spacing, hence specimen CF-12 was not analysed.

It is felt that analysis of the four walls mentioned above is representative of eight of the fourteen walls tested.

4.2.2 TF Series

The TF series was a research program conducted by C-FER (Zimmerman and Stephens, 1990) to assess the effect of combined in-plane and transverse loading on shear capacity. Eight wall specimens were tested in all. Figure 4.6 is a typical TF ice wall specimen. The configuration is similar to that of the CF series, except that the wall specimen is welded to a pair of steel legs filled with concrete which are meant to simulate the effects of bulkheads. In addition, a pair of tie-down plates are placed at the ends of the specimen to maintain support continuity. The specimen is attached to a loading reaction frame, as shown in Figure 4.7. The reaction frame is a sequence of two large C sections welded together, and can accommodate both tensile and compressive in-plane loads applied by eight 60 tonne hydraulic jacks. Transverse loading was applied by using a distribution beam which transferred load from the MTS loading head to a series of roller assemblies on the specimen. A series of rollers was used at the load reaction points for TF-1 to TF-4, and is shown in Figure 4.8a. Because an uneven load distribution was obtained from this setup, a more sophisticated roller setup was used for TF-5 to TF-8 (see Figure 4.8b). The second roller setup included a rocker assembly to allow for joint rotation as well as translation.

The specimens were first subjected to in-plane loading, then transverse loading was applied. Stroke control was used so that the post-peak response could be captured.

Table 4.2 is a summary of all the series results. Specimens TF-1 to TF-4 were subjected to longitudinal in-plane loading, while specimens TF-5 to TF-8 were subjected to tensile loading. The failure mechanism was much the same as for the CF series, with diagonal cracking and crushing occuring in the cell adjacent to the supports and in the beam span where loading was applied. However. the first crushing did not always take place nearest the support, but rather at the top right hand corner of the shear cell. Figure 4.9 shows a typical failed specimen. Residual strengths varied from 70% to 90%.

Three walls were analysed from this series. These included specimens TF-1, TF-2, and TF-4. The objective was to test the finite element model's ability to evaluate the effect of confining load upon shear capacity. Specimen TF-3 had no in-plane loading, and since the CF series also had no in-plane loading, it was felt that an analysis of TF-3 would be redundant.

From the test results of TF-5 to TF-8, which were subjected to tensile axial forces, it is seen that there is a small variation in the ultimate load of these specimens. This is probably because the concrete separated from the steel when the axial load was first applied and thus transmitted no tensile axial force through the concrete. Hence, the concrete would act as though no axial load was imposed, and the ultimate load would be similar to a specimen with no in-plane load if the specimen failed in shear. Comparing the ultimate loads of TF-5 to TF-8 with TF-3 confirms this.

4.2.3 VTT Series

The VTT test series was conducted at the Technical Research Centre of Finland (Hassinen, et. al., 1989), and consists of four composite ice walls. The intent was to determine the ultimate capacity of a specific wall configuration, shown in Figure 4.10, under static and cyclic loading.

Figure 4.11 shows the loading apparatus used in the testing. Two concentrated loads were applied by means of a distribution beam which transferred the load to two rollers. Rollers were also used at the beam reaction points. The cyclic loading was applied for 2000 cycles at a load range of 800 kN.

Table 4.3 summarizes the series results. It is seen that, since the specimens were of near identical geometry and material properties, the failure loads are similar for the static tests. It is also observed that the cyclic loading tests show no decrease in strength due to fatigue. Failures occurred in shear which were similar to both the CF and TF series.

Since all tests were nearly identical, it is only necessary to perform one analysis in the VTT series. Specimen VTT3 was chosen as the representative wall.

4.3 Finite Element Models

4.3.1 General

The determination of proper material properties for concrete and steel require extensive testing. However, the three test series described above reported a limited amount of material data. Hence, it is necessary to use empirical relationships between the reported and undetermined parameters to obtain estimates for a complete description.

For concrete, a large amount of empirical data exists relating the concrete uniaxial strength, f'_c, and other material data. The initial modulus of elasticity is estimated by using the ACI equation (ACI, 1989)

$$E = 5000\sqrt{f'_c}. \qquad [4.1]$$

MacGregor (1988) determined that the multiplying factor of 5000 should be modified to 4400 in the Edmonton area to account for local aggregate stiffnesses. This modified value is adopted here in the CF, TF, and VTT series, even though the VTT series was conducted in Finland. It was felt that the error introduced into the VTT series results would be small.

The uniaxial strain corresponding to the ultimate stress, ε_c, shows little variation with changing f'_c (ACI, 1982). Typical values range between 0.002 to 0.003. A value of 0.0025 was chosen here.

The uniaxial tensile strength, f'_t, is usually hard to determine experimentally, and is usually, approximately, taken as

$$f'_t = 0.33\sqrt{f'_c}. \qquad [4.2]$$

To complete the description of the Willam and Warnke (1975) strength surface, it is necessary to obtain the biaxial strength and strain, f_{cb} and ε_{cb}, and the high strength and strain points. In the absence of any other data, values from Elwi and Murray (1980), which were developed for 40 MPa concrete, were adopted, and are listed in Figure 4.12.

Experimental values for the fracture energy in tension, G_f, are limited, and there seems to be no relationship between G_f and the tensile strength, f'_t. Tests by Gopalaratnam and Shah (1984), and Peterson (as used by Rots et. al.,1985) indicate that G_f ranges from 0.05 N/mm to 0.15 N/mm. In this study a value of 0.10 N/mm is used.

Values for the descending branch decay parameters for tension and compression are taken from Equations 3.29 and 3.34 respectively. It is noted here that the descending branch value for compression, k_c, should vary with confinement. However, test data regarding confined compressive softening is scarce, hence, the uniaxial value of k_c is assumed to be representative for confinement effects.

The mesh spacing, h_c, is uniform for a perfectly square mesh. However, for a slightly rectangular mesh, h_c differs in each direction. An area average is taken as a representative mesh spacing

$$h_c = \sqrt{h_1 h_2}, \qquad [4.3]$$

where h_1 and h_2 are Gauss point spacings in the "1" and "2" directions of Figure 4.13 respectively.

It is uncertain whether the walls are closer to conditions of plane stress or plane strain. For the CF series, the aspect ratio of specimen width to depth is approximately 1.5, which is not by itself large enough to warrant the assumption of plane strain conditions. However, the relatively thick plates which form the steel cells are used for formwork, which are able to carry transverse forces generated from restraining concrete expansion. Figure 4.14 shows the mechanism of load transfer into the plates. Because the concrete strut is in compression, expansion would occur in the transverse direction due to the Poisson effect. In order for no expansion to occur, the steel plates must restrain the concrete. Transverse forces along the steel-concrete interface act as restraint, and are transferred as frictional forces. The plates must be thick enough to carry these forces without significant yield. Although calculations have not been specifically made, it is assumed that the plates are of sufficient thickness for this to be the case. It should also be noted that the diaphragm steel plate at this point is not highly stressed in compression. This adds further confinement, and minimizes the effect of Poisson's ratio in the steel plate.

The TF and VTT series have plates which are much less stocky. However, the width to depth aspect ratio is approximately 3 for both test series. This may be sufficient to approximate plane strain conditions.

It is suggested here that the final test of the assumption of plane stress/plane strain lies in the comparison of analytical results with test data.

4.3.2 Loads and Boundary Conditions

Figure 4.15 shows the finite element mesh used for specimens CF-4 and CF-5. Because of symmetry, only one half of the wall needs analysis. Eight noded quadratic isoparametric elements were used with a 3X3 Gauss integration order. Loading from the hydraulic jacks was applied as a series of pressure loads on the top steel plate. To simulate shear transfer across the steel-concrete interface, the elements were double noded at those points, and gap elements of the type described in Chapter 3 were placed there. The concrete cores are thus connected to the steel plates by means of gap elements. If all gap elements were to separate, the problem would become numerically unstable. To avoid this situation, a number of fixed points were used to keep the core inside the steel plates, shown in Figure 4.15. At the support, a stiff plate was placed to represent the use of a 75 mm bearing plate. Similar configurations were generated for specimens CF-8 and CF-13, shown in Figures 4.16 and 4.17 respectively.

The finite element mesh for the TF series is shown in Figure 4.18. Since the end caps were fairly thick, in-plane loads were placed on the specimen ends as uniform pressure loading. To conform with experimental procedure, the in-plane loading was imposed before transverse loading was applied. Since the specimen legs were fairly stocky, and no failure in this region was observed for any of the experiments, the legs were idealized as a series of linear elastic elements. This also resulted in considerable geometric simplification of the model. Instead of a series of rollers, one roller was used at the support. This was because portions of the legs tended to lift off some of the rollers as the legs translated with increased transverse loading. This means that the support region would partially rotate as well as translate. It was also felt that the flexural stiffness of the legs would have a negligible influence on the stiffness and failure load of the specimen. Rollers were placed at the tie-down positions to simulate the deformation restraint occuring there.

Figure 4.19 is the finite element mesh used for the VTT series. Since the specimens were simply supported with no overhanging loads, the end caps were neglected in the analysis. This proved to be an unwise decision, as will be discussed in Chapter 5. Although bearing plates were used at the supports, they were not included in the analysis for similar reasons.

The formulation used in the analysis consisted of small displacement and infinitesimal strains. It was felt that there was not significant catenary action developed in any of the tests within the deformation range tested. Some of the tests, however, showed large rotations in the steel plate closest to the support after the onset of shear failure. This took place at a sufficiently advanced loading stage not to have had much effect on analysis.

The solution strategy employed was exclusively displacement control for all specimens with the exception of the TF series. In the TF series, the in-plane loads were applied using a standard Newton-Rhapson technique, and the transverse loads were then imposed using displacement control. The vertical displacement at the wall center at the plate top was used as the control displacement. Loading was applied in the form of displacement increments of 1 mm; this was felt to be adequately small enough to capture essential behavioural characteristics. Relative load and displacement norms, λ_{load} and λ_{disp}, were used as convergence criteria:

$$\lambda_{disp} = \sqrt{\frac{\langle \Delta q \rangle \{\Delta q\}}{\langle q \rangle \{q\}}}, \qquad [4.4]$$

$$\lambda_{load} = \sqrt{\frac{\langle \Delta Q \rangle \{\Delta Q\}}{\langle R \rangle \{R\}}}, \qquad [4.5]$$

where Δq and q represent incremental and total displacements respectively, and ΔQ and R are incremental and arc length reference loads respectively. Values of 0.05 were used for both load and displacement norms.

Table 4.4 is a summary of the basic input parameters used in the analysis of the eight walls. In order to facilitate numerical stability when steel yielding was encountered, a hardening slope of 0.02E was used. Specimen CF-4 was analysed using three different Gauss integration orders, 2x2, 3x3, and 4x4. This was done in order to verify the objectivity of the proposed post-peak constitutive model developed here. A friction coefficient of 0.5773 was used for the steel-concrete interface in all analyses, corresponding to a friction angle of 30° as supported by Kennedy and Cheng (1987).

4.4 Execution

It is of practical interest to describe the pre- and post- processing strategy utilized to model the problems, and to generate the results. Figure 4.20 is a flowchart showing the sequence used in model generation, analysis, and results processing. The general purpose pre- and post processing program PATRAN (PDA, 1991) was used to generate the model finite element meshes, loadings, and material properties. The program PATRAN allows for a fast and efficient means of generating complex geometric models. The model description is written into an ASCII file called a neutral file. The ASCII format was used in order to maximize portability between different computing platforms. The neutral file must be translated into a format readable to the SINAAPS finite element program. This is performed by using a translator program named PATSI developed by the writer which reads the PATRAN neutral file, and writes a SINAAPS input file. The analysis is then performed, and ASCII plot files are written. These files contain information pertaining to mesh geometry, stresses and stress history, and deflections.

The model generation and finite element analysis was performed on an Apollo DN10000 workstation at C-FER, which has significant speed and storage capabilities. The capability to output graphical information is, however, somewhat limited on the Apollo. Therefore, it was decided to use microcomputers to process the graphical information. The Macintosh was judged to be superior in generating and processing graphical results. A graphics program named SINPLOT was written by the author to read in the plotfiles and generate graphical output. The program utilizes standard PLOTLIB routines to draw deformed shapes, stress trajectories, and nonlinear effects (cracking, crushing, etc.). The drawings can then be modified for presentation by using any standard Macintosh drawing program, such as MacDraw.

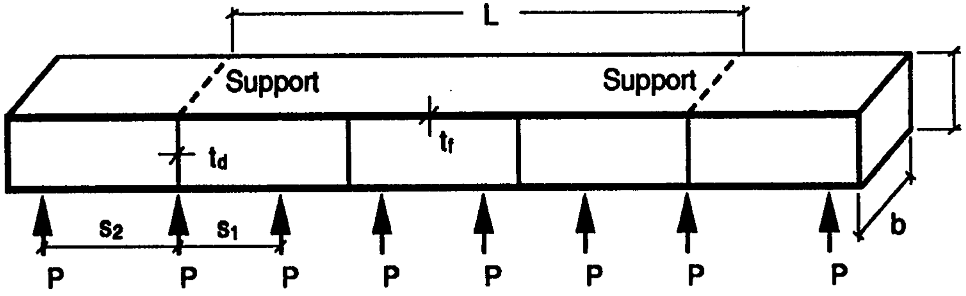

f'_c = concrete compressive strength (MPa)
f_y = steel yield strength (MPa)
P_f = failure load (kN)
w_f = equivalent uniformly distributed load (MPa)

Note: All dimensions are in mm

Specimen	f'_c	f_y	t_f	t_d	h	b	L	s_1	s_2	P_f	w_f	Failure type
CF-1	58.0	265.0	6.4	6.4	250.0	375.0	1000.0	200.0	238.0	684.0	9.12	Shear
CF-2	62.1	265.0	6.4	6.4	250.0	375.0	1000.0	200.0	238.0	617.0	8.23	Flexure
CF-3	58.8	265.0	6.4	6.4	250.0	375.0	1000.0	200.0	238.0	717.0	9.56	Shear
CF-4	53.5	371.0	12.6	6.4	250.0	381.0	1500.0	300.0	333.0	560.0	4.90	Shear
CF-5	36.3	371.0	12.4	6.4	250.0	381.0	1500.0	300.0	333.0	437.0	3.82	Shear
CF-6	57.5	352.0	10.0	6.4	250.0	381.0	1500.0	300.0	333.0	561.0	4.91	Shear
CF-7	58.4	347.0	16.1	6.4	250.0	381.0	1500.0	300.0	333.0	601.0	5.26	Shear
CF-8	59.5	371.0	12.4	6.4	250.0	381.0	1500.0	300.0	333.0	761.0	6.66	Shear
CF-9	61.0	371.0	12.5	6.4	250.0	381.0	1500.0	300.0	333.0	754.0	6.60	Shear
CF-10	54.5	401.0	9.5	6.4	250.0	375.0	1250.0	300.0	333.0	908.0	9.69	Shear
CF-11	58.2	388.0	9.5	6.4	250.0	375.0	1250.0	300.0	333.0	757.0	8.07	Shear
CF-12	56.6	398.0	9.5	6.4	250.0	375.0	1250.0	300.0	333.0	772.0	8.23	Shear
CF-13	56.0	398.0	9.5	6.4	250.0	375.0	1250.0	300.0	333.0	712.0	7.59	Shear
CF-14	60.0	398.0	9.5	6.4	250.0	375.0	1250.0	300.0	333.0	745.0	7.95	Shear

Table 4.1 Summary of test results for the CF series

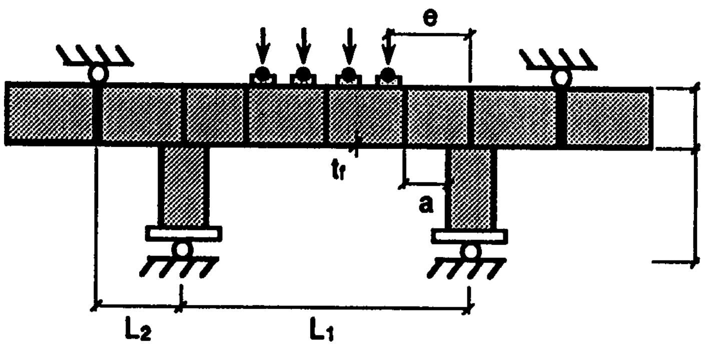

F_f = Total failure load (kN)
N = Compressive/tensile load (kN)
b = Specimen width (mm)

Notes:
1) All dimensions are in mm
2) Specimen TF-3 did not have tie downs
3) Specimens TF-6, TF-7, and TF-8 are subjected to 2 point loading (loads closest to the center omitted)
4) Specimen TF-8 fabricated with 6 mm dia. x 60 mm long headed studs welded to inner side of face plate

Specimen	f'_c	f_y	t_f	h_1	h_2	b	L_1	L_2	e	a	N	F_f
TF-1	50.0	325.0	10.2	249.0	420.0	802.0	1250.0	390.0	350.0	168.0	-1965.0	5600.0
TF-2	55.0	350.0	6.8	249.0	420.0	800.0	1250.0	390.0	350.0	174.0	-1180.0	4550.0
TF-3	62.0	350.0	6.8	251.0	420.0	799.0	1250.0	390.0	350.0	175.0	0.0	4100.0
TF-4	68.0	350.0	6.8	249.0	420.0	799.0	1250.0	390.0	350.0	176.0	-3145.0	5876.0
TF-5	52.0	372.0	6.4	252.0	420.0	799.0	1250.0	390.0	350.0	175.0	1000.0	4130.0
TF-6	54.0	372.0	6.4	251.0	420.0	801.0	1250.0	390.0	330.0	175.0	2000.0	4200.0
TF-7	55.0	372.0	6.4	250.0	420.0	801.0	1250.0	390.0	354.0	174.0	3000.0	3990.0
TF-8	55.0	372.0	6.6	251.0	420.0	800.0	1250.0	390.0	351.0	175.0	2000.0	4100.0

Table 4.2 Summary of test results for the TF series

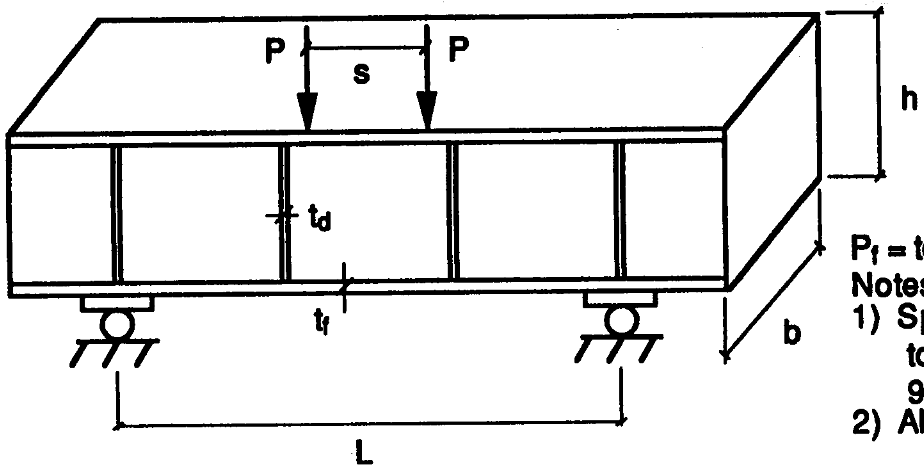

P_f = total failure load (kN)

Notes:

1) Specimens VTT2 and VTT4 were subjected to 2000 load cycles, varying in intensity from 900 to 1700 kN.
2) All dimensions are in mm.

Specimen	f'_c	f_y	t_f	t_d	h	b	L	s	P_f
VTT1	54,4	364.0	8.0	6.1	216.0	600.0	910.0	200.0	2003.0
VTT2	54.4	364.0	8.0	6.1	216.0	600.0	910.0	200.0	2198.0
VTT3	52.7	364.0	8.0	6.1	216.0	600.0	910.0	200.0	1869.0
VTT4	52.7	364.0	8.0	6.1	216.0	600.0	910.0	200.0	1965.0

Table 4.3 Summary of test results for the VTT series

Specimen	Concrete						Steel		
	f'_c	E	f'_t	k_t	h_c	k_c	f_y	E	E_h
CF-4	53.5	32200	2.41				371.0	200	4
2x2				881.6	36.6	88.2			
3x3				592.3	24.5	66.3			
4x4				437.7	18.2	49.1			
CF-5	36.3	26500	1.99	488.4	24.5	43.0	371.0	200	4
CF-8	59.5	33900	2.55	546.5	21.4	56.4	371.0	200	4
CF-13	56.0	33000	2.47	606.1	24.5	65.6	370.0	200	4
TF-1	50.0	31100	2.33	538.0	23.1	56.0	325.0	200	4
TF-2	55.0	32600	2.45	565.7	23.1	62.0	350.0	200	4
TF-4	68.0	36300	2.72	628.1	23.1	67.6	350.0	200	4
VTT-3	52.7	32000	2.40	432.0	18.0	45.8	364.0	200	4

f'_c = uniaxial compressive strength (MPa)
E = elastic modulus (MPa)
f'_t = uniaxial tensile strength (MPa)
k_t = tensile decay parameter
h_c = effective sampling point spacing (mm)
k_c = compressive decay parameter
f_y = steel yield strength (MPa)
E_h = steel hardening modulus (MPa)

Table 4.4 Summary of base material parameters for analyses

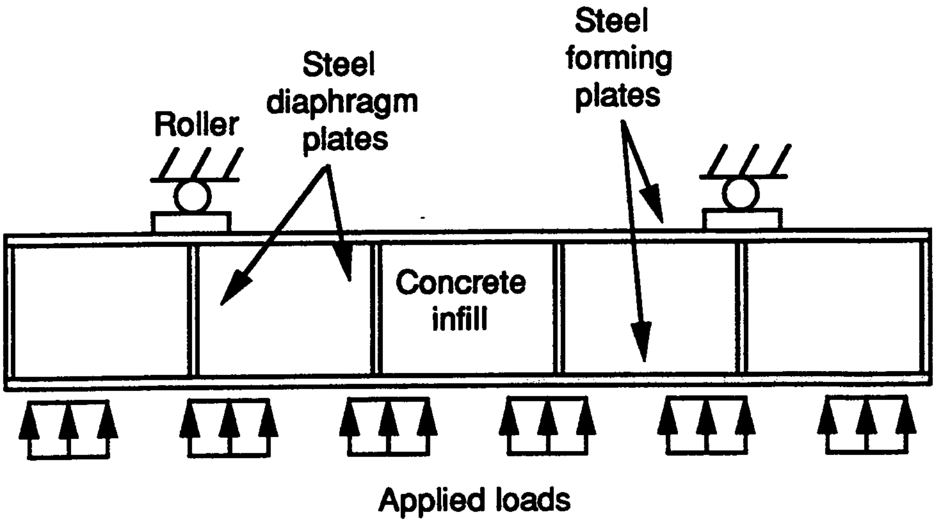

Figure 4.1 Typical CF series ice wall specimen

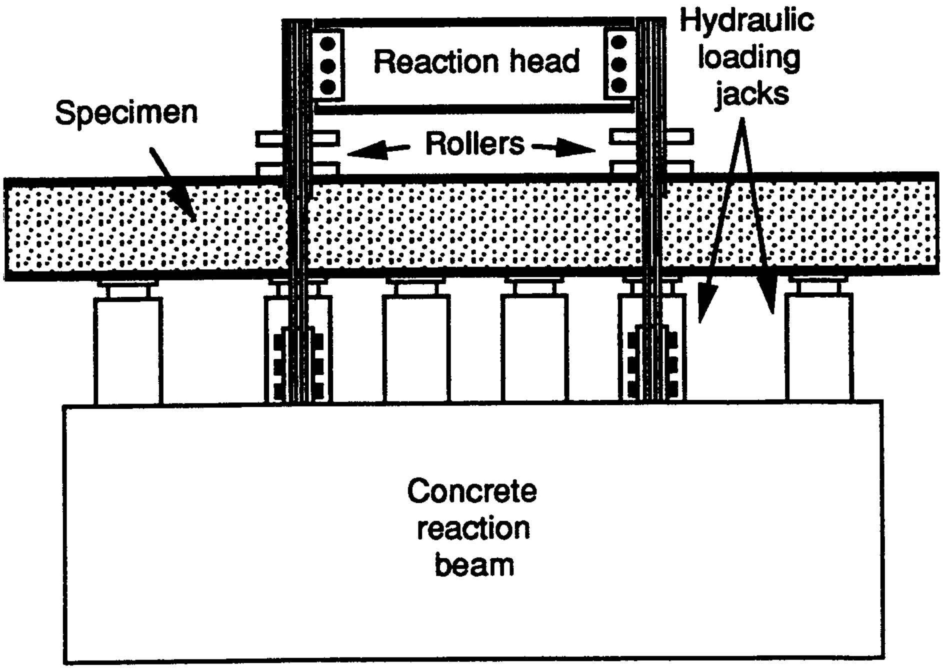

Figure 4.2 Schematic of beam testing frame

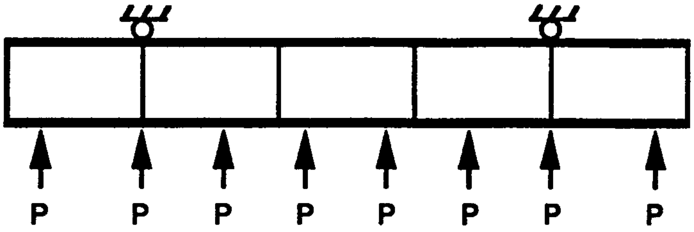

Specimens CF-1, CF-2, CF-3

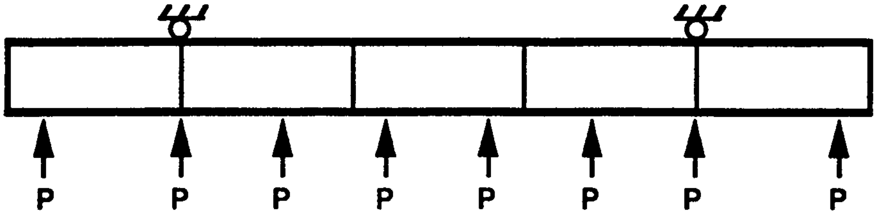

Specimens CF-4, CF-5, CF-6, CF-7

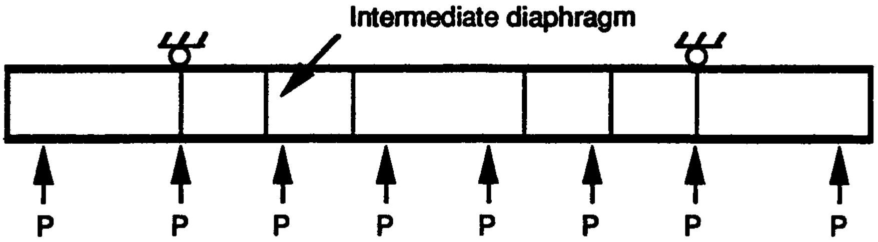

Specimen CF-8

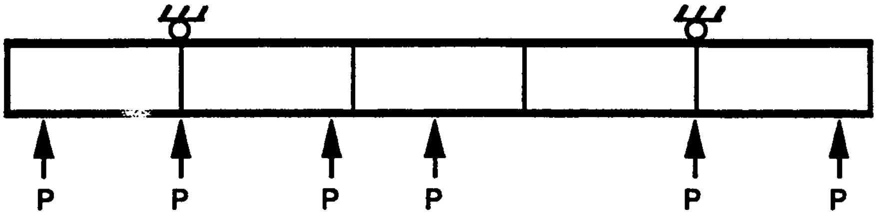

Specimen CF-9

Figure 4.3 CF test series

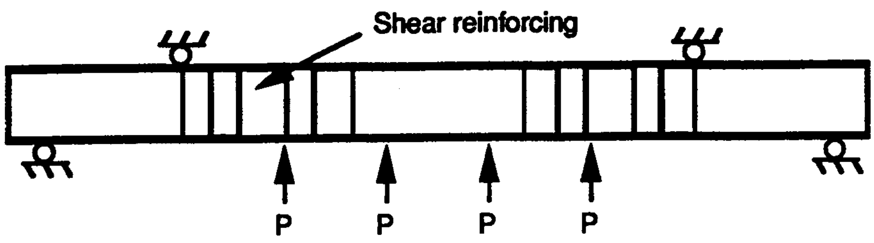

Specimen CF-10

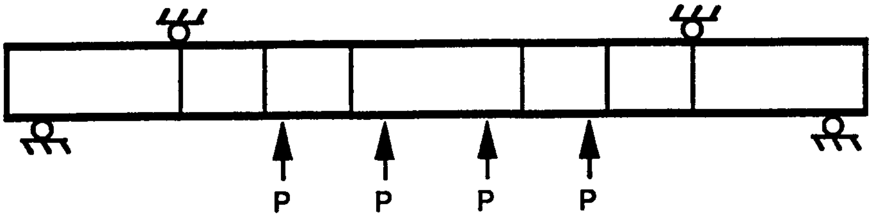

Specimen CF-11

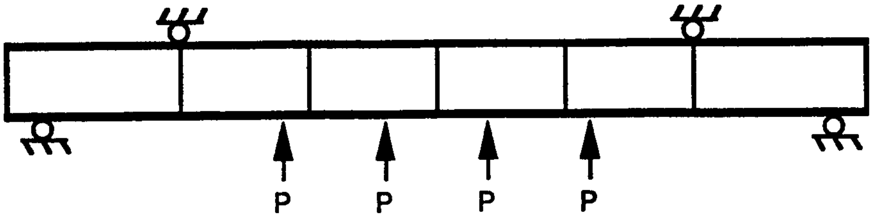

Specimen CF-12

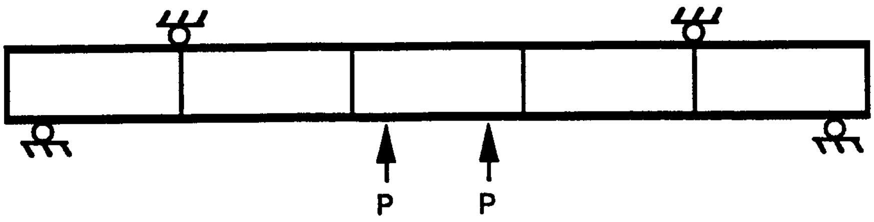

Specimens CF-13, CF-14

Figure 4.3 CF test series

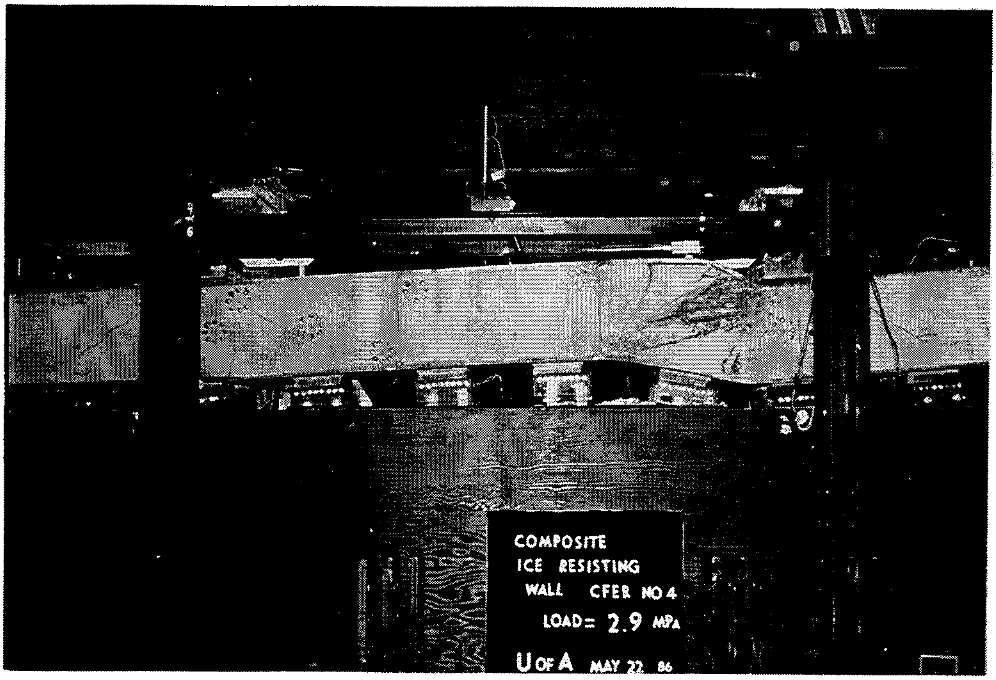

Figure 4.4 Typical failed specimen

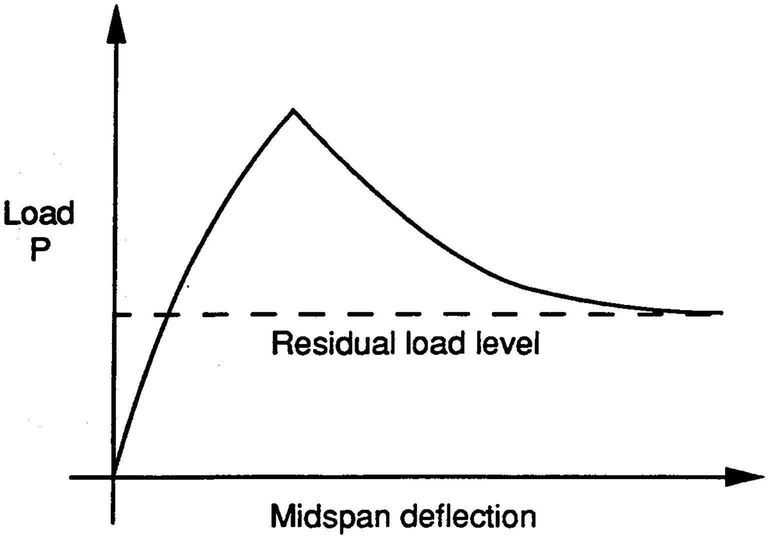

Figure 4.5 Typical load versus midspan deflection plot for CF series

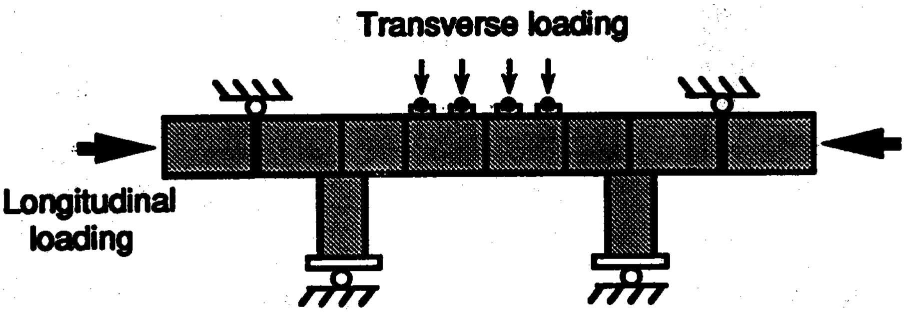

Figure 4.6 Typical specimen from the TF series

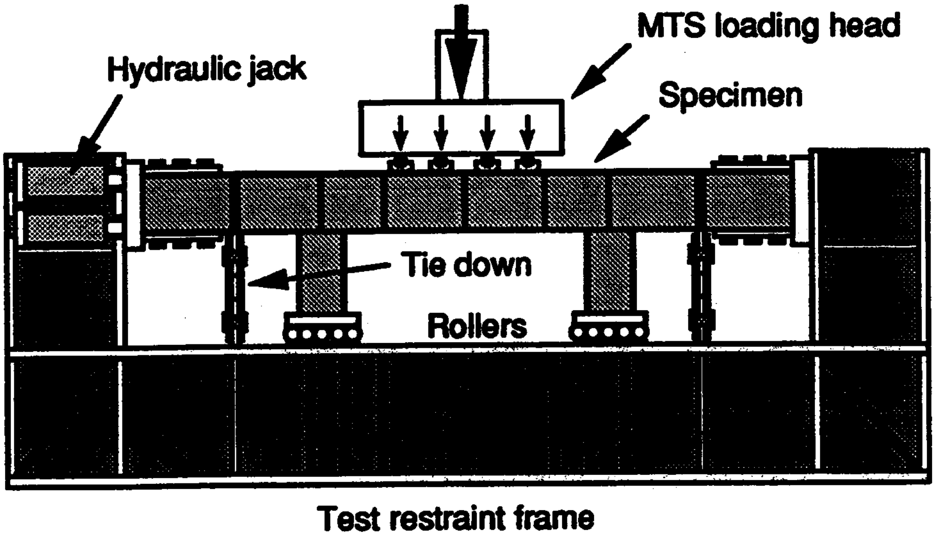

Figure 4.7 Schematic of test frame for TF series

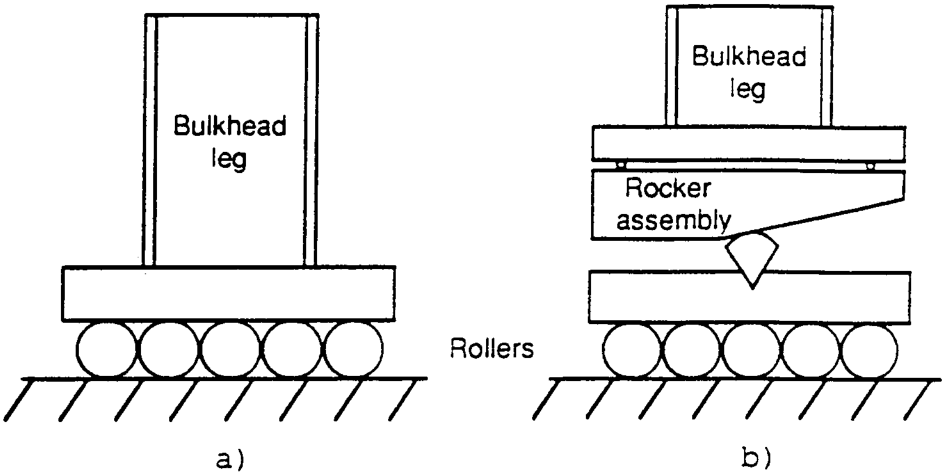

Figure 4.8 Typical roller assemblies

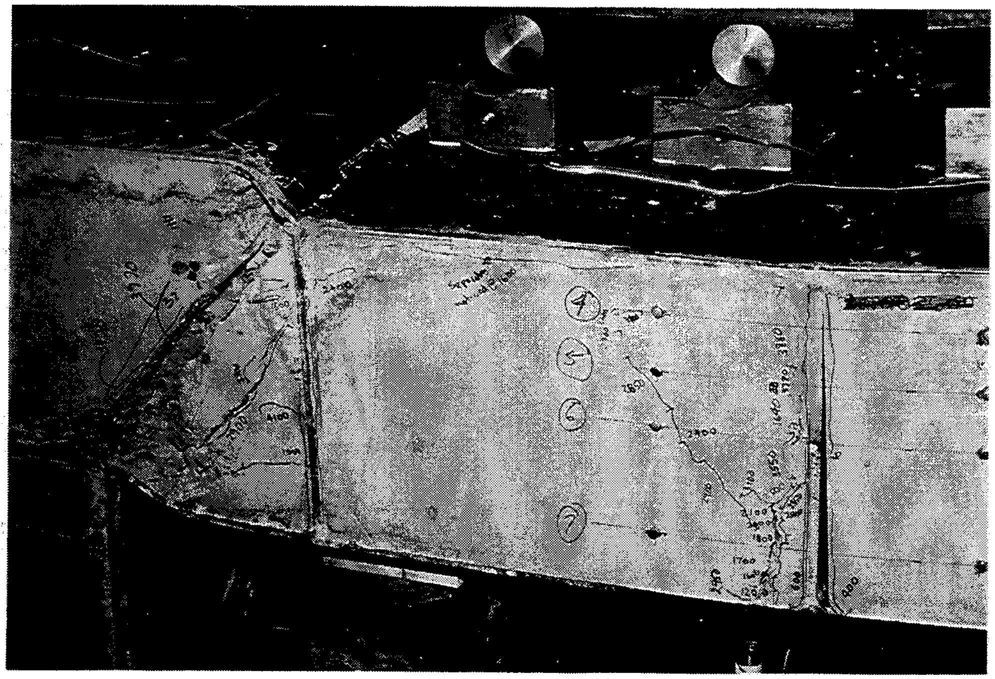

Figure 4.9 Typical failed specimen

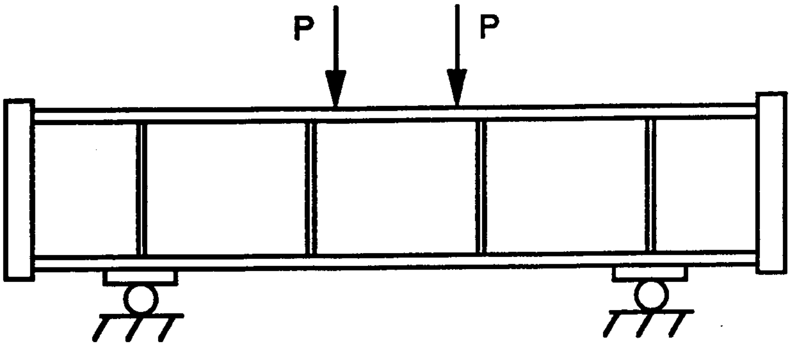

Figure 4.10 Typical VTT series specimen

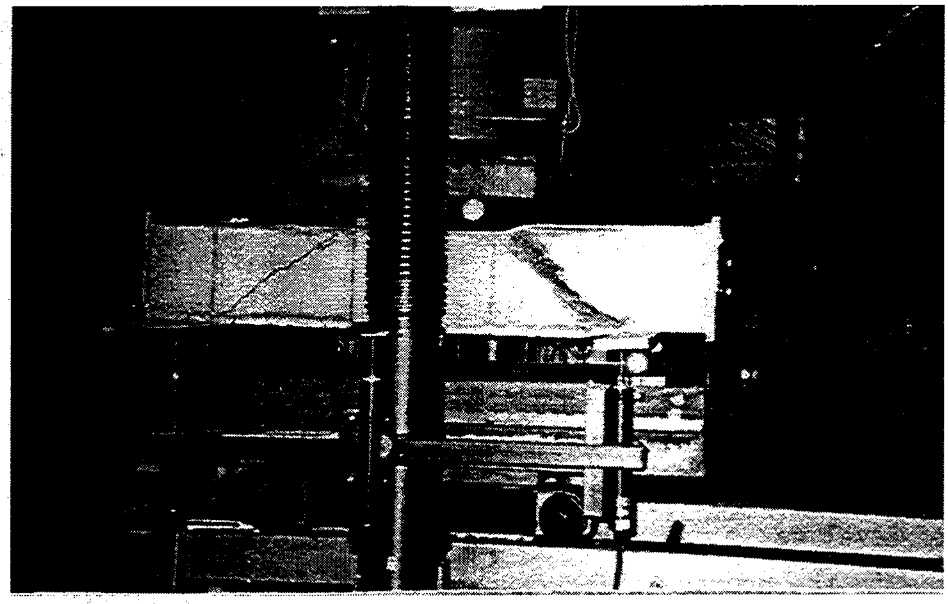

Figure 4.11 Loading apparatus and failed specimen

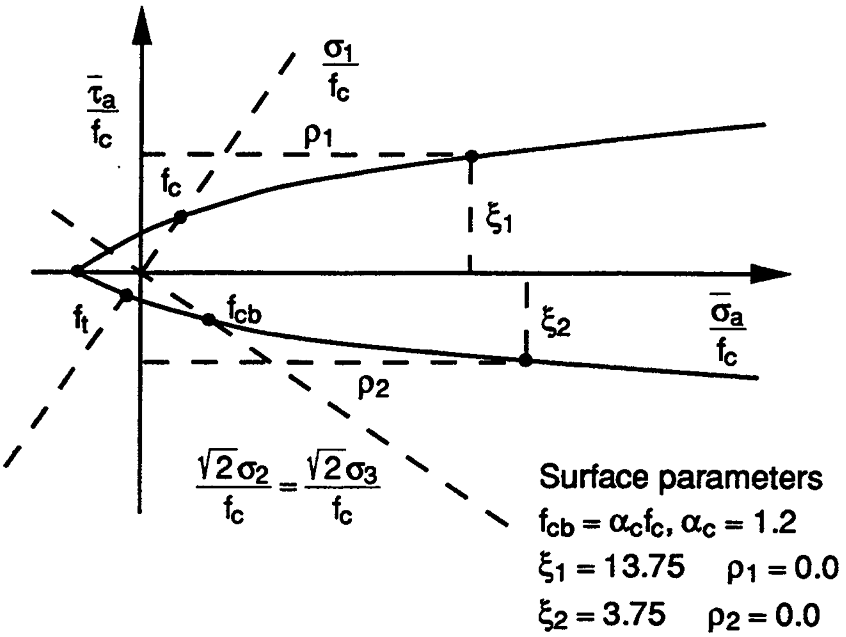

Surface parameters
$f_{cb} = \alpha_c f_c, \alpha_c = 1.2$
$\xi_1 = 13.75 \quad \rho_1 = 0.0$
$\xi_2 = 3.75 \quad \rho_2 = 0.0$

Figure 4.12 Strength surface parameters

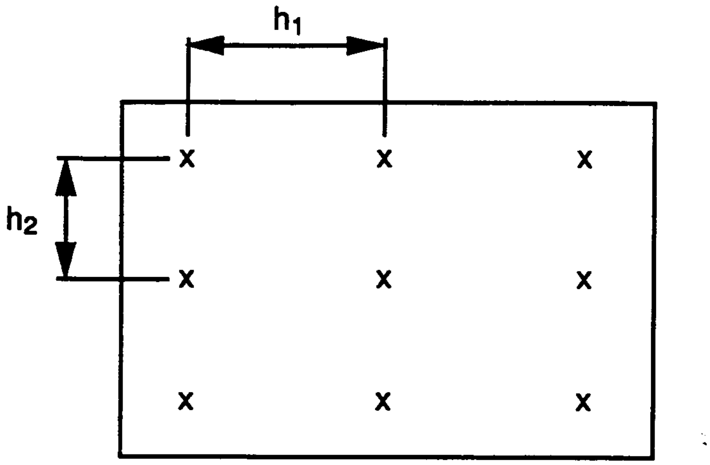

$h_c = \sqrt{h_1 h_2}$

Figure 4.13 Mesh spacing convention

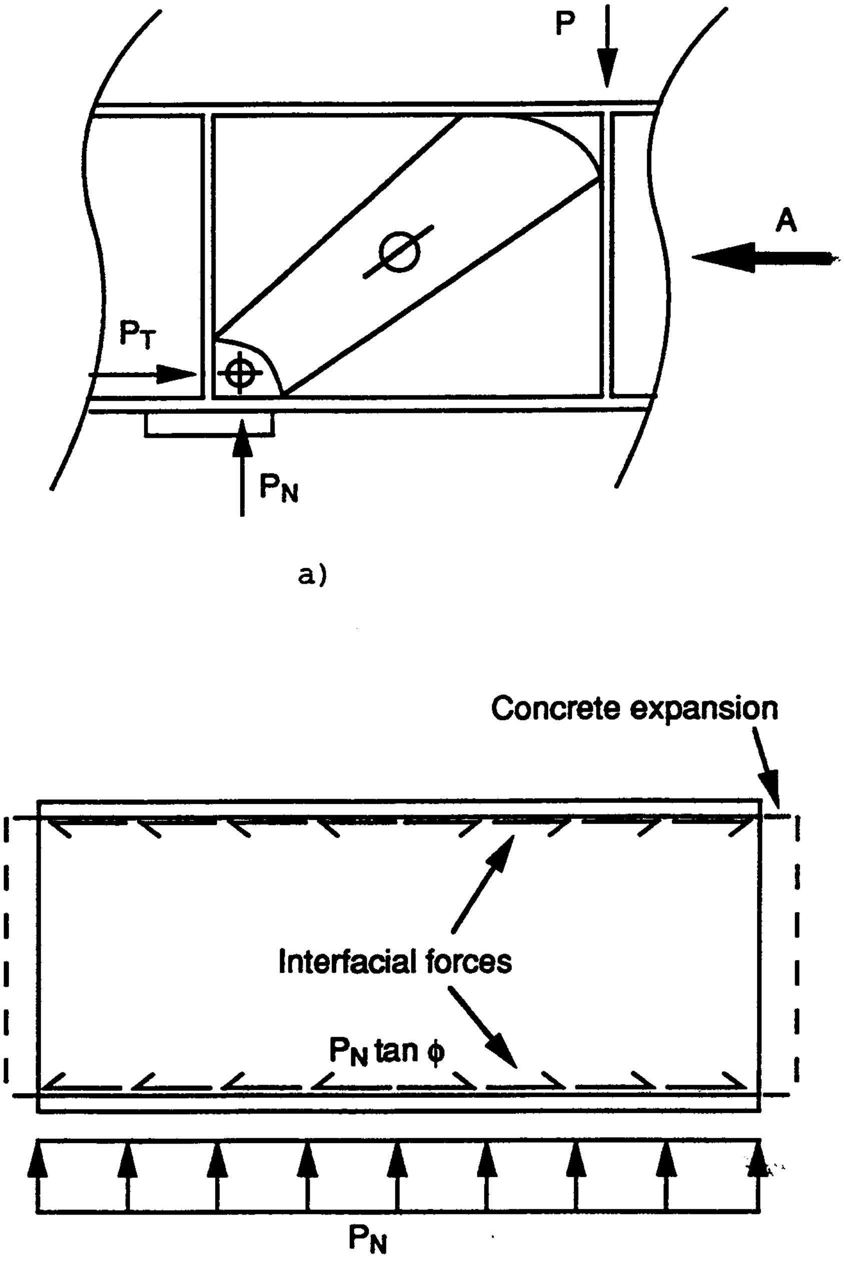

a)

b) View A

Figure 4.14 Plane strain argument

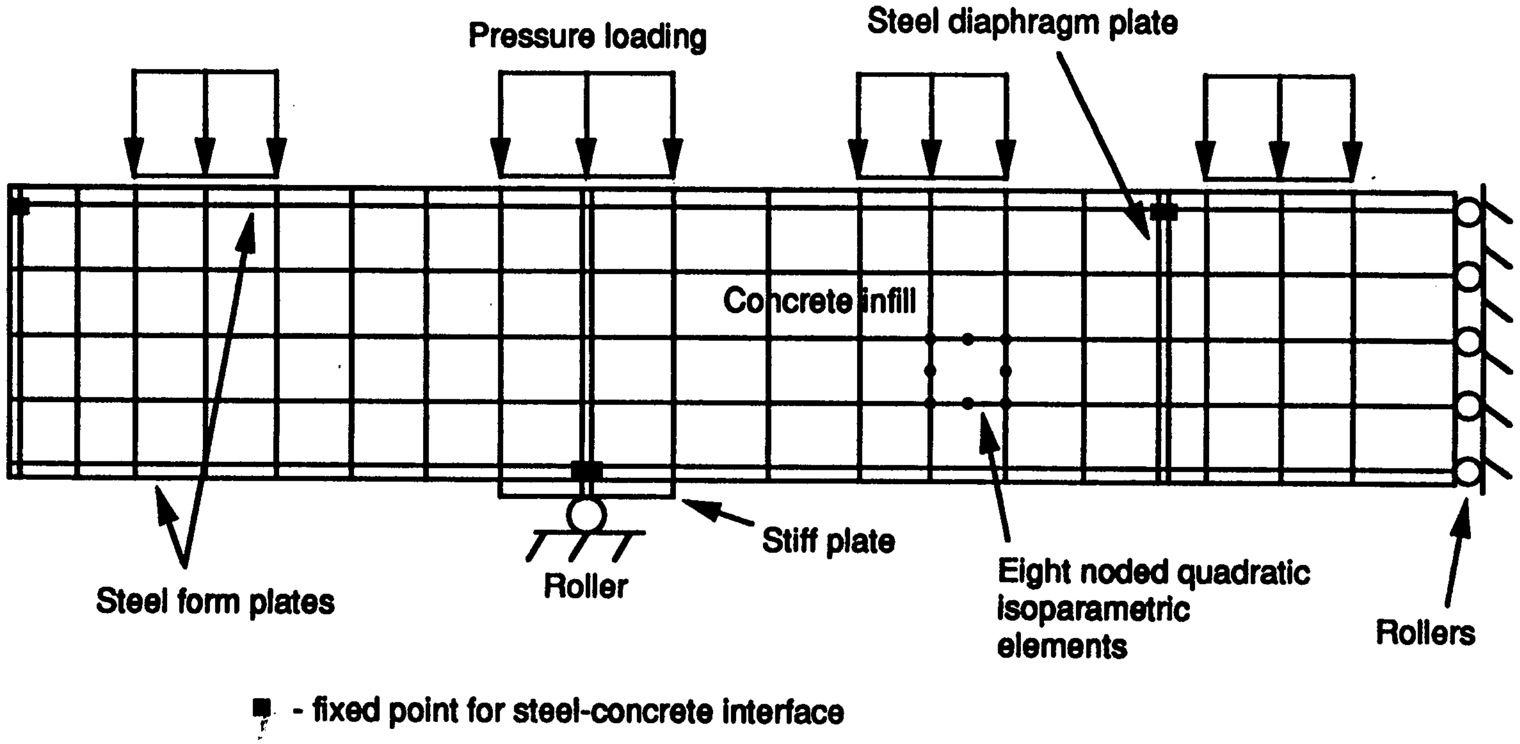

Figure 4.15 Mesh layout for Specimens CF-4, CF-5

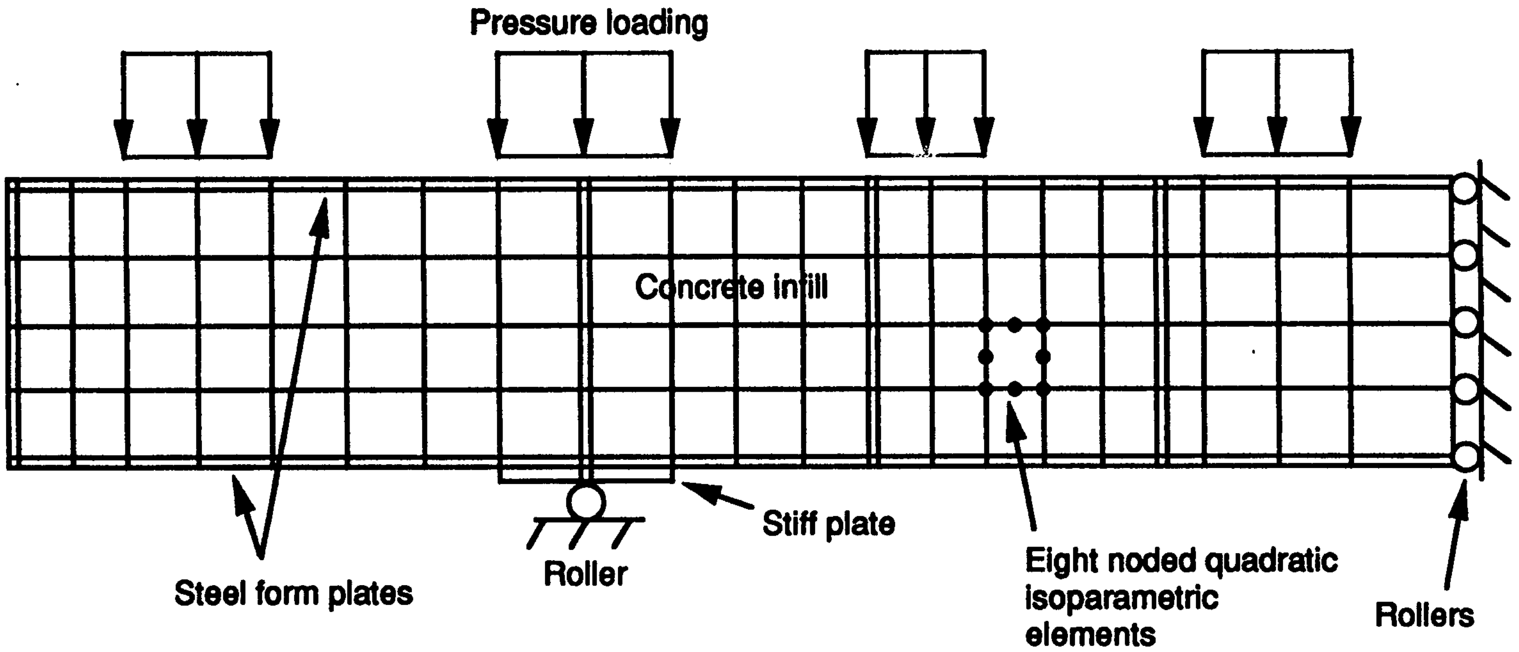

Figure 4.16 Mesh layout for Specimen CF-8

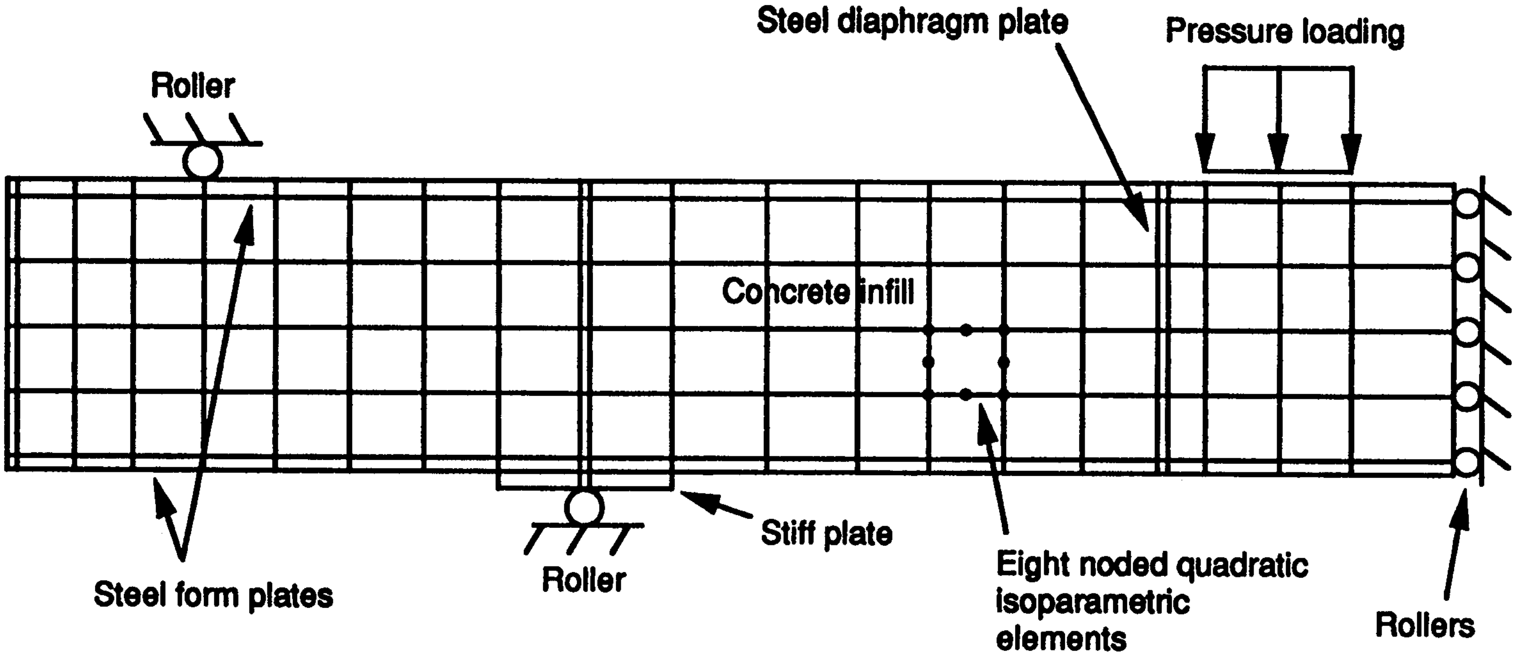

Figure 4.17 Mesh layout for Specimen CF-13

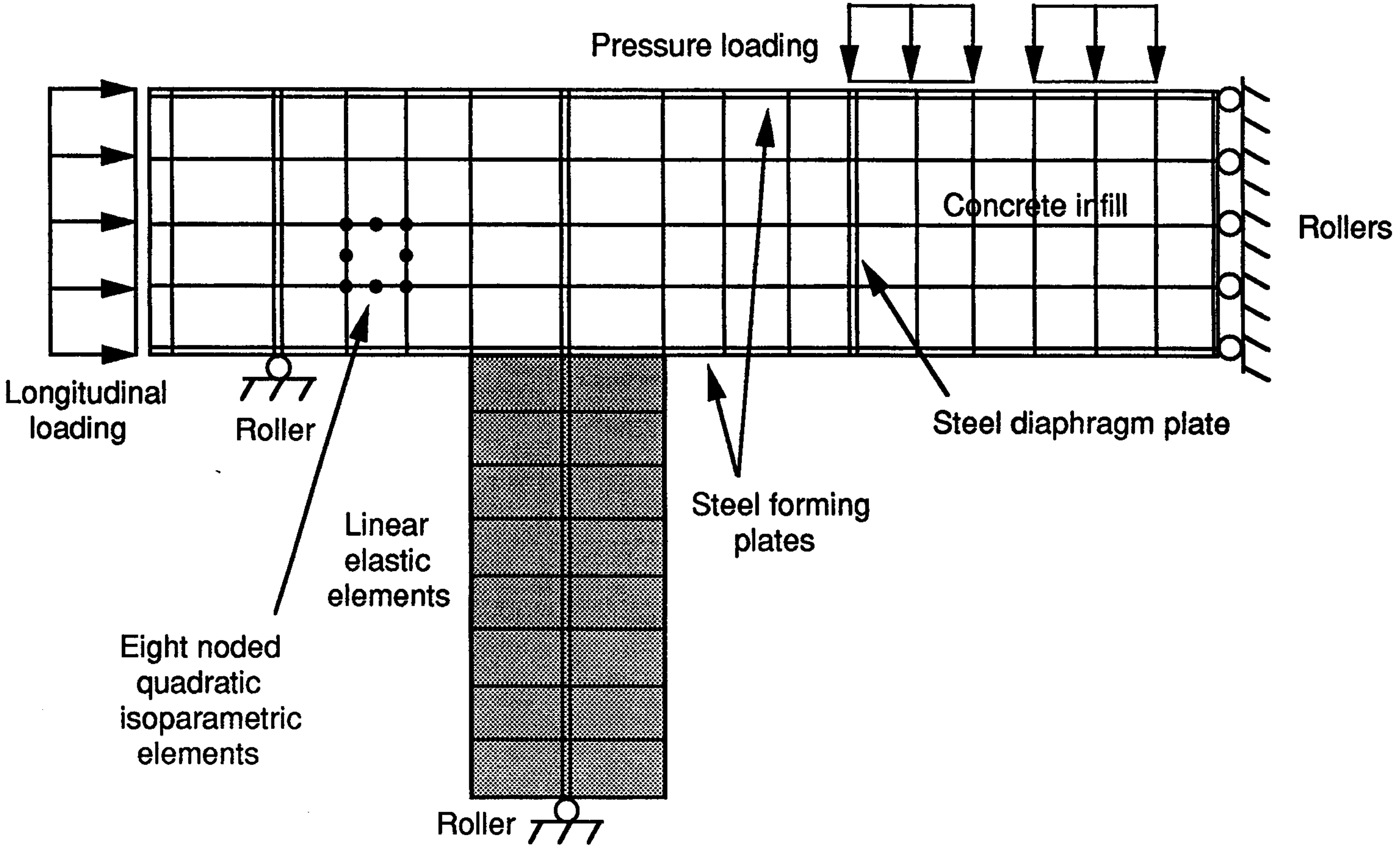

Figure 4.18 Mesh layout for Specimens TF-1, TF-2 and TF-4

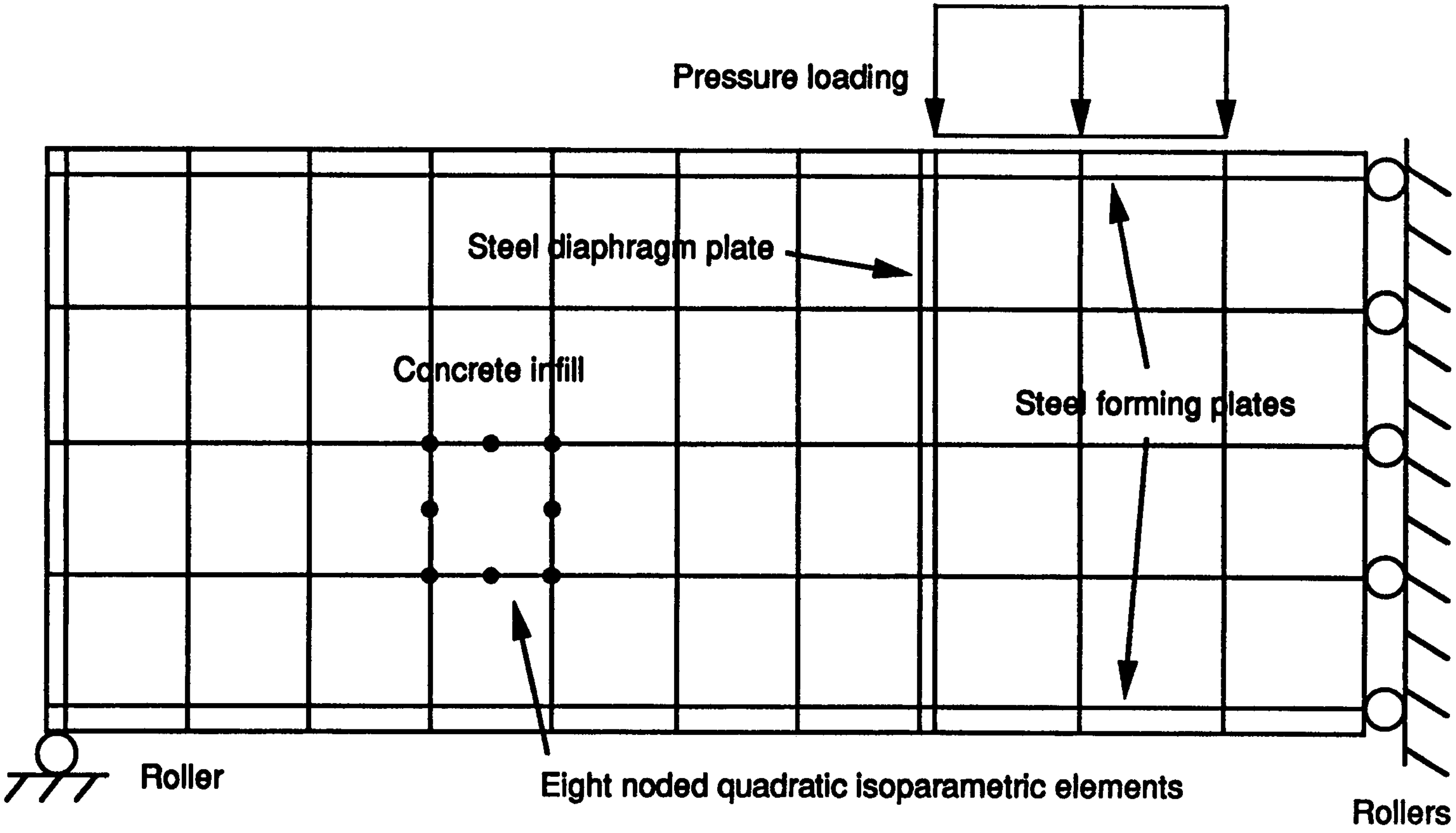

Figure 4.19 Mesh layout for Specimen VTT-3

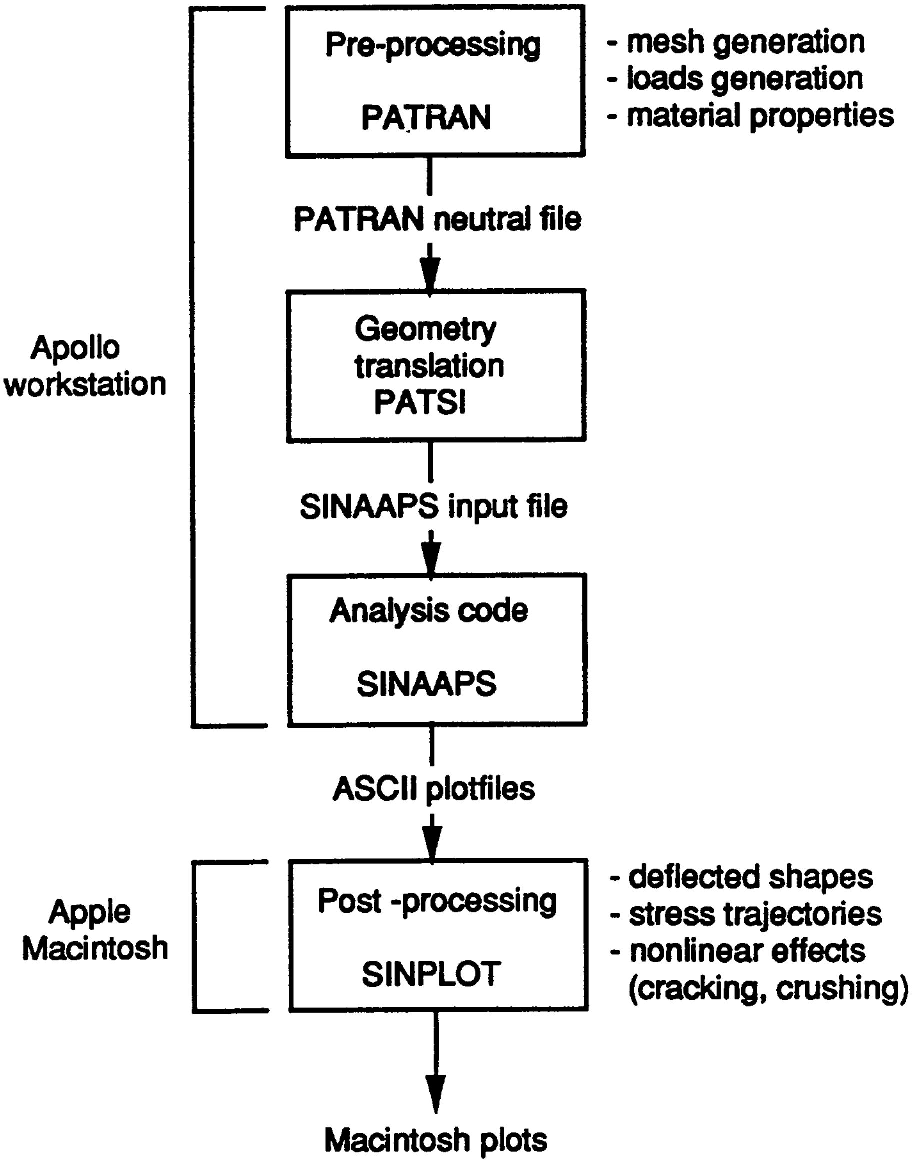

Figure 4.20 Model pre- and post- processing strategy

5.0 FINITE ELEMENT RESULTS

5.1 Introduction

As expected, the finite element analyses of the eight walls generated a significant amount of output results. In order not to be repetitive, and to facilitate insight into the structural behaviour of the walls throughout the loading regime, the results of three walls are presented in detail. These are CF-4, CF-8, and TF-1.

Detailed results are presented in terms of load vs. midspan deflection curves, plots of nonlinear effects such as crack location and orientation and compressive softening locations, and local stress plots. Local stresses are taken here to mean the normal stresses in the principal axes of orthotropy. In certain cases, the stress distribution in the steel plates is also shown. For walls not presented in detail, only the load vs. midspan deflection curves are presented.

5.2 Specimen CF-4

This specimen was the first wall to be analysed. At that point, it was necessary to gain confidence in the model refinement with respect to the performance of the concrete constitutive relationship. The basic issue here was mesh dependency, with other aspects of the model having been tested elsewhere. Since the width of the fracture process zone is the governing factor, and that has been tied to the integration point spacing, it was felt that varying the integration order would represent a change in the effective mesh refinement. This would enable a determination of a suitable degree of mesh refinement necessary for accuracy, and also determine whether the model was objective with respect to mesh refinement.

Figure 5.1 shows the load vs. midspan deflection curve obtained from three analyses of the CF-4 model performed using 2x2, 3x3, and 4x4 Gaussian integration rules. Pre-peak response was nearly identical for the three cases. The peak loads differ somewhat in magnitude; values of 4.02, 5.16, and 5.60 MPa were computed for the 2x2, 3x3, and 4x4 integration rules respectively. This trend of lower strength values for decreasing integration orders is probably due to the decrease in structural redundancy for decreasing order. Figure 5.2 illustrates this effect. Elements with different integration orders are subjected to a stress field which increases from right to left. Softening behaviour is assumed. Once the first Gauss point becomes soft, the excess load (stress) is redistributed to the adjacent Gauss points. For increasing orders of integration, more capacity exists for load redistribution than lower orders. Hence, an increase in capacity with increasing orders is to be expected. However, the wall ultimate load is expected to monotonically converge to a unique value as the number of integration points increases. This trend is seen by the decrease in load difference between 2x2, 3x3, and 4x4 integration rules.

The post peak response of the three integration orders is similar. The constitutive softening relationships developed in Chapter 3 give consistent descending branches for differing mesh spacings. Although not conclusive, the softening relationships show good promise in modelling concrete compressive softening problems.

There is a significant amount of "chatter" in the analytical results, i.e. stress increases and decreases. This is probably due to the finite nature of the model. As various Gauss points soften, a perturbation is set up in the model. The load decreases until suitable load redistribution occurs to warrant load increase. The load will then increase until more regions soften, causing another perturbation. As will be seen in the experimental results presented, a similar effect exists in the test data.

In all subsequent work a 3x3 Gauss rule is used, because the 3x3 rule is exact for quadratic isoparametric elements, and gives sufficiently accurate results in both the pre- and post-peak region for Specimen CF-4.

Figure 5.3 is a plot of equivalent distributed load intensity versus midspan deflection for specimen CF-4 for a Gauss integration rule of 3x3. It can be seen that the numerical curve is somewhat stiffer in the pre-peak region than the test results, but gives an adequate representation of the wall behaviour. The peak load was computed as 5.10 MPa, which compares favorably to the experimentally obtained load of 4.91 MPa. The post-peak response was fairly stable, and compares well with the experimental curve. The residual load was calculated as 2.50 MPa, which is identical to the experimentally obtained residual load.

It is interesting to describe the typical convergence characteristics of the composite walls. Typically, no convergence problems are encountered until first cracking or crushing occurs. At this point, numerous iterates in the order of 100 to 150 are required before the specified convergence tolerances of 0.05 are met. This is due to the high nonlinearity of much of the structure as it loads. After the peak load is reached, localization affects relatively small regions while the rest of the structure unloads. The stiffness properties of the unloaded parts of the structure do not change significantly. Convergence is then stable throughout the post-peak range.

Using the secant modulus of concrete for stiffness calculations, relatively few problems were encountered with convergence. The numerical stability of the solution was quite robust, and convergence was always obtained.

Figures 5.4 and 5.6 through 5.10 are plots of the nonlinear effects in the concrete at midspan displacement levels of 5.0, 8.0, 10.0, 12.0, 20.0, and 40.0 mm respectively for specimen CF-4. The nonlinear effects are plotted at the Gauss points. Cracks caused by the in-plane stresses, σ_x, σ_y, and τ_{xy}, are identified by a solid line; cracks caused by the out of plane stress, σ_z, are denoted by a diamond shape, and compressive softening points are identified by an octagonal shape. At 5.0 mm, extensive diagonal cracking has formed in the wall cells closest to the support. Cracking had also formed in the midspan cell. This cracking pattern is consistent with the observed experimental result in Figure 5.5. At 8.0 mm, softening has initiated in the element nearest the support plate, and the far diagonal corner of that cell. At 10.0 mm, which was the deflection at which the ultimate load was reached, softening had propagated through these two elements and into others. As deformation levels increased, the damage level increased in the main shear cell, which was evidenced by an increase in cracking. However, the softening regions maintain a nearly constant size after a deflection of 12.0 mm. This means that strain localization was occuring in this region. At the termination of the analysis (Figure 5.10), extensive damage was evident in the shear cell, and especially near the support region. The test experienced similar damage, which is shown in Figure 5.11.

It was experimentally observed that major concrete spalling occurred in the support region when the ultimate load was reached, an indication of major crushing accompanied by cracks caused by out of plane stresses. In the test, the damage in the cell increased as deformation levels were increased in the post-peak region, a trend also observed in the analysis. Thus, the analysis prediction of failure was identical to experimentally obtained results.

Evidence of strain localization near the diagonal corners can be observed by examination of Figures 5.12 to 5.17, which are deformed shapes at deformation levels of 5.0, 8.0, 10.0, 12.0, 20.0, and 40.0 mm. The deflections are magnified by 10 for deformation levels of 5.0, 8.0, 10.0, and 12.0 mm, and 1 for midspan deflections of 20.0 and 40.0 mm. It can be seen that localized deformation takes place in the support region and at the upper diagonal corner, thus indicating strain localization. The deformed shape at a deflection of 40.0 mm is similar to that obtained by experiment (see Figure 5.11).

It is seen in Figures 5.12 to 5.15 that separation occurs in the lower right hand corner of the wall cell nearest the support, and that there is major slippage occurring between the horizontal plates and the concrete core. The separation was also observed in the test. Such large relative movements between the steel and concrete means that it is impossible to predict the load-deformation behaviour of the composite walls using conventional reinforced concrete elements.

Figures 5.18 to 5.23 show local stress trajectories in the concrete for midspan deflections of 5.0, 8.0, 10.0, 12.0, 20.0, and 40.0 mm. The classical strut model is clearly seen in Figure 5.18a. Figure 5.18b shows the development of compressive struts in the model. In the central cell (denoted by Cell 1 in Figure 5.18b), a horizontal strut spans across to the top of the first diaphragm plate. A minor strut spans down to the bottom of the first diaphragm plate. The load from the central cell is then transferred by diaphragm plate action to the cell nearest the support (denoted by Cell 2). This strut then spans to the support. As well, the load on the overhanging cell (identified as Cell 3) also struts into the support. Thus, the analytical behaviour supports the concept of a strut and tie model to predict failure loads in the walls.

Examination of Figures 5.19 through 5.23 gives an insight into the redistribution of load occurring in the structure after peak load. It can be seen that the stress levels decrease significantly in the support region after peak load; the stresses attempt to "flow around" the softening region and enter the support by means of the diaphragm and bottom plates. Such load redistribution is the reason that a residual load is recorded in the tests. The promotion of this redistribution is the key to providing ductility in a shear compression failure mode.

It is observed in Figure 5.17 that transfer of forces in the support region imposes severe flexural deformation of the plate. It would thus appear that a successful design should account for plate bending stiffness. Indeed, it was observed in subsequent tests at C-FER that plate failures due to tearing occurred in specimens with very thin plates.

In Figures 5.18 through 5.23, and in all subsequent local stress plots, the steel plate stresses are not plotted. These stresses were neglected because the stress magnitudes were large in comparison with the concrete stresses. This resulted in confusion when both stress quantities were plotted simultaneously. Plate stresses are discussed in detail in Section 5.5.

5.3 Specimen CF-8

Figure 5.24 is a plot of load versus midspan deflection for specimen CF-8. Again, the pre-peak response is somewhat stiffer than the test, perhaps indicating the need to use a lower friction angle. Two analyses were performed for this wall. The initial analysis that was performed assumed that the steel was experiencing plane strain conditions. It was found that this resulted in premature failure of the wall when compared with experimental data as can be seen in Figure 5.24 indicated with empty squares. The second analysis, denoted by black diamonds, assumed that the steel was experiencing plane stress conditions. Since it was not possible to perform an analysis where the steel was plane stress and the concrete was plane strain, a plane strain analysis was conducted with the plate yield stress reduced to approximate plane stress conditions. This called for a yield stress reduction of 11.1%. When this was done, it was found that the bottom steel plate had yielded significantly, as evidenced by the extended yield plateau in Figure 5.24, and in addition, a better estimate of the ultimate load was obtained. The large variation in load-deformation behaviour for the change in yield strength shows that the steel plate is not restrained entirely against lateral expansion. However, it was found that the residual load was not significantly affected by a yield strength change. The ultimate computed equivalent distributed load obtained from the second analysis was 6.85 MPa, which compared favorably to a reported experimental load of 6.66 MPa. The test was terminated before a stable residual load could be determined, so there is no comparison of post-peak response. In the following, only the results of the second analysis are presented.

Figures 5.25 and 5.27 through 5.31 show nonlinear effects in the concrete for midspan deflections of 5.0, 8.0, 10.0, 20.0, 25.0, and 40.0 mm respectively. At 5.0 mm, diagonal cracking can be identified in all shear cells. As well, major cracking occurred at midspan. This cracking pattern is identical to that observed in Figure 5.26, which is a photograph of the cracked specimen. As the midspan deflection increases, softening initiates at the diagonal corners in the shear cell nearest the support. Softening gradually propagates through the cell and extensive cracking in the plane of the specimen is observed, denoted by diamond shapes. At the analysis termination, extensive damage exists in the shear cell at the support, which is corroborated by the photograph of the failed specimen in Figure 5.32.

Progression of strain localization at the top diagonal corner of the first shear cell can be seen by examination of Figures 5.33 through 5.38, which are deformation plots at midspan deflections of 5.0, 8.0, 10.0, 20.0, 25.0, and 40.0 mm. Localized deformation is present in this location as the midspan deflection is increased. It is also noted that large separations occur at the bottom right hand corner of this cell, and in the middle cell at the bottom plate. Unfortunately, close up photographs of this region for specimen CF-8 were not available to verify this observation. The deformed shape at the analysis termination is similar to the photograph shown in Figure 5.32.

Evidence of strut and tie action is seen in Figure 5.39, which is a plot of the stress trajectories at a midspan deflection of 5.0 mm. Struts along the diagonals of the cells are evident, again supporting the rationale for using a strut and tie model to compute ultimate loads. Figures 5.40 through 5.43 are stress trajectory plots for midspan deflections of 8.0, 10.0, 12.0, 20.0, 30.0, and 40.0 mm., and illustrate the load redistribution that occurs in the softening range. Once the top diagonal corner in the first shear cell becomes soft, it is observed that the main compressive strut changes direction, and attempts to span across the first shear diaphragm, as evidenced in Figure 5.42. In addition, some load is carried into the support by the formation of a secondary strut as the stresses attempt to "flow around" the soft area.

5.4 Specimen TF-1

Figure 5.44 is the load versus midspan deflection plot for specimen TF-1. It should be remembered that specimen TF-1 was tested under a constant longitudinal compression force of 1965 kN. It is observed that the pre-peak response is close to the experimentally obtained results. The computed ultimate load is 5600 kN, which is identical to the test ultimate load. The calculated post-peak response is much lower than the experimental curve, which perhaps suggests that triaxial confinement has a significant effect upon concrete post-peak behaviour (Pramono and Willam, 1989).

Figures 5.45 to 5.49 show the progression of damage through the structure at application of in-plane load and midspan deflections of 5.0, 8.0, 10.0, 15.0, and 40.0 mm respectively. It is seen that the failure mode is similar to the two walls previously described, with crushing occurring at the top and bottom diagonal corners of the shear cell closest to the support, followed by extensive damage in this cell. This failure mode also compares favorably with the failed specimen shown in Figure 5.50.

Figures 5.51 and 5.52 show the deformed shapes at midspan deflection levels of 8.0 mm (magnified 10 times) and 40.0 mm (not magnified). It is again seen that strain localization occurs at the top and bottom diagonal corners. The displaced shape at 40.0 mm (Figure 5.52) differs slightly from the failed specimen in Figure 5.50. There is pronounced curvature of the top plate at the test termination. This may have been impossible for the model to capture, since a greater degree of mesh refinement and a large deformation formulation may be necessary.

Figures 5.53 and 5.54 are stress trajectory plots at midspan deflection levels of 8.0 mm and 40.0 mm respectively. The strut and tie action is again evident in Figure 5.53. After the peak load is reached, the load attempts to strut into the support around the soft diagonal corners, similar to the other two walls mentioned earlier.

5.5 Plate Stresses

In order to further check the performance of the finite element model, the stress levels in the steel plates must be examined. Two examples are included here; specimens CF-4 and CF-8. Since the local stress trajectory plots for CF-4 and CF-8 favour the concept of a strut and tie load carrying mechanism, the plate stresses are checked against the results of a simple strut and tie model.

Figures 5.55 and 5.56 show the strut and tie models adopted for specimens CF-4 and CF-8 respectively. It is assumed that the top and bottom steel plates carry full compressive and tensile loads. In other words, no longitudinal concrete struts form. The concrete compression struts are assumed to form between the angles of 15° and 75°, which is consistent with the provisions set out in the general method for shear in CSA CAN3-A23.3-M89 (CSA, 1989).

Figure 5.57 shows the computed top and bottom plate stress levels for specimen CF-4 at a midspan deflection level of 10.0 mm. The corresponding load level, P, was 582.9 kN. It can be seen that the stresses obtained from the finite element model are close to the stresses computed from the strut and tie model for the bottom plate. The post-peak stress distribution is also plotted in Figure 5.57 at a midspan deflection level of 40.0 mm (load level of 297.2 kN). It is observed that the ratio between top plate stress levels at and after peak load is approximately 2.0, which is in agreement with the ratio of peak to residual load.

Significant stress level differences occur between the finite element and truss models in the top plate. The compressive loads in both the central and support regions are lower than predicted by the truss model. Examination of the local stress trajectories in Figure 5.20 indicates that a compressive block forms in the central region of the plate. This means that the concrete assists in carrying the compressive load, thereby decreasing the stress intensity in the top plate. It is also seen from Figure 5.57 that the tensile load in the top plate near the support is lower than that predicted by the truss model. Examination of the assumed strut and tie model in Figure 5.56 indicates that the stress in that area can be computed by using the compressive strut on the overhanging edge of the specimen. It can be seen in Figure 5.20 that the compressive strut does not span from the load point to the support center; instead, the strut spans from the load point to the edge of the support plate. This has the effect of lowering the stress intensity in the top plate.

Figure 5.58 shows the stress distribution in the diaphragm plate referred to as diaphragm plate 1 in Figure 5.55. The finite element model predicts stresses which are lower than those calculated using the strut and tie model. This could be due to partial strut action from the load point to the support center; the net effect of this is to reduce the load level in the diaphragm plate. Examination of the local stress trajectories in Figure 5.20 confirms this.

Figure 5.59 is a plot of the stress distributions in the top and bottom plates of specimen CF-8 at a midspan deflection of 20.0 mm. The corresponding load level, P, is 793.6 kN. It is again seen that the finite element model produces results which are consistent with the strut and tie analogy for the bottom plate. As for specimen CF-4, there are significant differences in predicted stress levels for the top plate. Examination of local stress trajectories in Figure 5.41 indicates that a compressive stress block exists in the central region similar to that found in specimen CF-4 which has the tendency to reduce the stress intensity in the top plate. The compressive strut on the overhanging edge of the wall spans from the load point to the support plate edge, which reduces the stress intensity in the top plate near the support, similar to specimen CF-4.

Figure 5.60 shows the stress distribution in the plates designated as diaphragm plates 1 and 2 in Figure 5.56. The stress level for diaphragm plate 1 is close to the truss model stress level; however, the computed stress level in diaphragm plate 2 is significantly lower than the truss model prediction. It is evident from examination of Figure 5.41 that partial strut action occurs from the load point in the central region to the bottom of diaphragm plate 1. This has the effect of reducing the load intensity in diaphragm plate 2.

To summarize, the finite element model produces plate stress results which are consistent with the formation of a strut and tie load carrying mechanism. Subtle differences are seen in top plate stresses; these are due to neglecting the effects of partial strut action in the strut and tie model.

5.6 Results Summary

Figures 5.61 to 5.65 are load versus midspan deflection for specimens CF-5, CF-13, TF-2, TF-4, and VTT3 respectively. Good correlation is observed between analytical results and experiment for all tests, with the exception of the prediction of the ultimate load for specimen TF-4, and the residual load level for specimen VTT3. The structural behaviour of specimens CF-5, CF-13, and TF-2 was similar to that seen in specimens CF-4, CF-8, and TF-1. Post-peak response was precipitated by localized crushing at the diagonal corners of the cell adjacent to the support.

The predicted ultimate load for specimen TF-4 was calculated as 7800 kN, which is significantly above the reported failure load of 5876 kN. This specimen had the highest reported concrete strength (68.0 MPa) and the largest in-plane force (3000 kN, or 15.0 MPa confining stress). This high confining stress would result in high equivalent uniaxial strengths if the Willam and Warnke surface is used. The values of high compression strength were taken for normal concretes (Elwi and Murray, 1979). It is possible that these values may have to be adjusted for high strength concretes. Uncertainty in boundary conditions, in particular the roller configuration and tie-down fixity, may also have an influence on the prediction accuracy.

The predicted residual load for specimen VTT3 was computed as 800 kN, which is below the reported residual load of 1200 kN. In addition, the analytical results show a sudden decrease in load after failure, followed by a gradual load increase thereafter, which was not observed in the test (see Figure 5.65). Closer examination of the finite element model revealed that the model did not include a support plate near the reaction point. Inclusion of this plate may have had the effect of widening the strut in the support area; hence, the load redistribution capability of the structure may have been increased.

The results for the eight walls are summarized in Table 5.1. Ultimate and residual loads are compared with experimental results. It can be seen that a good overall correlation exists between analysis and experiment for both ultimate and residual loads, with test to predicted ratios of 0.93 and 1.09 respectively. The predictions for the CF series are excellent, with test to predicted ratios of 0.96 and 1.01. The TF series shows more scatter and less accurate predictions; test to predicted ratios are 0.87 and 1.37. As mentioned above, uncertainty in boundary conditions for this test series and concrete strengths at high confining pressures may account for the differences.

To summarize, the finite element model provides results which are consistent with physically observed behaviour, both in the pre-peak and post-peak domains:

1) Pre-peak - The load vs. midspan deflection curves are similar to those obtained from test results. Cracking patterns are nearly identical to those observed experimentally. Test to predicted ratios for ultimate loads are good, and the failure mode is correctly predicted. Computed plate stresses are consistent with the concept of a strut and tie model, which is generally accepted as the correct load carrying mechanism.

2) Post-peak - Residual load predictions are good, and the damage level in the cell adjacent to the support is consistent with experimental observation. Examination of the stress trajectories provides insight into the load redistribution occurring after ultimate load.

The ability of the model to follow changes in the load carrying mechanisms is excellent. In addition, by using the secant based model for concrete, high numerical stability was achieved. No significant convergence problems were encountered. The proposed compressive softening constitutive relationship gave results which were objective with respect to mesh refinement. The gap elements used presented no problems for solution convergence, and realistically simulated separation and sliding regions in the wall specimens.

Examination of the concrete stress trajectory plots for the eight walls indicates that a strut and tie model is adequate in computing failure loads of the composite walls. It remains to compute adequate effectiveness factors for the concrete, taking into consideration confinement conditions and concrete strengths. A parametric study using finite element models may be useful in defining strut trajectories and effectiveness factors for a variety of wall configurations.

Specimen	Ultimate Load		Test/ Predicted	Residual Load		Test/ Predicted
	FEA	Test		FEA	Test	
CF-4	5.16	4.91	0.95	2.60	2.50	0.96
CF-5	4.02	3.82	0.95	2.45	2.25	0.92
CF-8	6.82	6.66	0.98	3.80	-	-
CF-13	7.85	7.59	0.97	3.70	4.20	1.14
TF-1	5600	5600	1.00	2500	4500	1.80
TF-2	5300	4550	0.86	2750	3200	1.16
TF-4	7850	5876	0.75	2800	3200	1.14
VTT-3	1920	1860	0.97	800	1250	1.56
		Average:	0.93		Average:	1.09

Note: Ultimate and residual loads are in MPa for the CF series, and in kN for both the TF and VTT series.

<u>Average test/predicted ratio for the CF series</u>

Ultimate Load: 0.96
Residual load: 1.01

<u>Average test/predicted ratio for the TF series</u>

Ultimate Load: 0.87
Residual Load: 1.37

Table 5.1 Summary of results

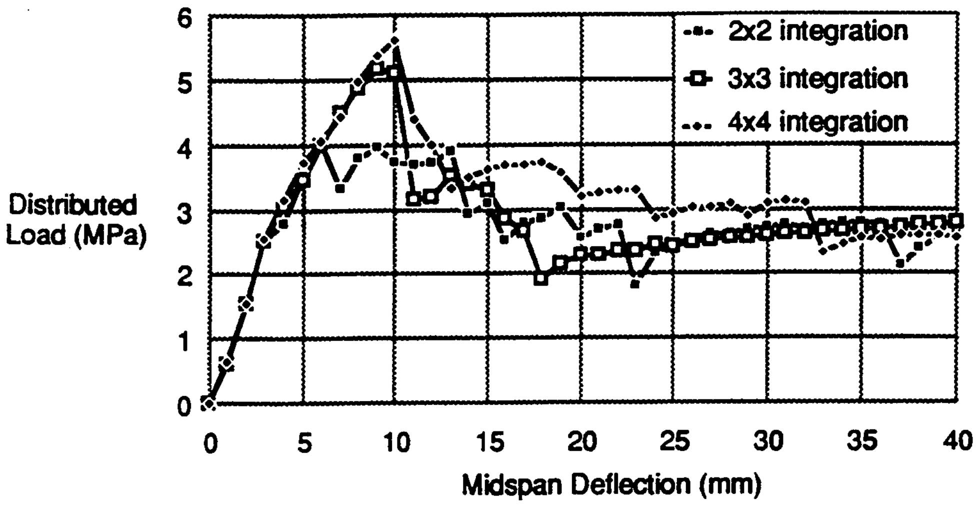

Figure 5.1 Effect of integration order on results

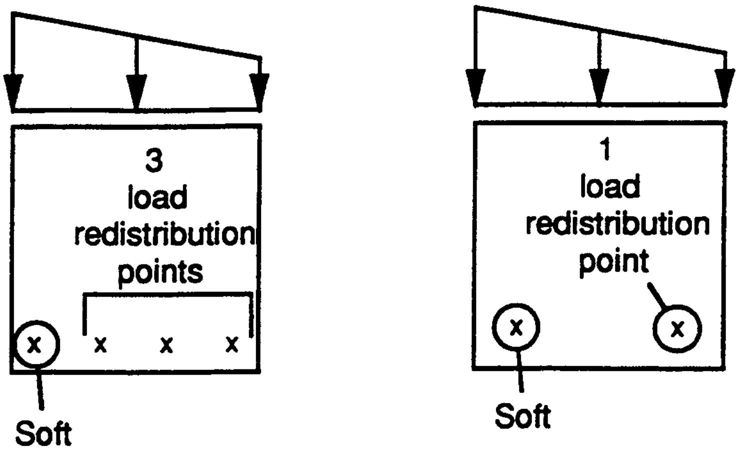

Figure 5.2 Structural redundancy illustration

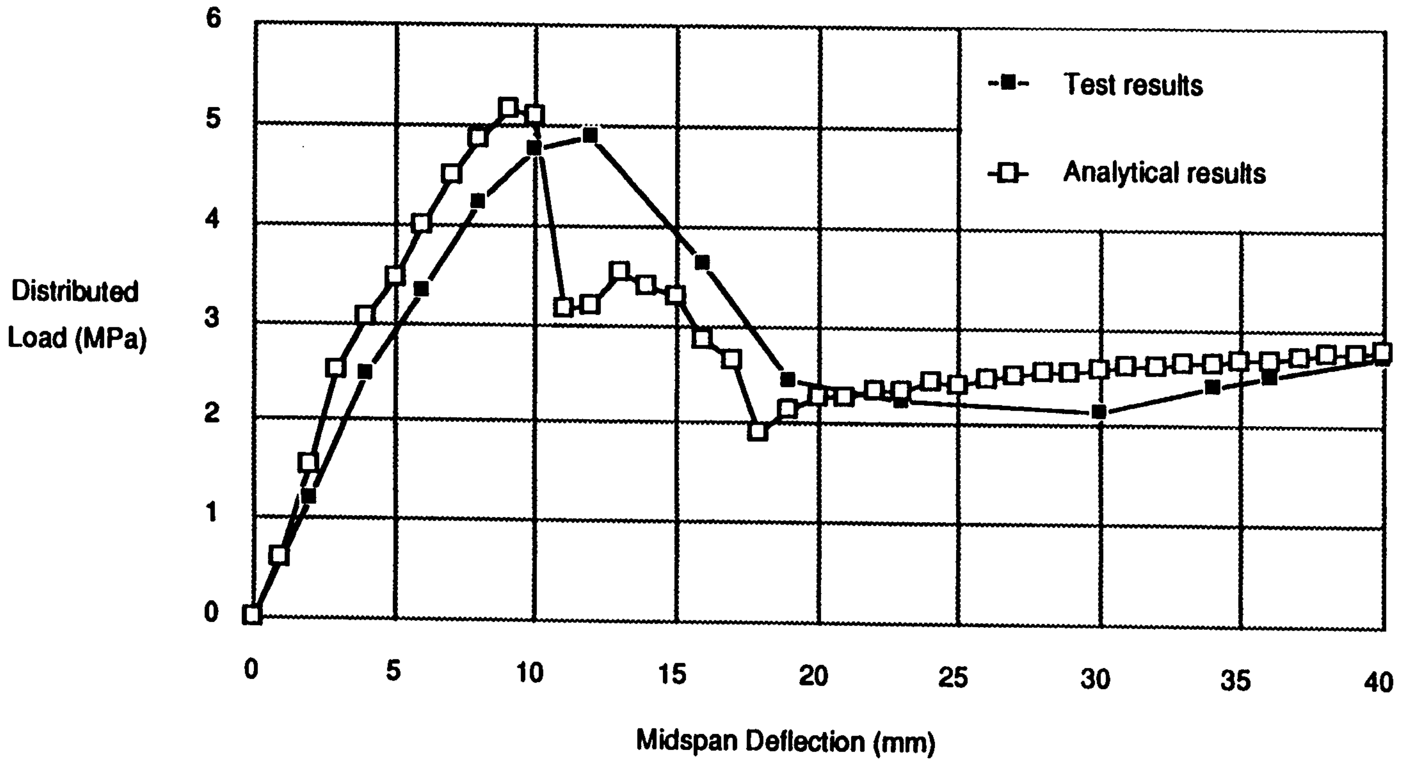

Figure 5.3 CF-4 load vs. midspan deflection plot

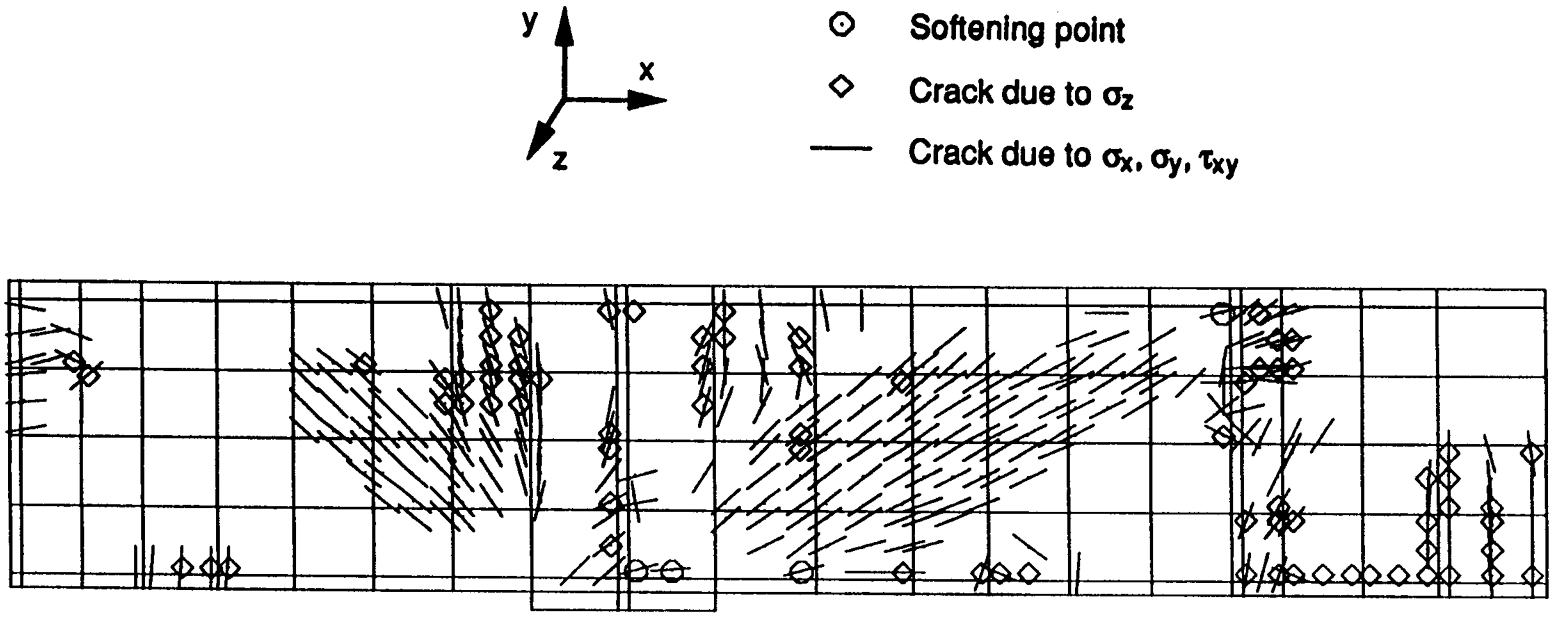

Figure 5.4 CF-4 nonlinear effects for d = 5.0 mm

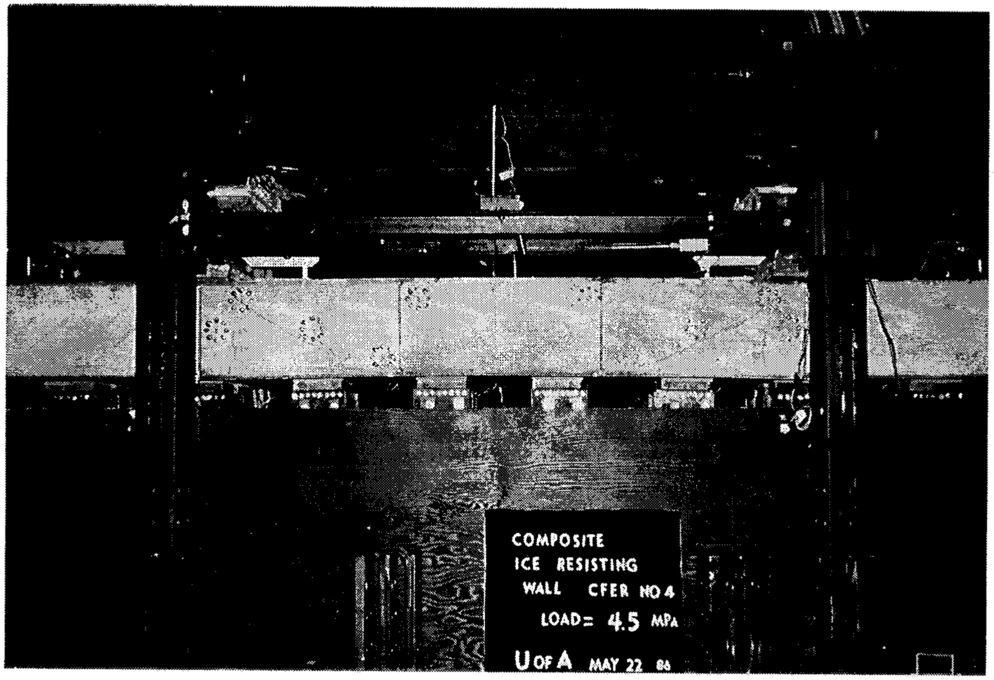

Figure 5.5 Cracking pattern for Specimen CF-4

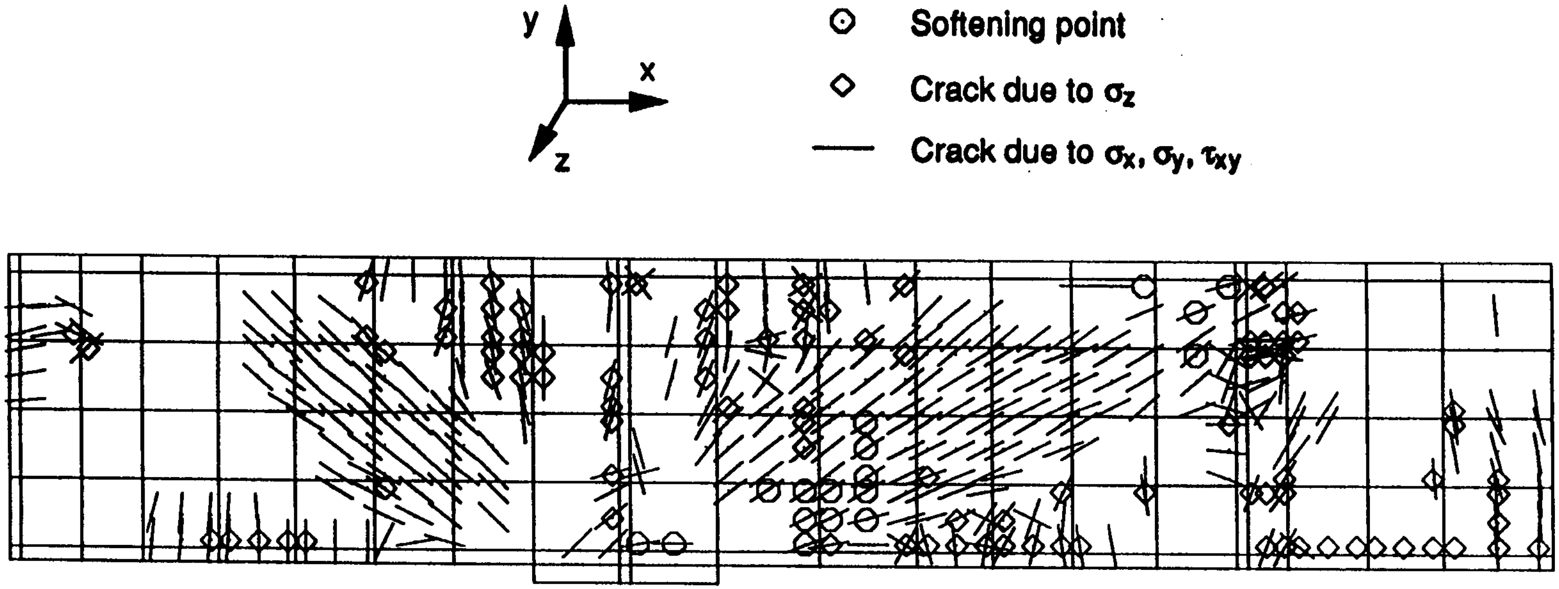

Figure 5.6 CF-4 nonlinear effects for d = 8.0 mm

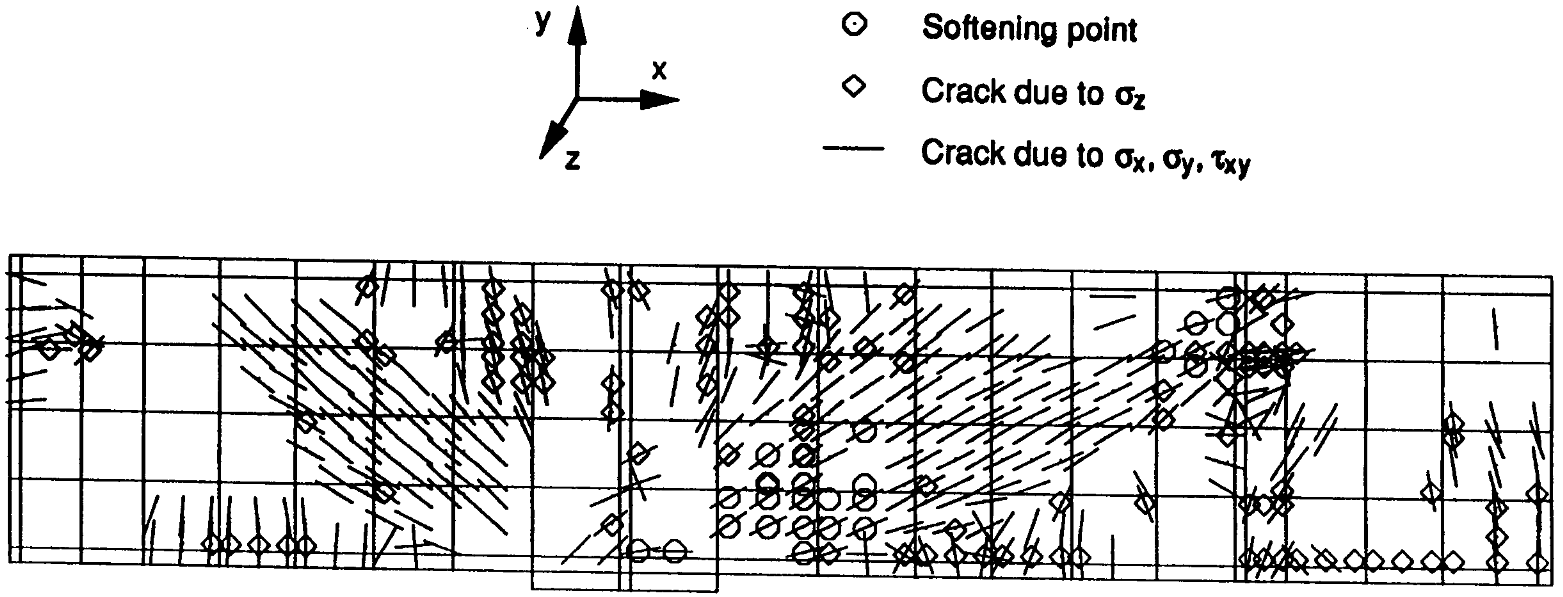

Figure 5.7 CF-4 nonlinear effects for d = 10.0 mm

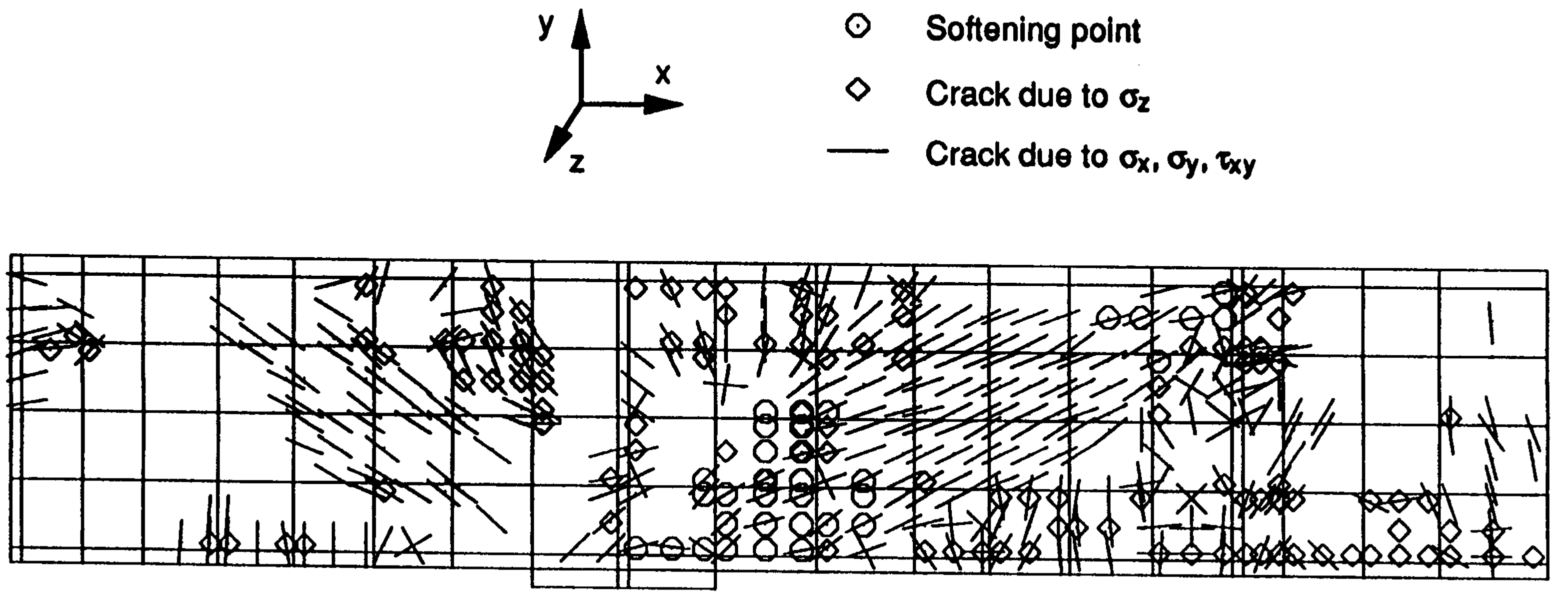

Figure 5.8 CF-4 nonlinear effects for d = 12.0 mm

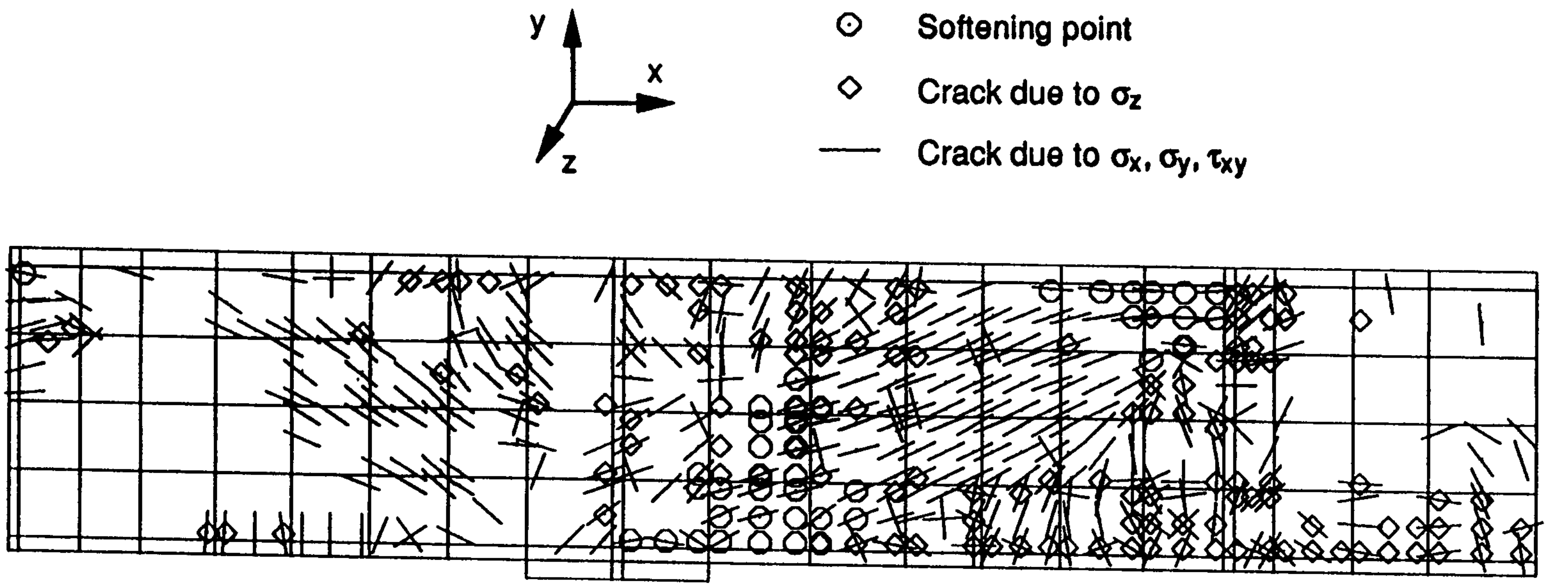

Figure 5.9 CF-4 nonlinear effects for d = 20 mm

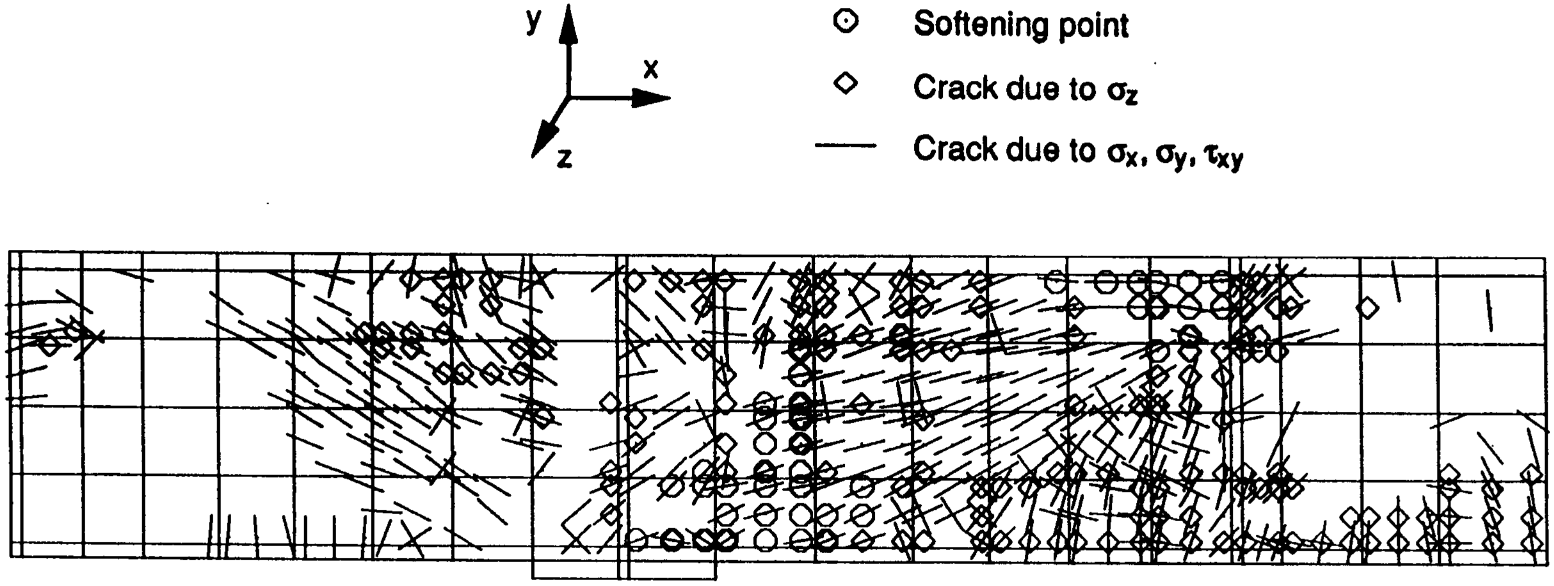

Figure 5.10 CF-4 nonlinear effects for d = 40 mm

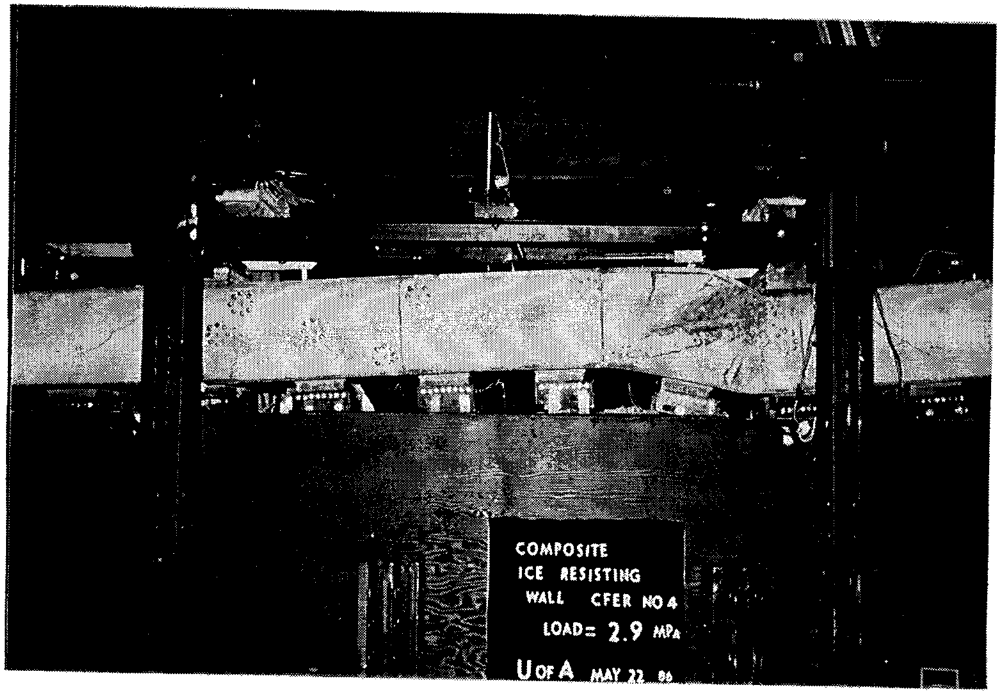

Figure 5.11 Photograph of failed specimen

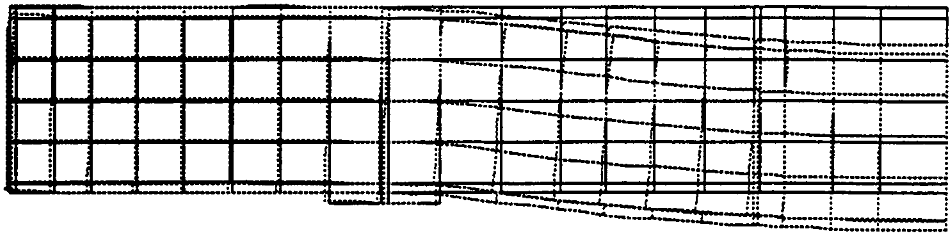

Figure 5.12 CF-4 deformed shape at d = 5.0 mm

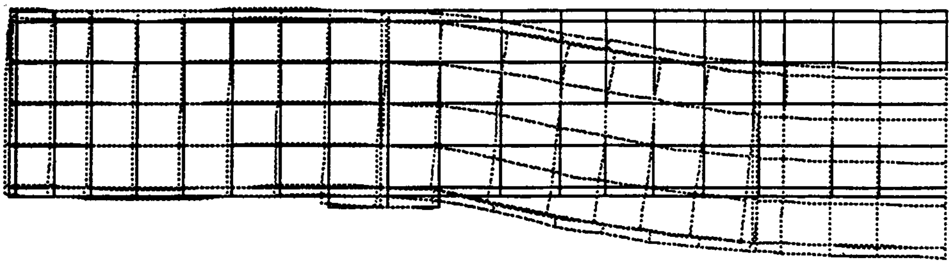

Figure 5.13 CF-4 deformed shape at d = 8.0 mm

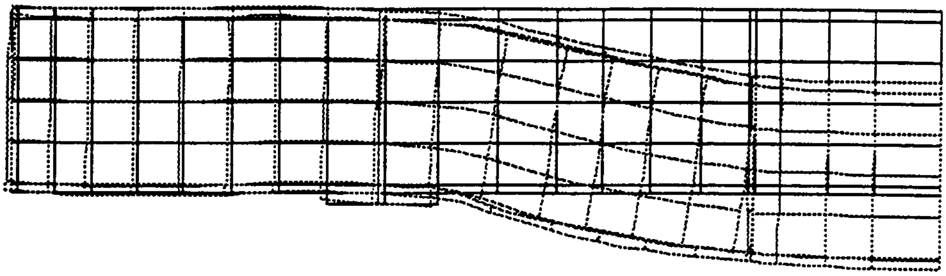

Displacement magnifier = 10

Figure 5.14 CF-4 deformed shape at d = 10.0 mm

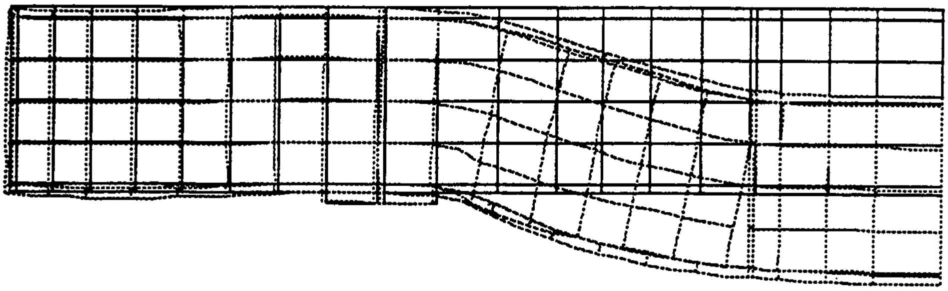

Displacement magnifier = 10

Figure 5.15 CF-4 deformed shape at d = 12.0 mm

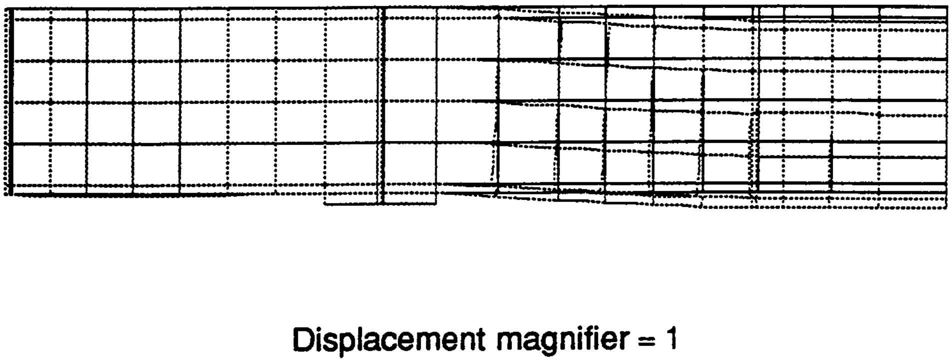

Figure 5.16 CF-4 deformed shape at d = 20.0 mm

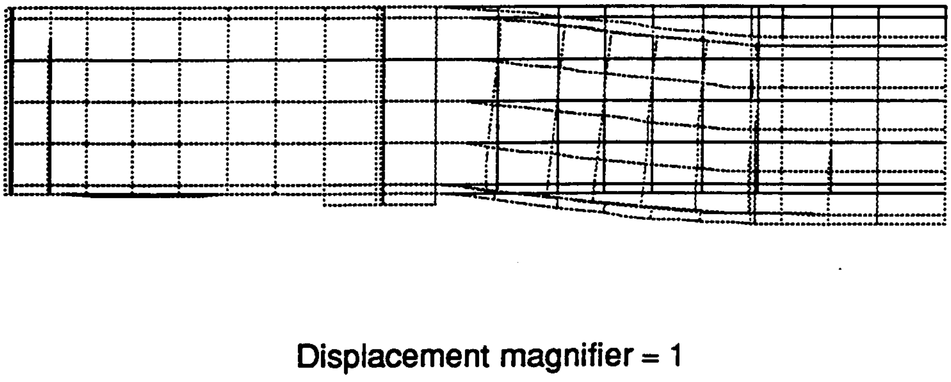

Figure 5.17 CF-4 deformed shape at d = 40.0 mm

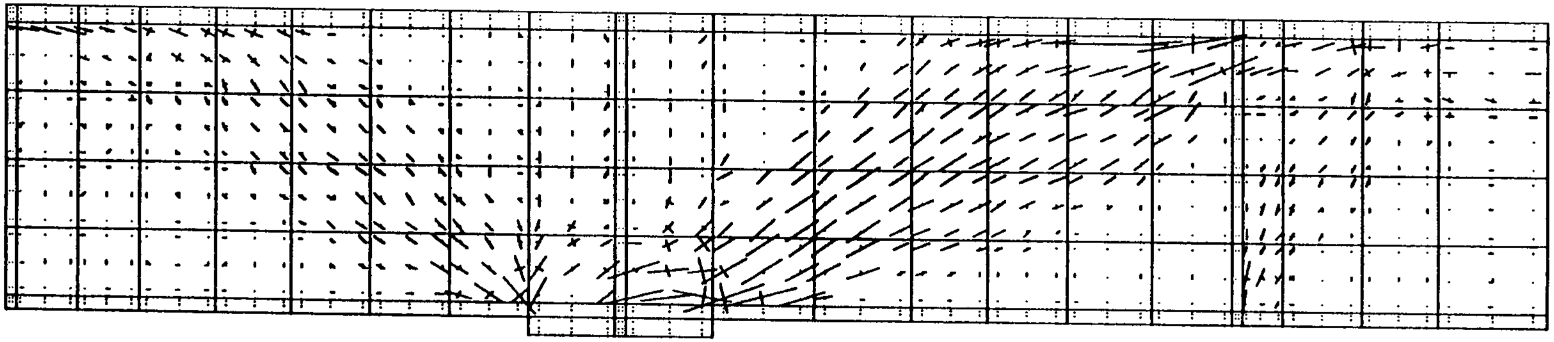

Stress plot scale = 175 MPa/cm

Figure 5.18a CF-4 local stresses at d = 5.0 mm

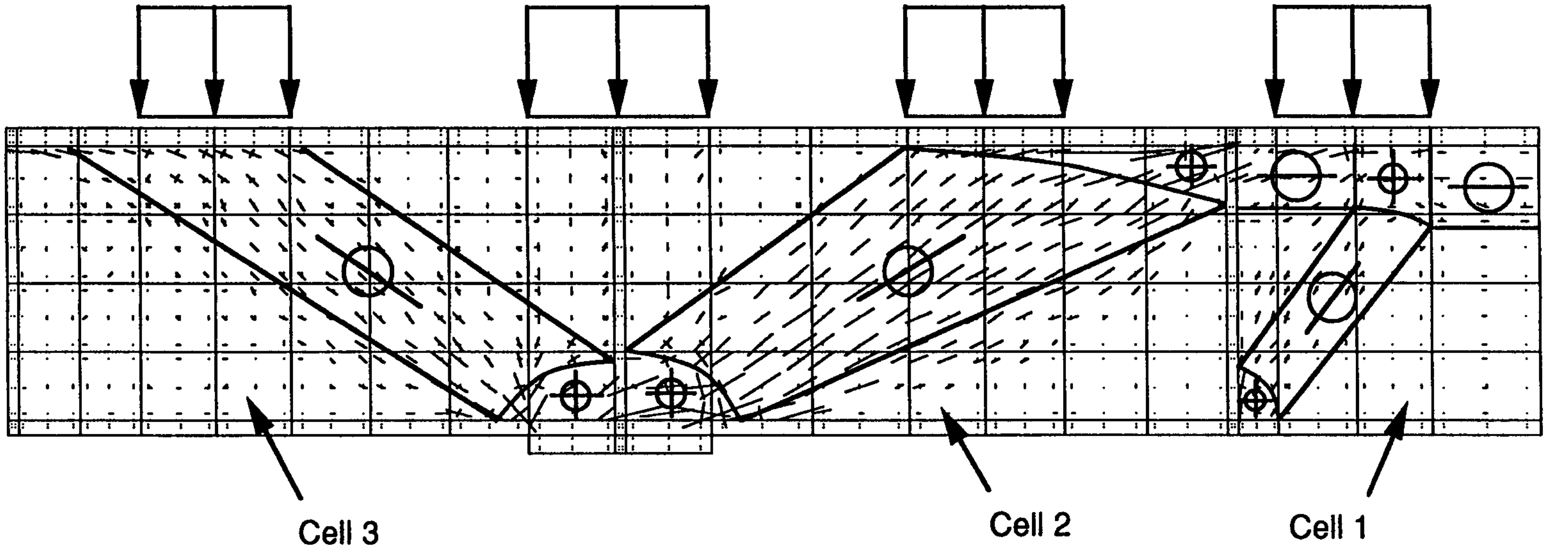

Figure 5.18b Strut and tie analogy for CF-4 at d = 5.0 mm

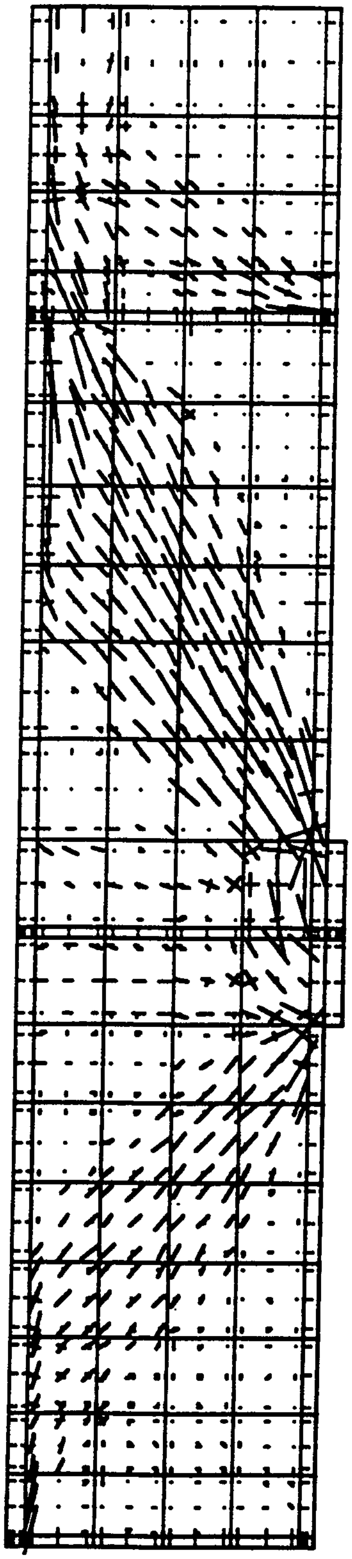

Figure 5.19 CF-4 local stresses at d = 8.0 mm

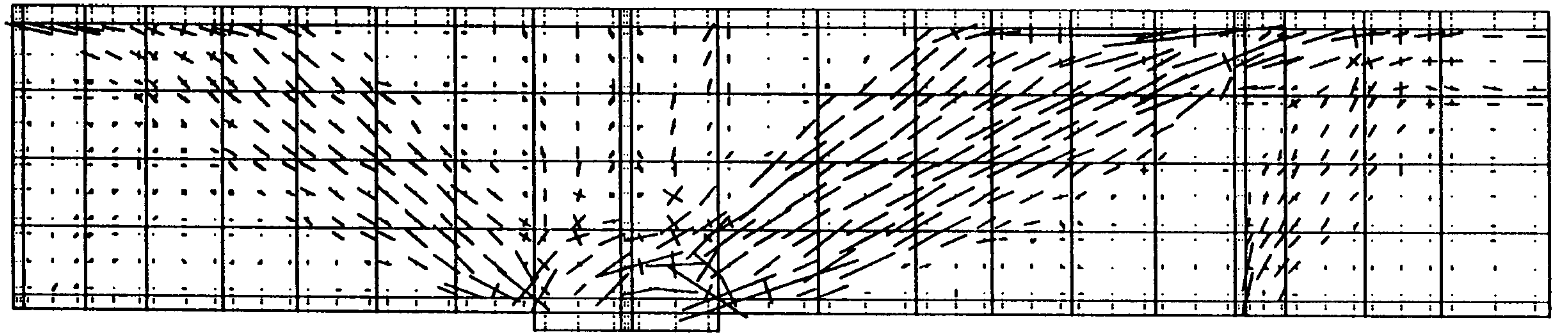

Stress plot scale = 175 MPa/cm

Figure 5.20 CF-4 local stresses at d = 10.0 mm

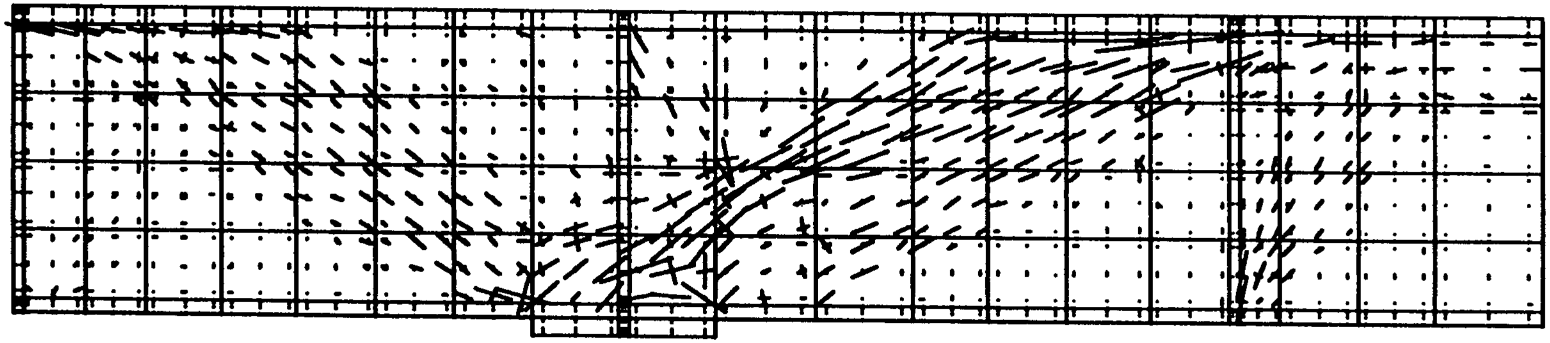

Stress plot scale = 175 MPa/cm

Figure 5.21 CF-4 local stresses at d = 12.0 mm

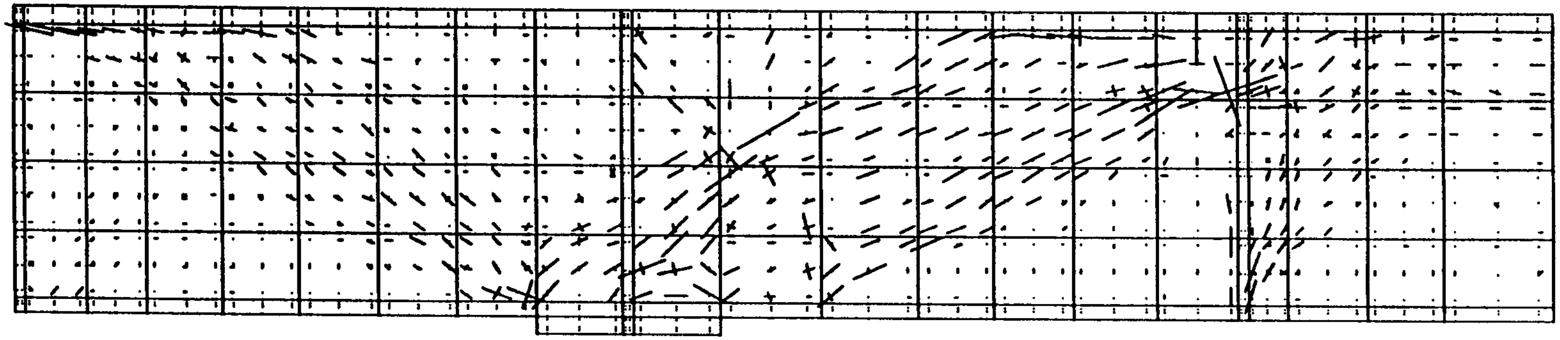

Stress plot scale = 175 MPa/cm

Figure 5.22 CF-4 local stresses for d = 20 mm

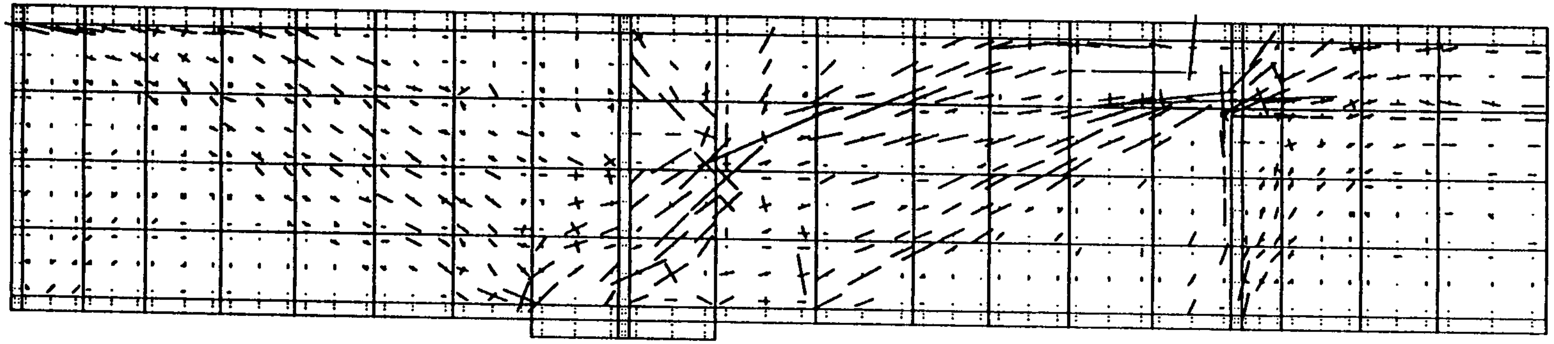

Stress plot scale = 175 MPa/cm

Figure 5.23 CF-4 local stresses for d = 40.0 mm

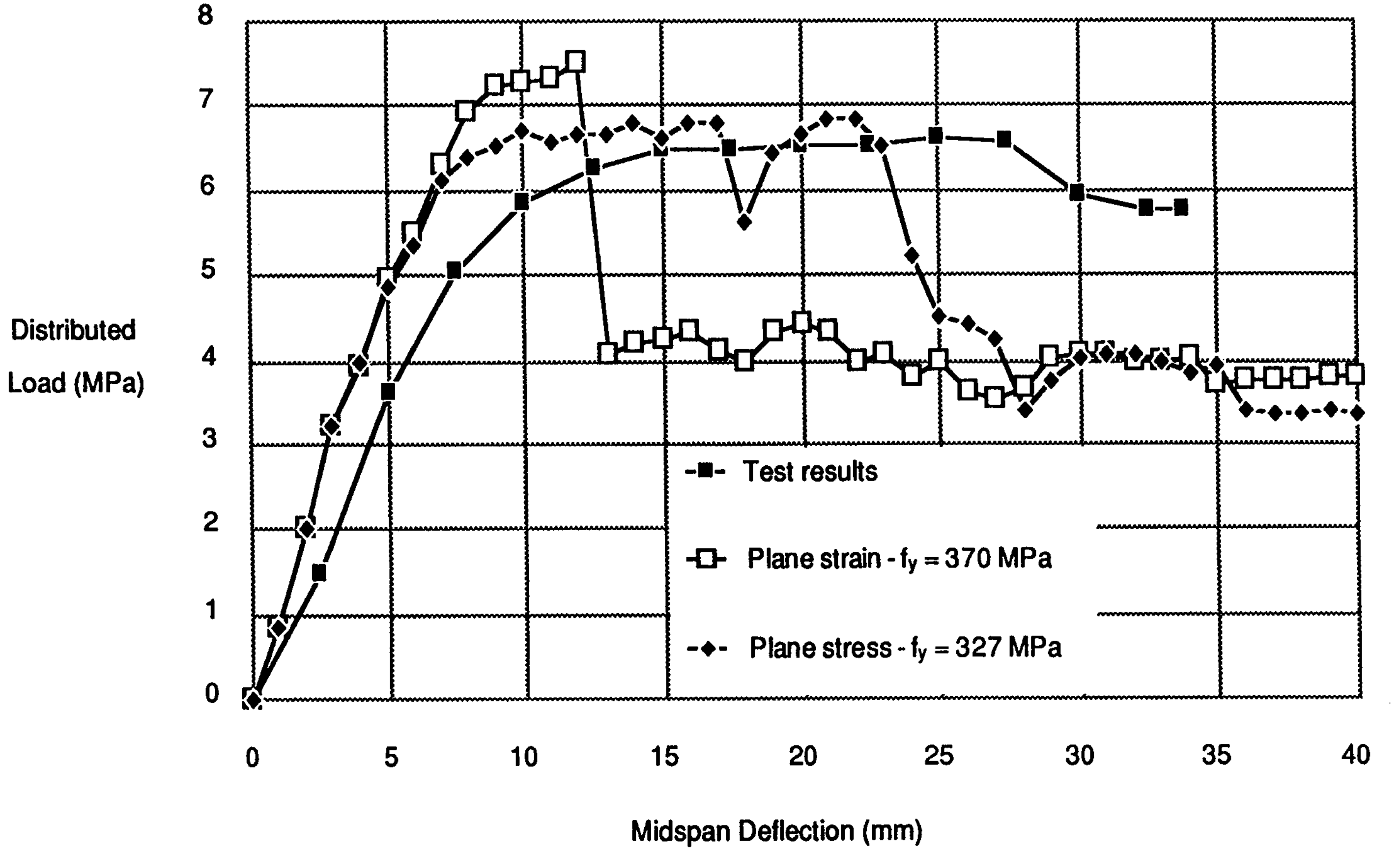

Figure 5.24 CF-8 load vs. midspan deflection plot

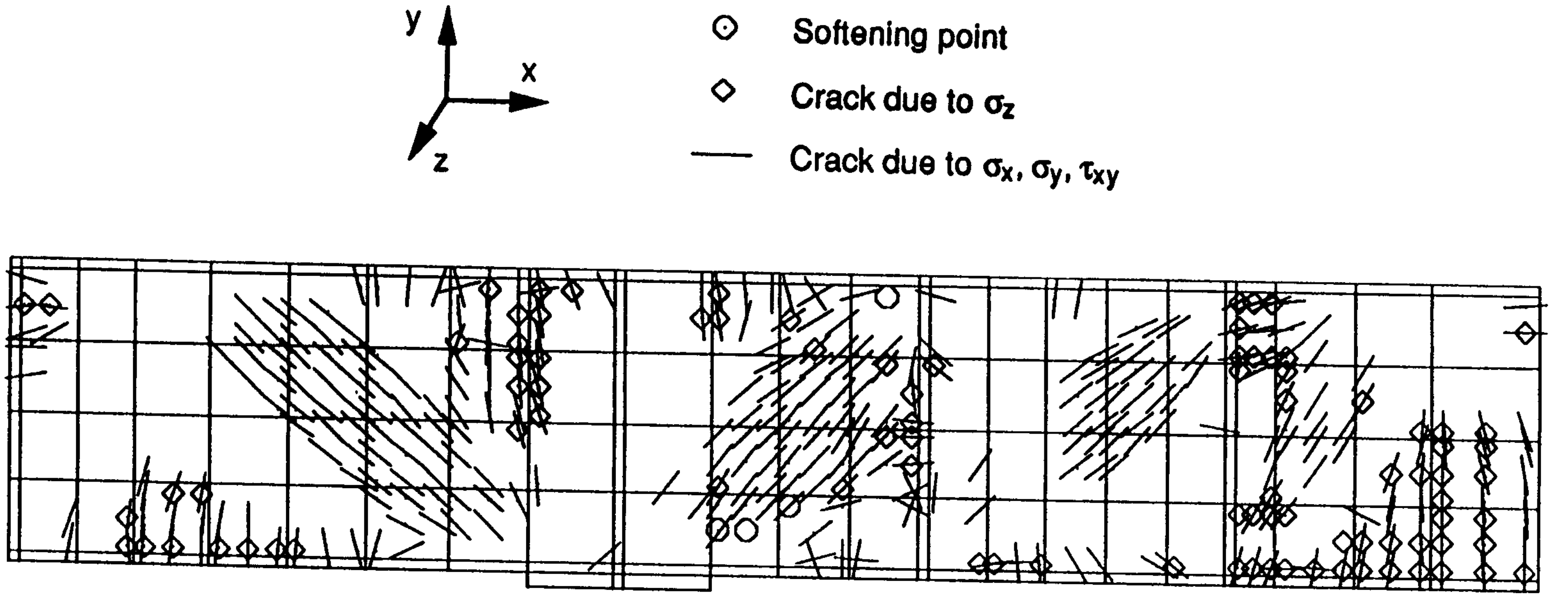

Figure 5.25 CF-8 nonlinear effects for d = 5.0 mm

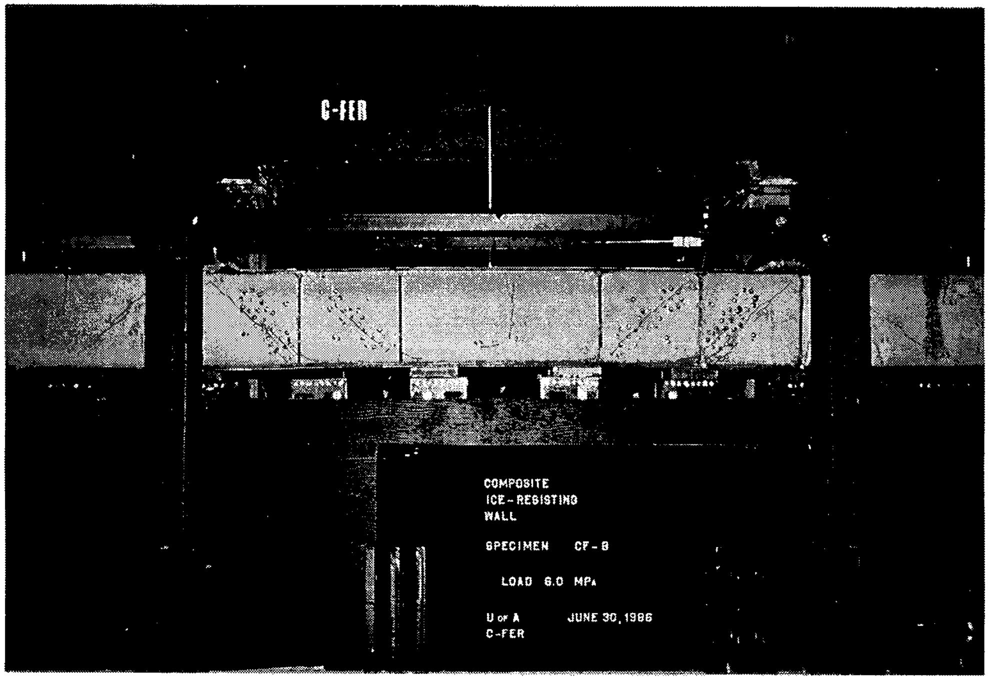

Figure 5.26 Cracking pattern for Specimen CF-8

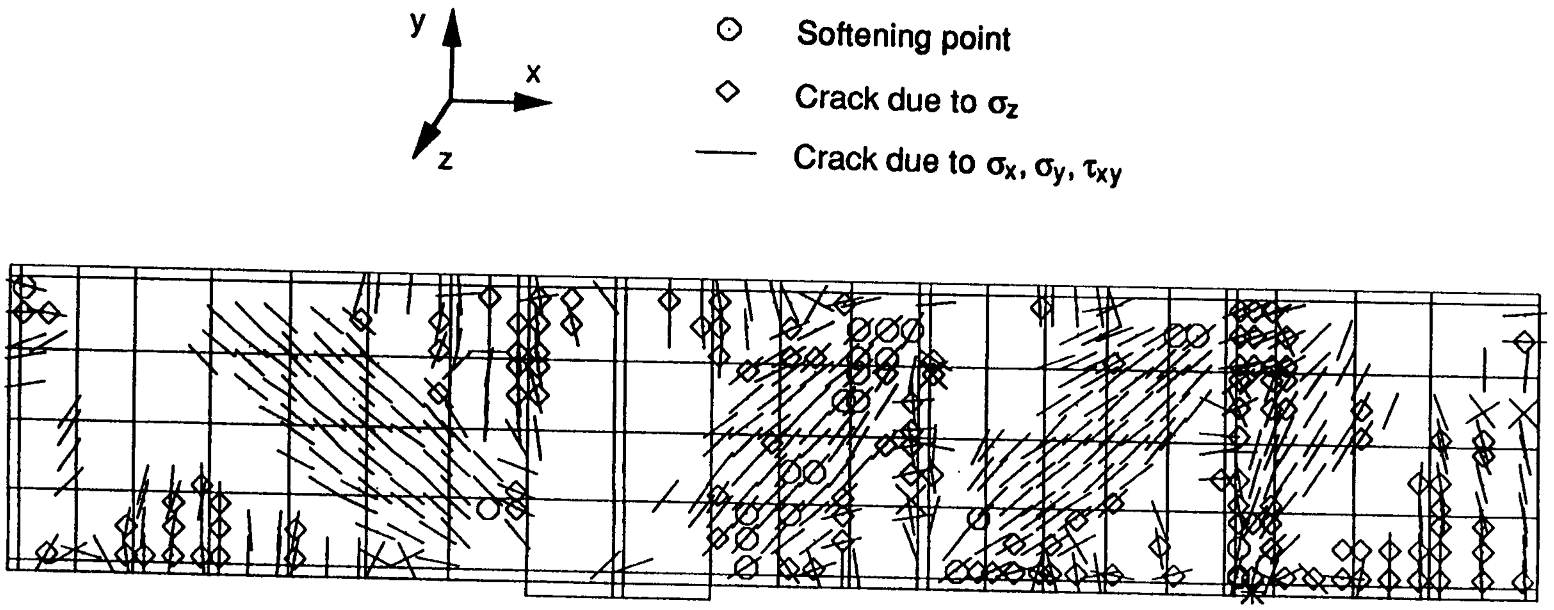

Figure 5.27 CF-8 nonlinear effects for d = 8.0 mm

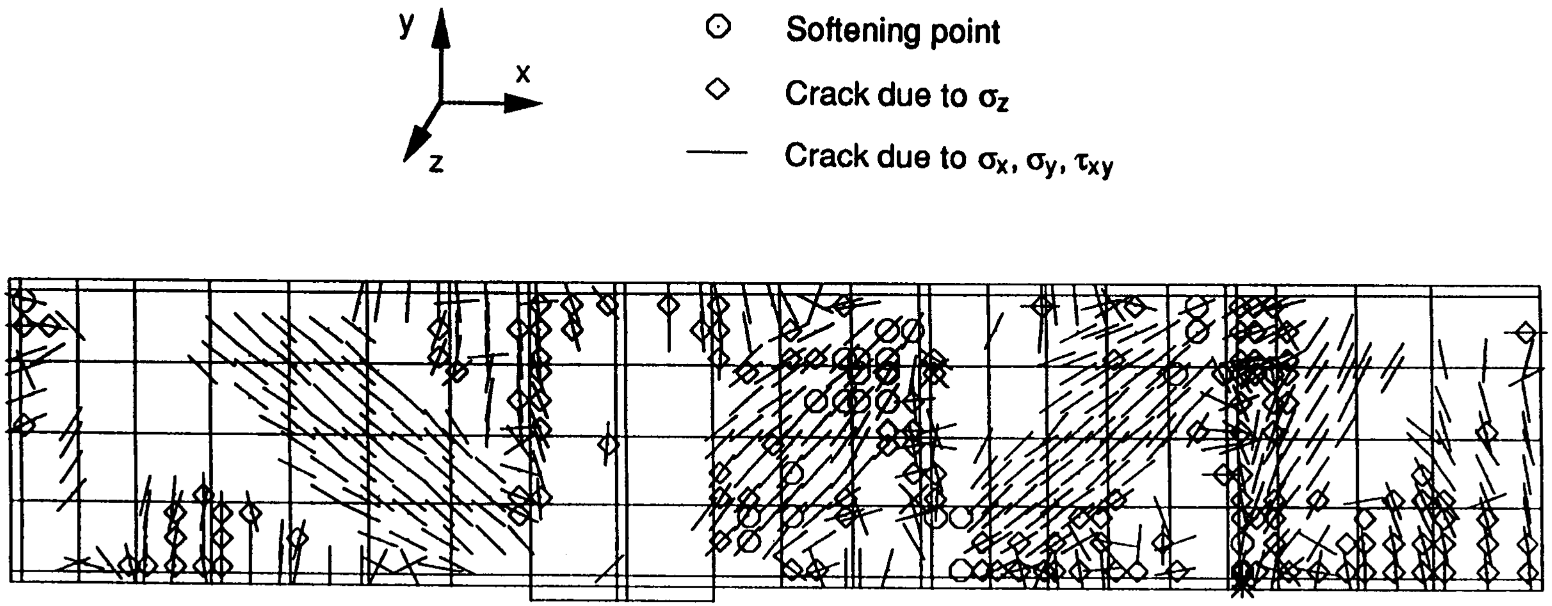

Figure 5.28 CF-8 nonlinear effects for d = 10.0 mm

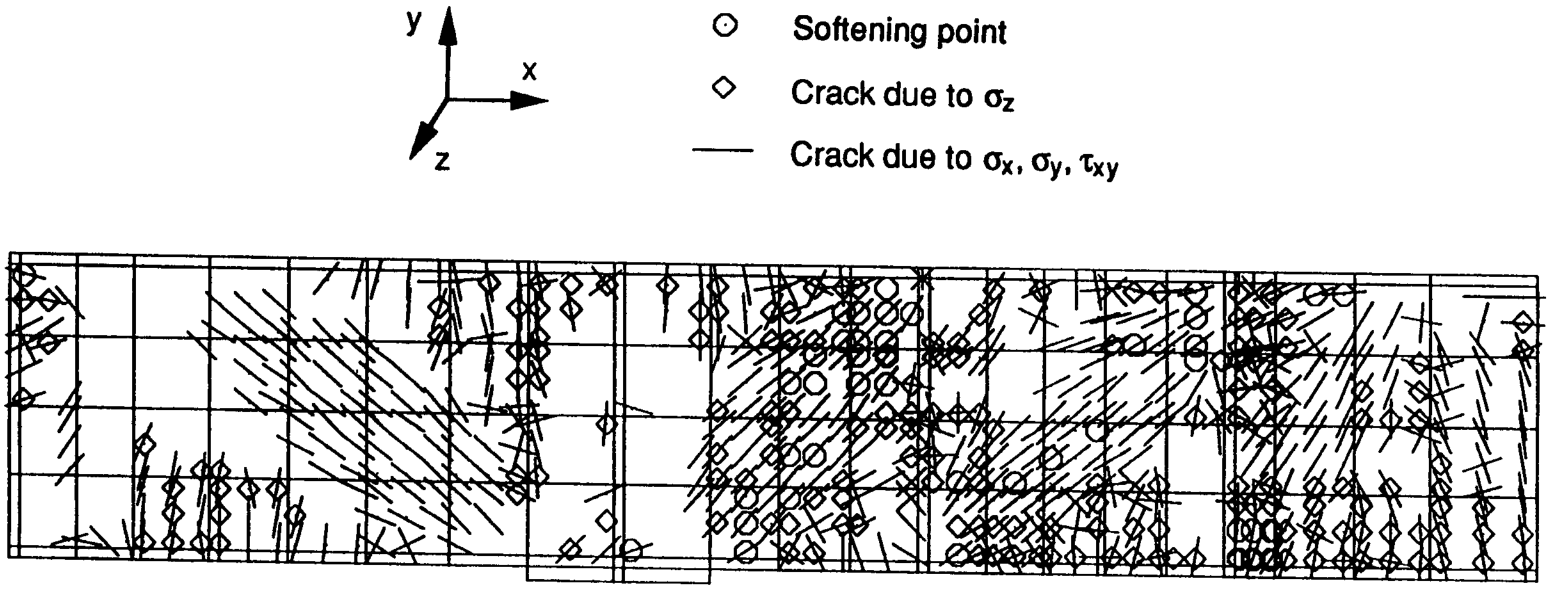

Figure 5.29 CF-8 nonlinear effects for d = 20.0 mm

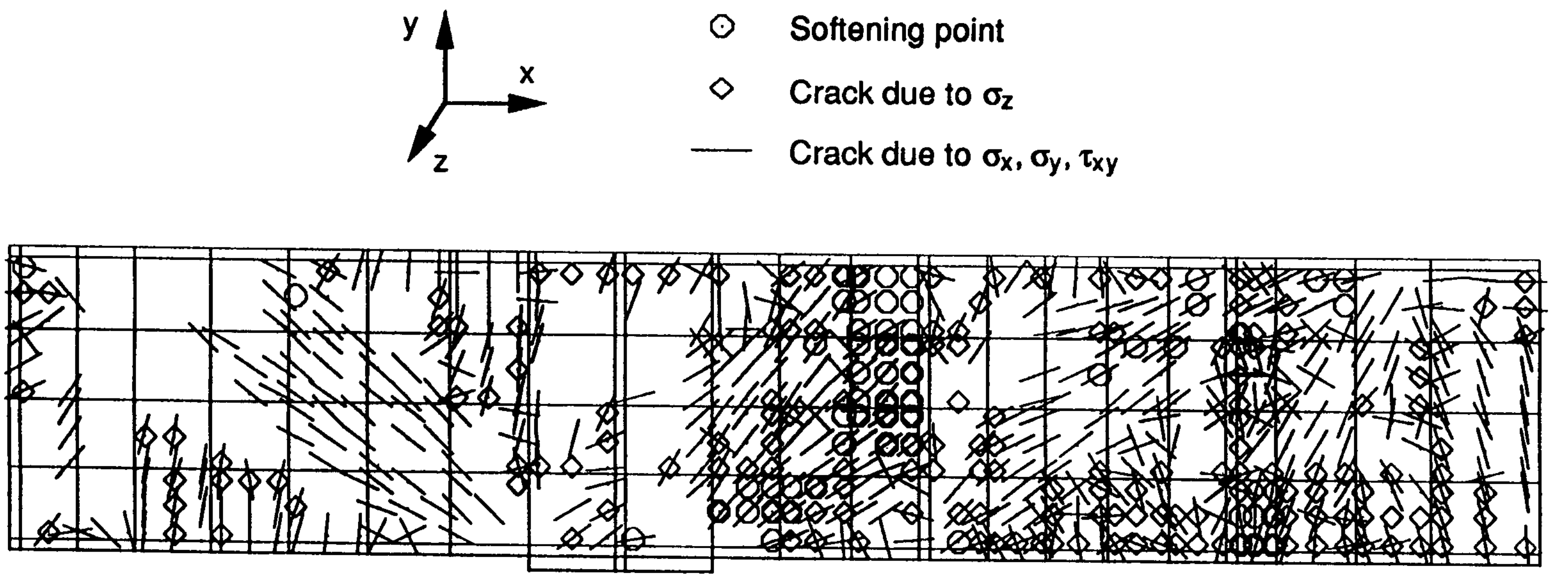

Figure 5.30 CF-8 nonlinear effects for d = 25.0 mm

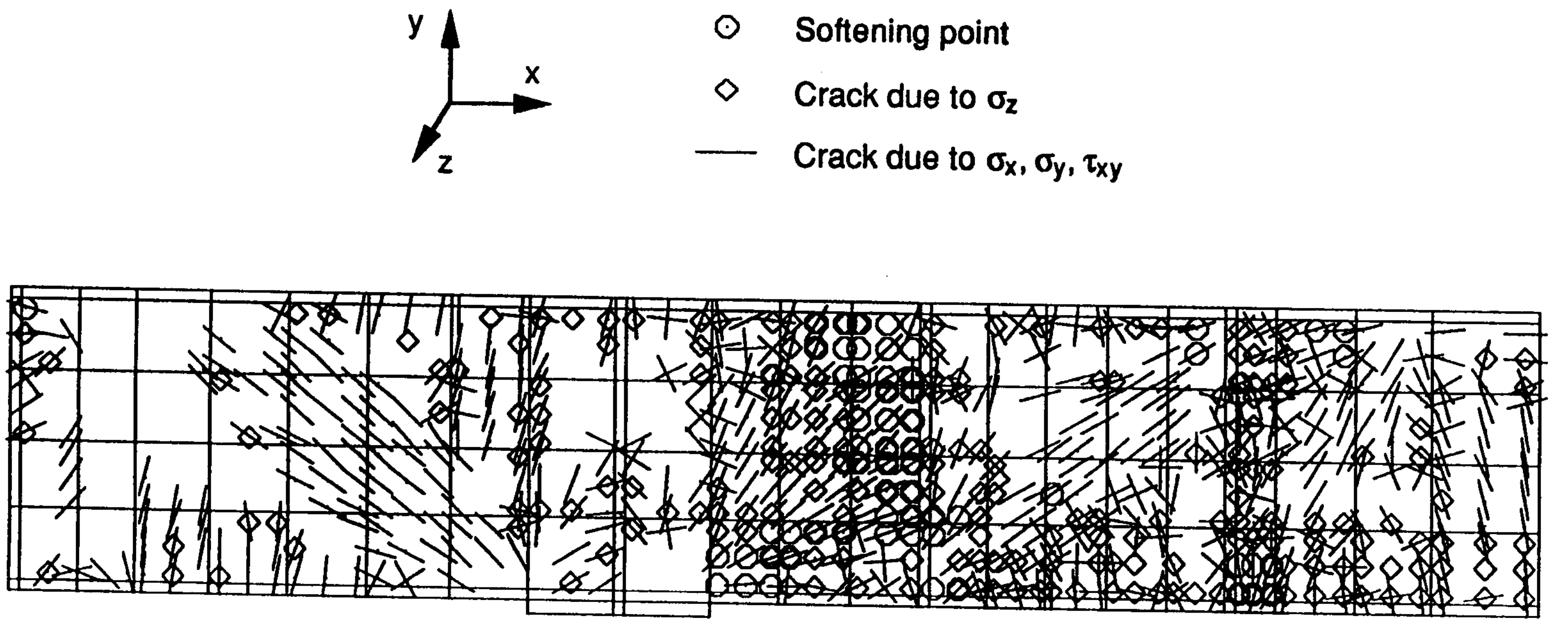

Figure 5.31 CF-8 nonlinear effects for d = 40 mm

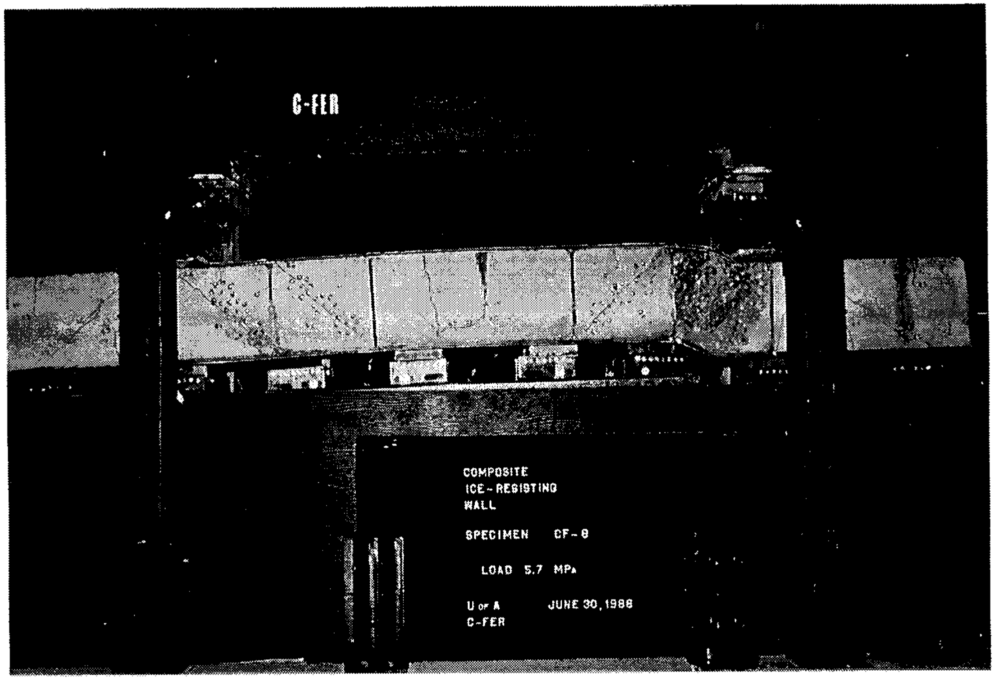

Figure 5.32 Photograph of failed specimen

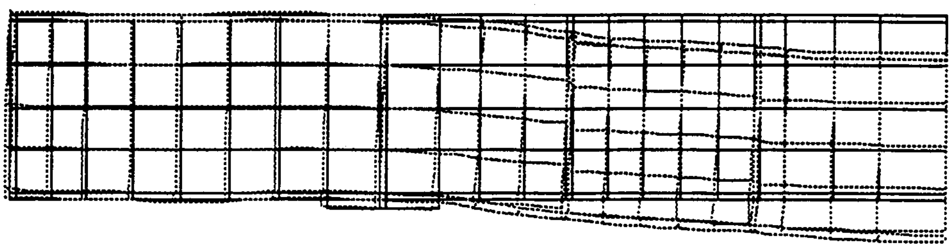

Displacement magnifier = 10

Figure 5.33 CF-8 deformed shape at d = 5.0 mm

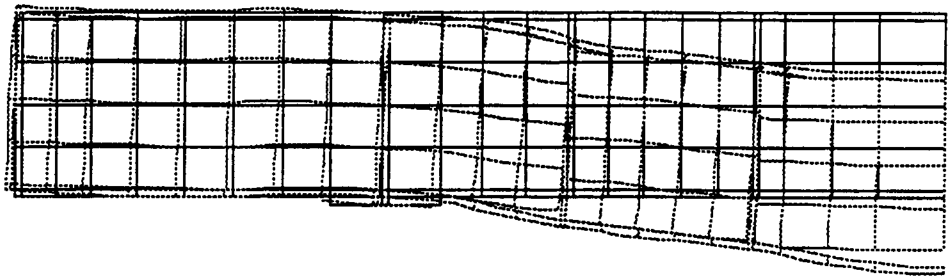

Displacement magnifier = 10

Figure 5.34 CF-8 deformed shape at d = 8.0 mm

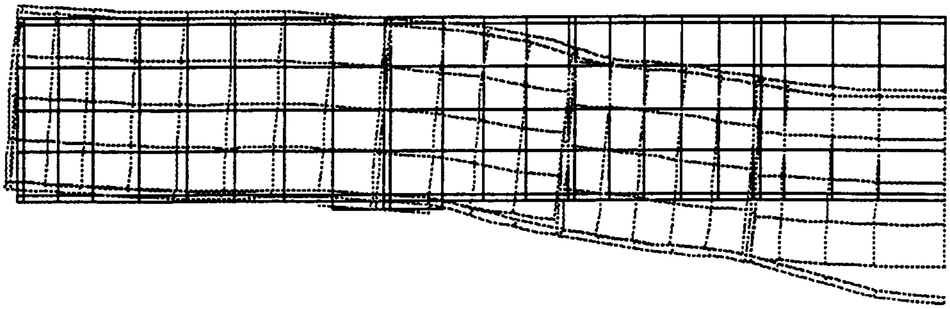

Displacement magnifier = 10

Figure 5.35 CF-8 deformed shape at d = 10.0 mm

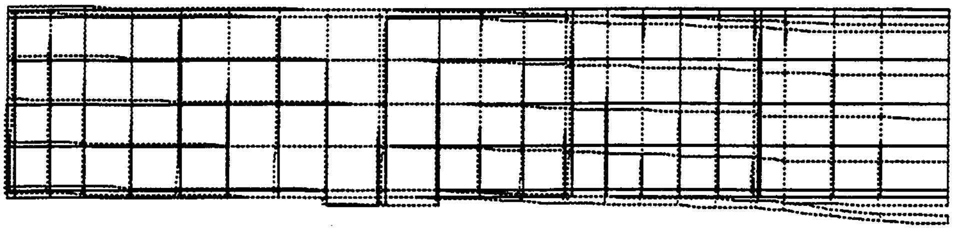

Displacement magnifier = 1

Figure 5.36 CF-8 deformed shape at d = 20.0 mm

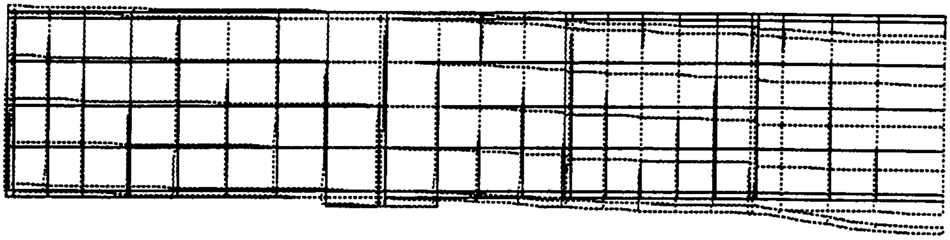

Displacement magnifier = 1

Figure 5.37 CF-8 deformed shape for d = 25.0 mm

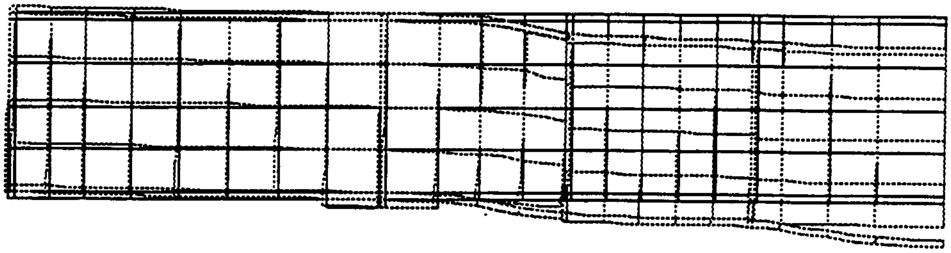

Displacement magnifier = 1

Figure 5.38 CF-8 deformed shape for d = 40.0 mm

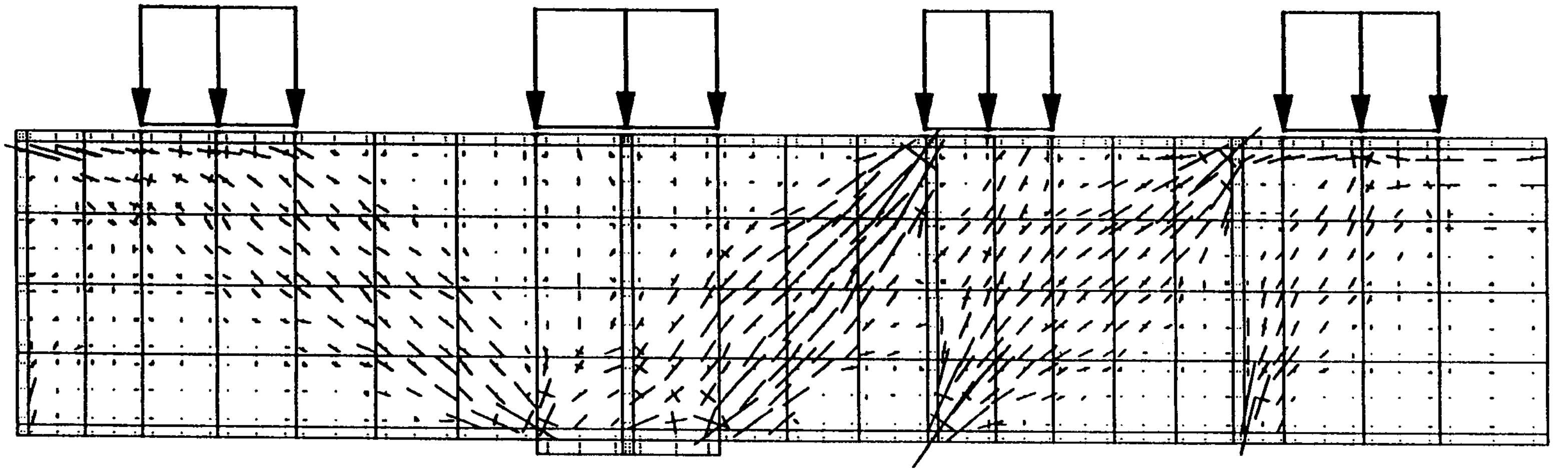

Stress plot scale = 175 MPa/cm

Figure 5.39 CF-8 local stresses for d = 5.0 mm

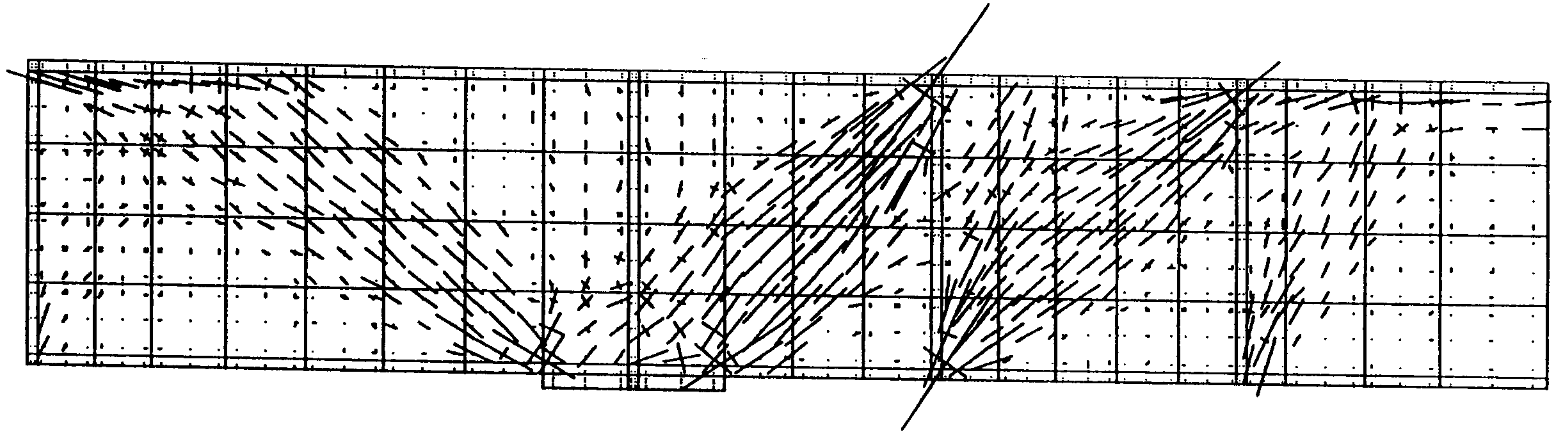

Stress plot scale = 175 MPa/cm

Figure 5.40 CF-8 local stresses at d = 10.0 mm

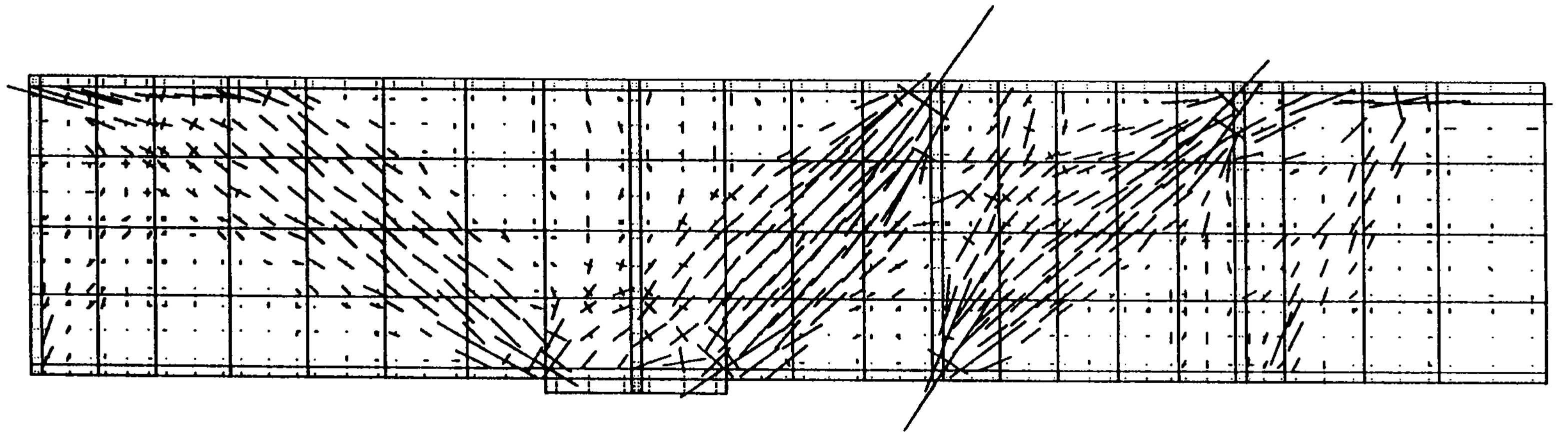

Stress plot scale = 175 MPa/cm

Figure 5.41 CF-8 local stresses for d = 20.0 mm

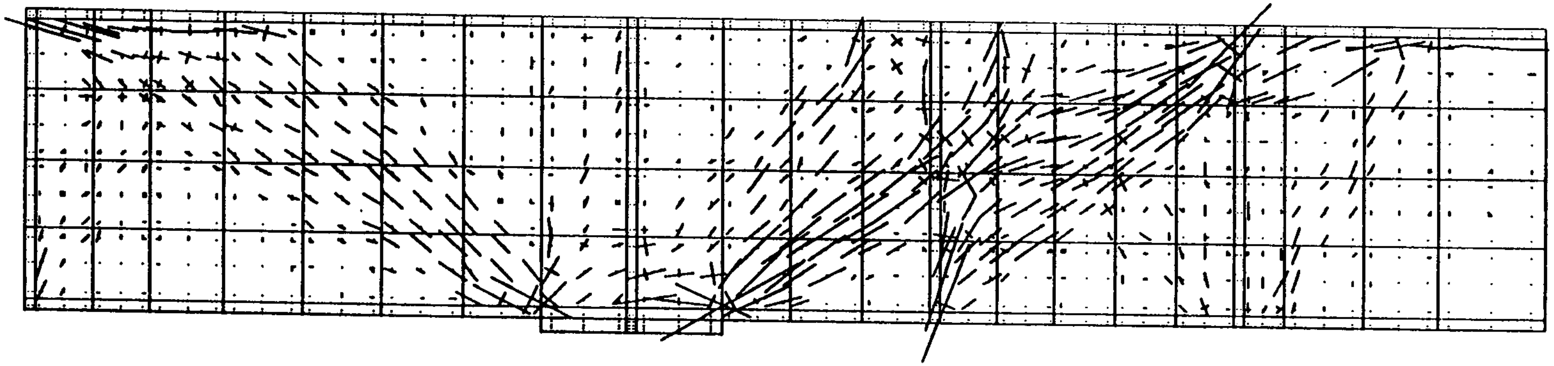

Stress plot scale = 175 MPa/cm

Figure 5.42 CF-8 local stresses for d = 25.0 mm

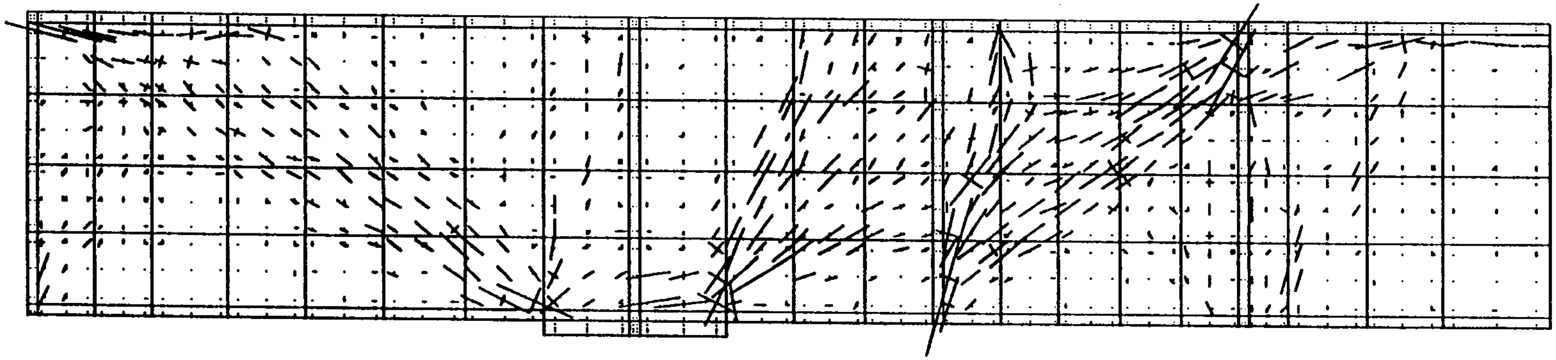

Stress plot scale = 175 MPa/cm

Figure 5.43 CF-8 nonlinear effects for d = 40.0 mm

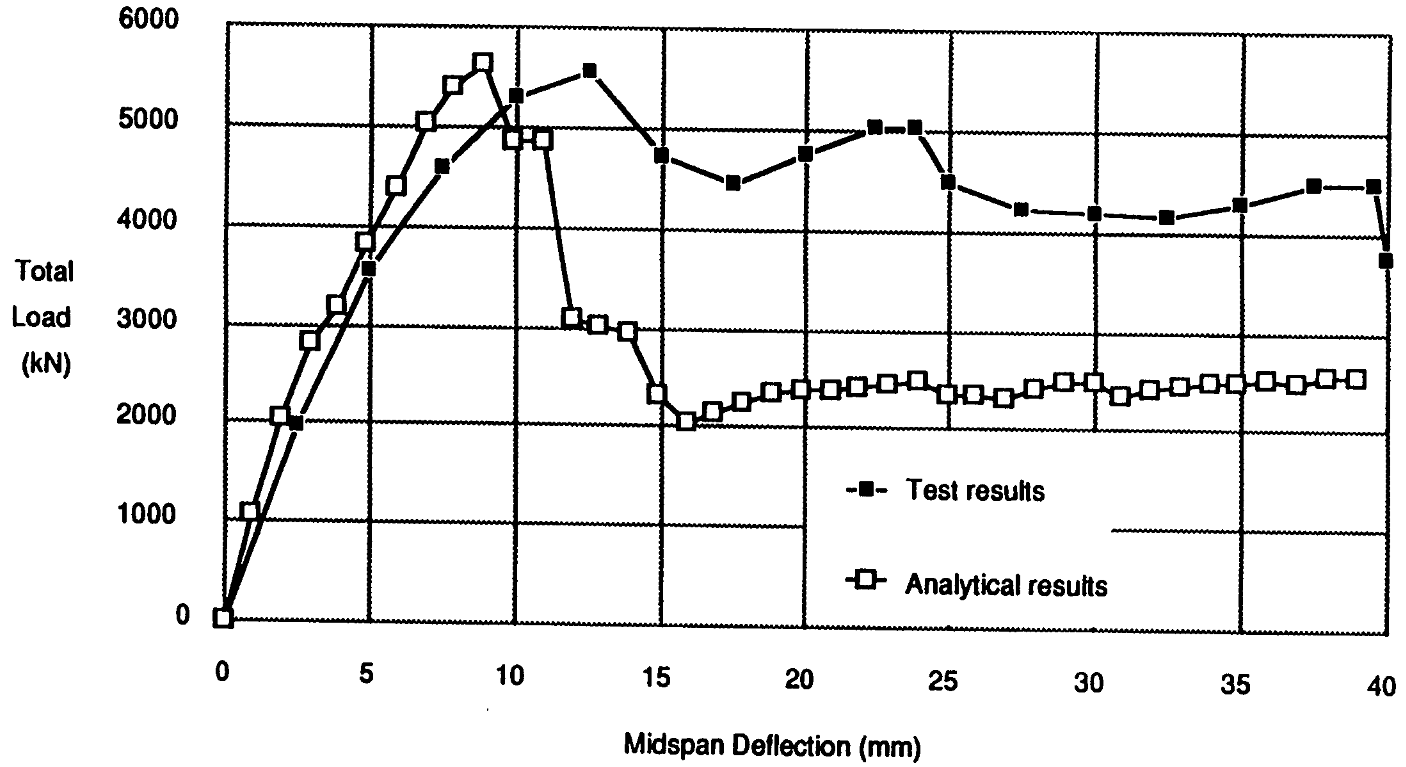

Figure 5.44 TF-1 load vs. midspan deflection plot

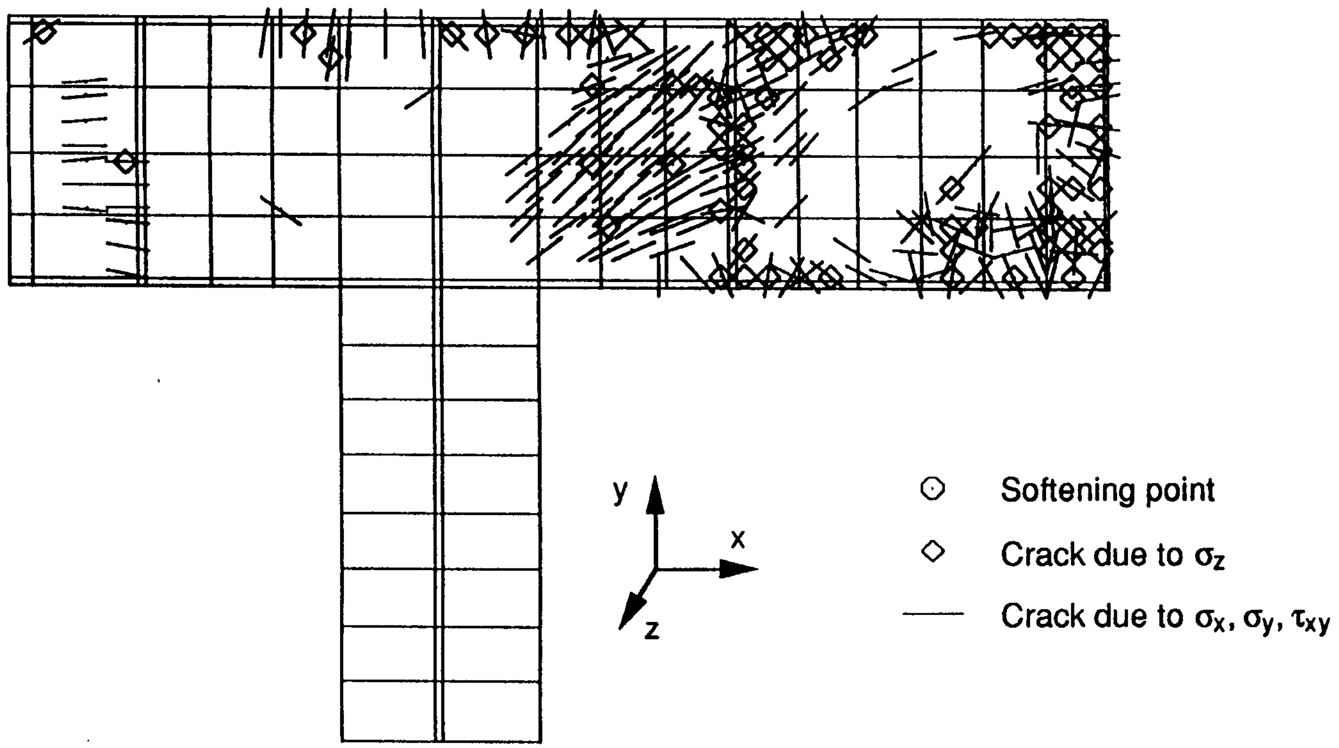

Figure 5.45 TF-1 nonlinear effects for d = 5.0 mm

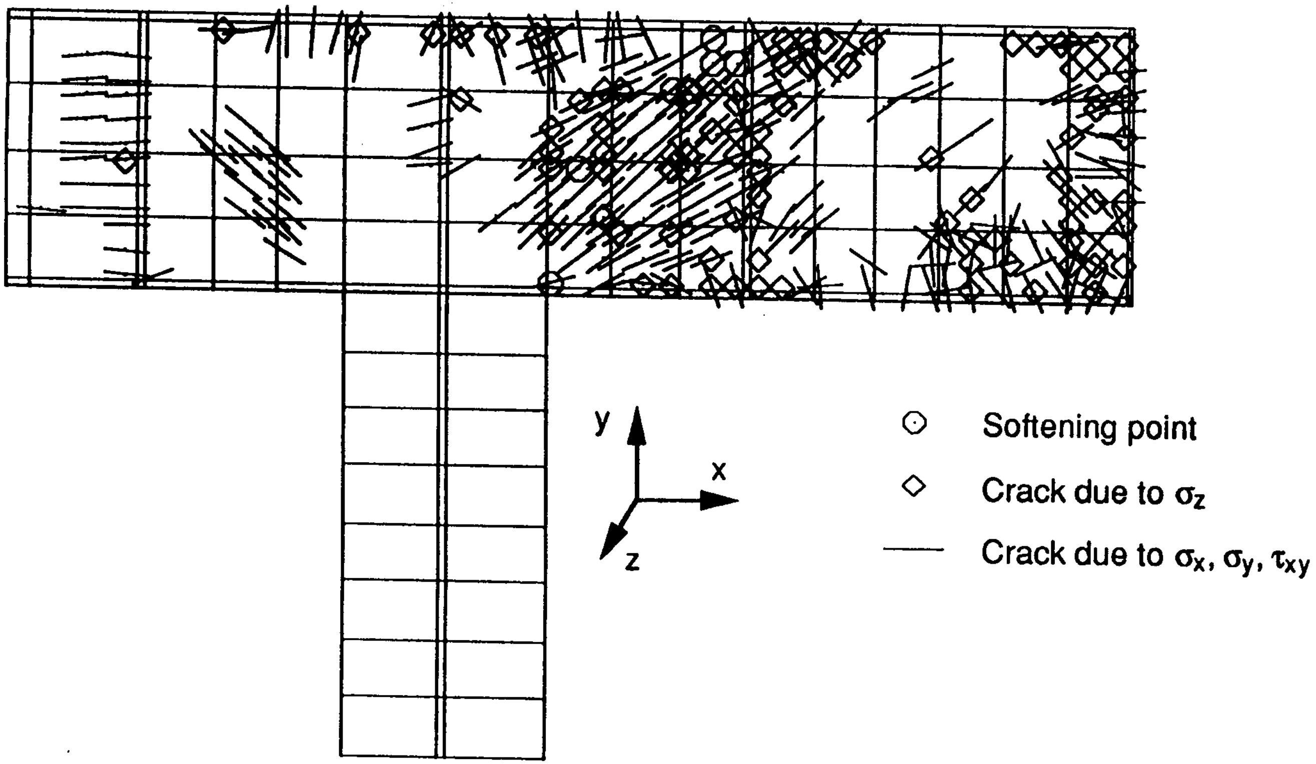

Figure 5.46 TF-1 nonlinear effects for d = 8.0 mm

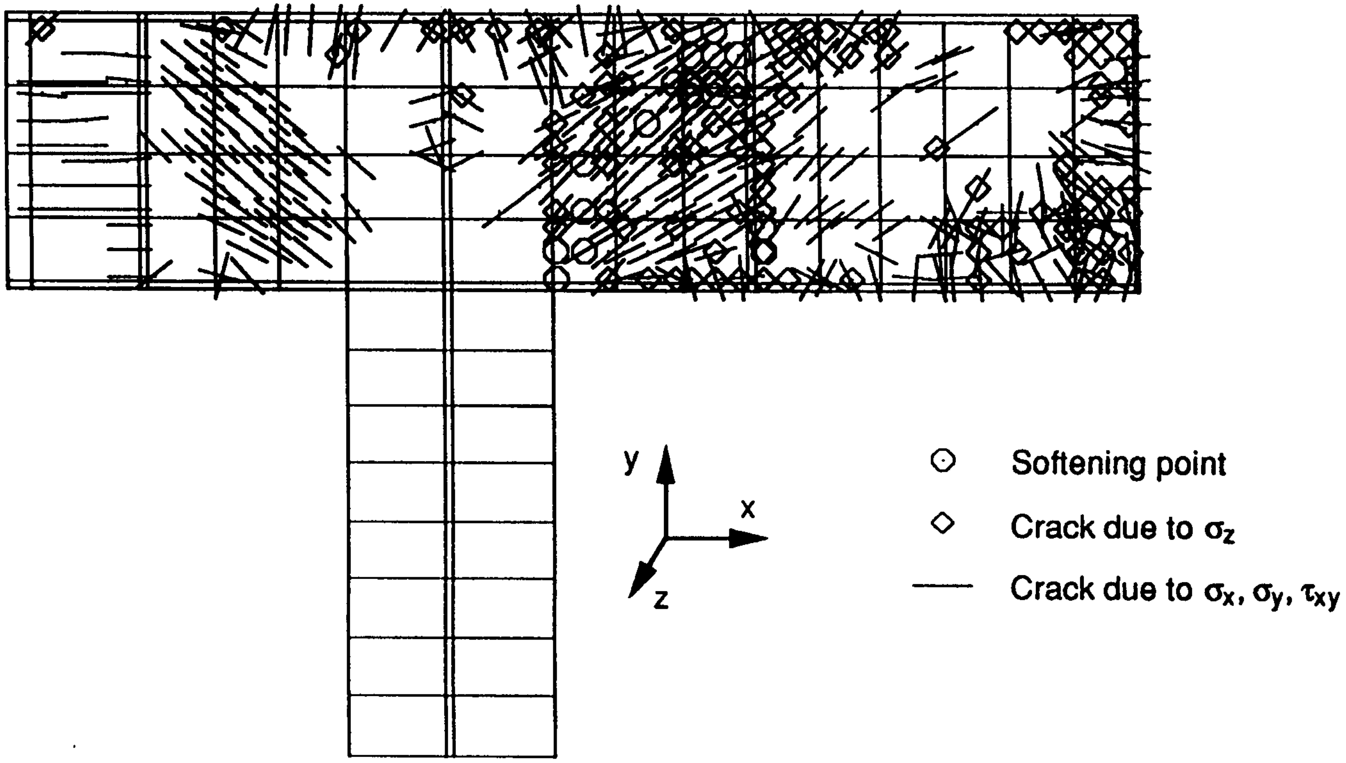

Figure 5.47 TF-1 nonlinear effects for d = 10.0 mm

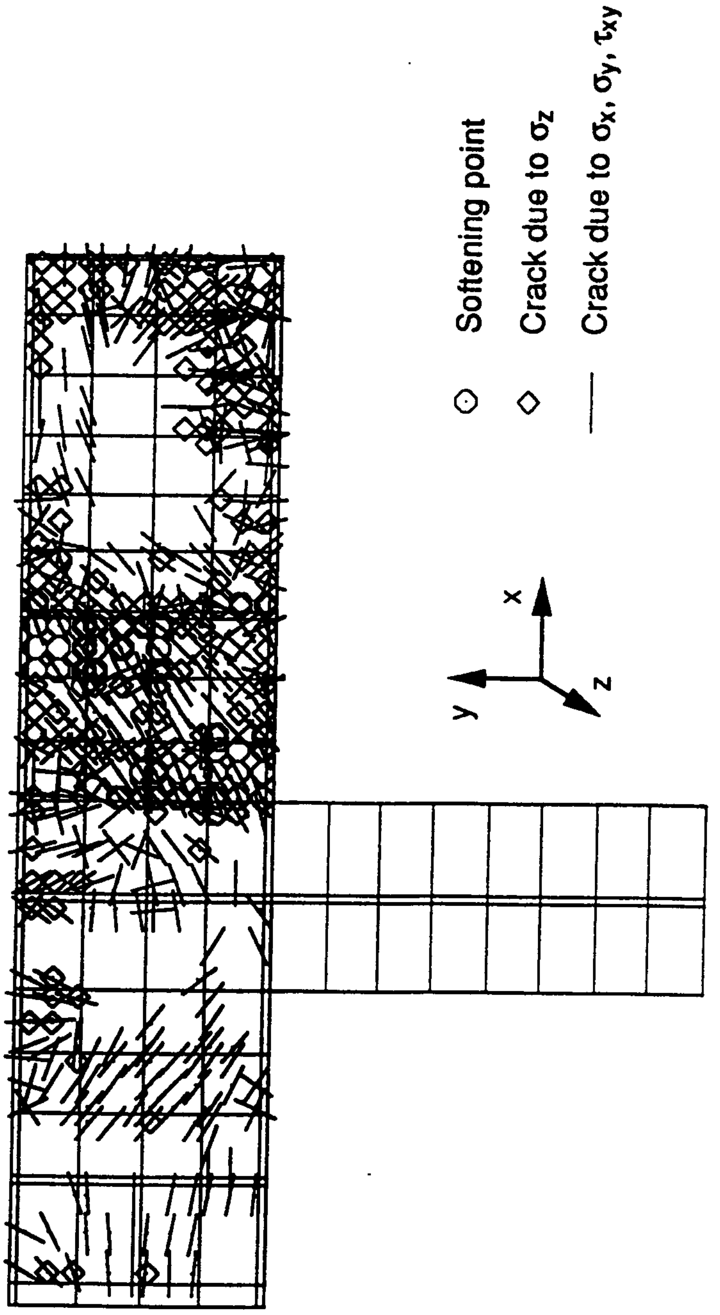

Figure 5.48 TF-1 nonlinear effects for d = 15.0 mm

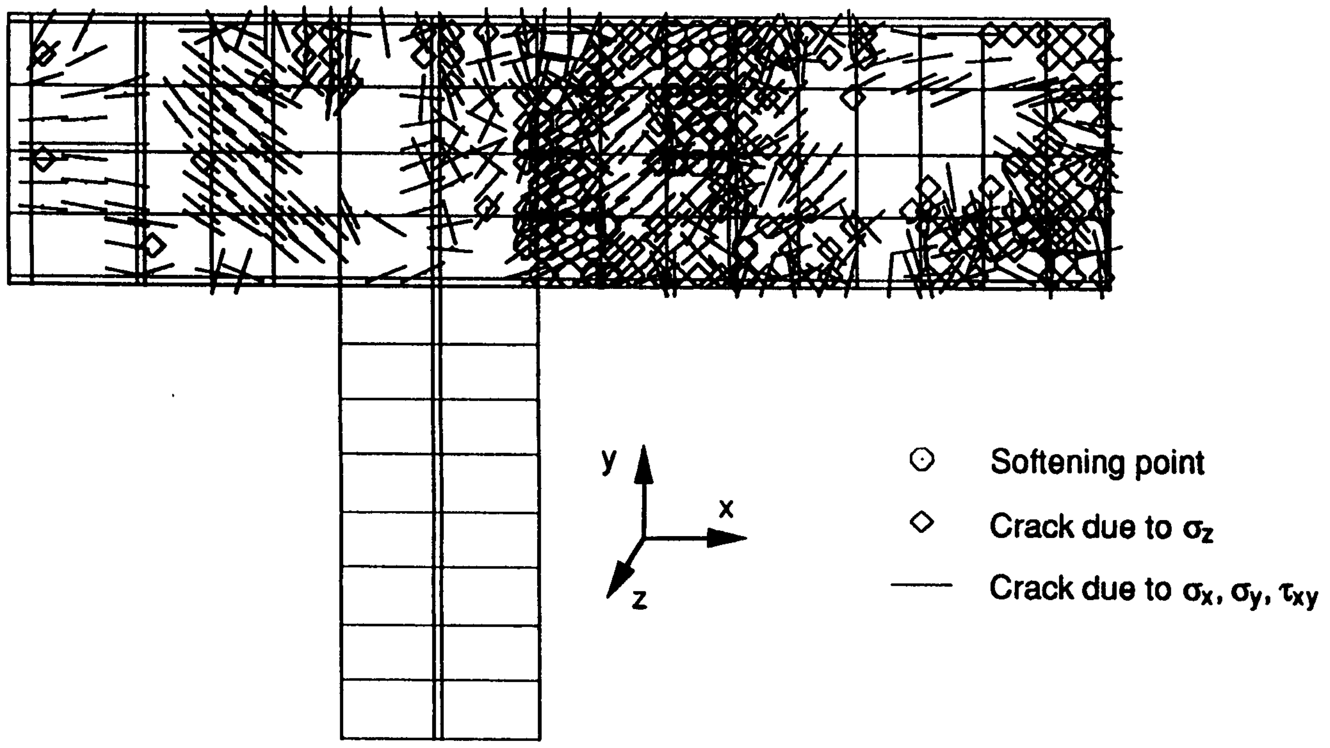

Figure 5.49 TF-1 nonlinear effects for d = 40.0 mm

Figure 5.50 Photograph of failed specimen

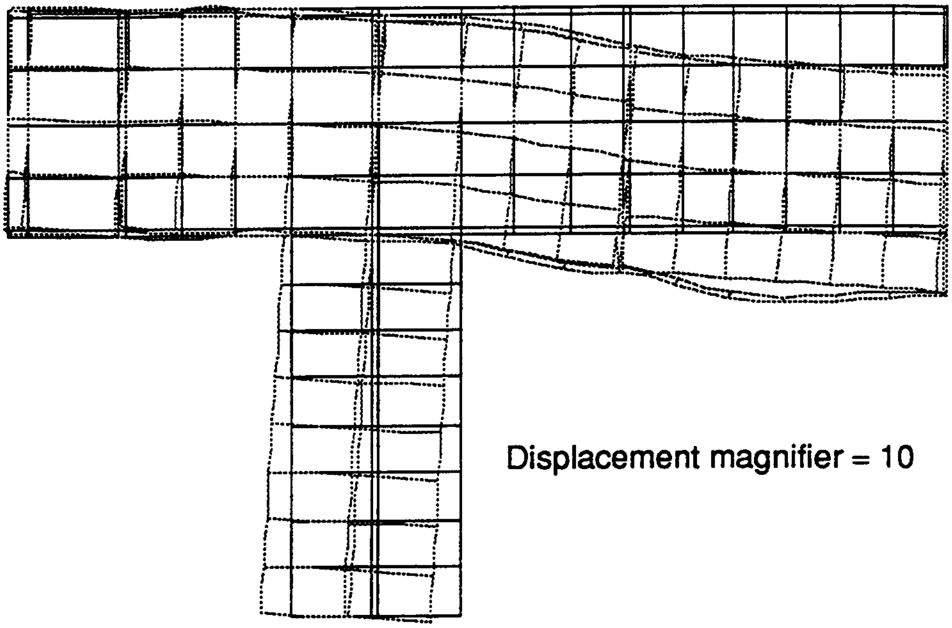

Figure 5.51 TF-1 deformed shape for d = 8.0 mm

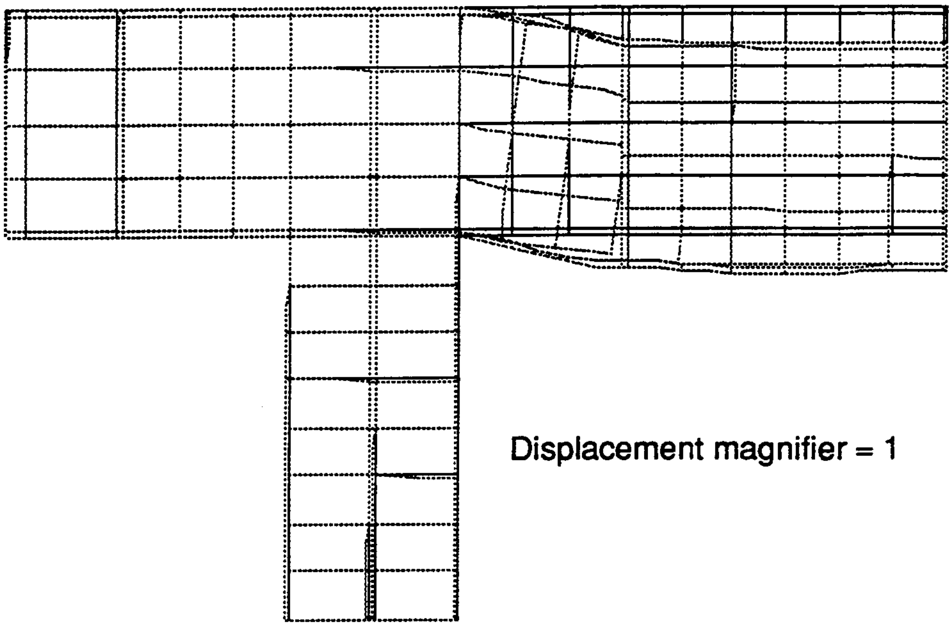

Figure 5.52 TF-1 deformed shape for d = 40.0 mm

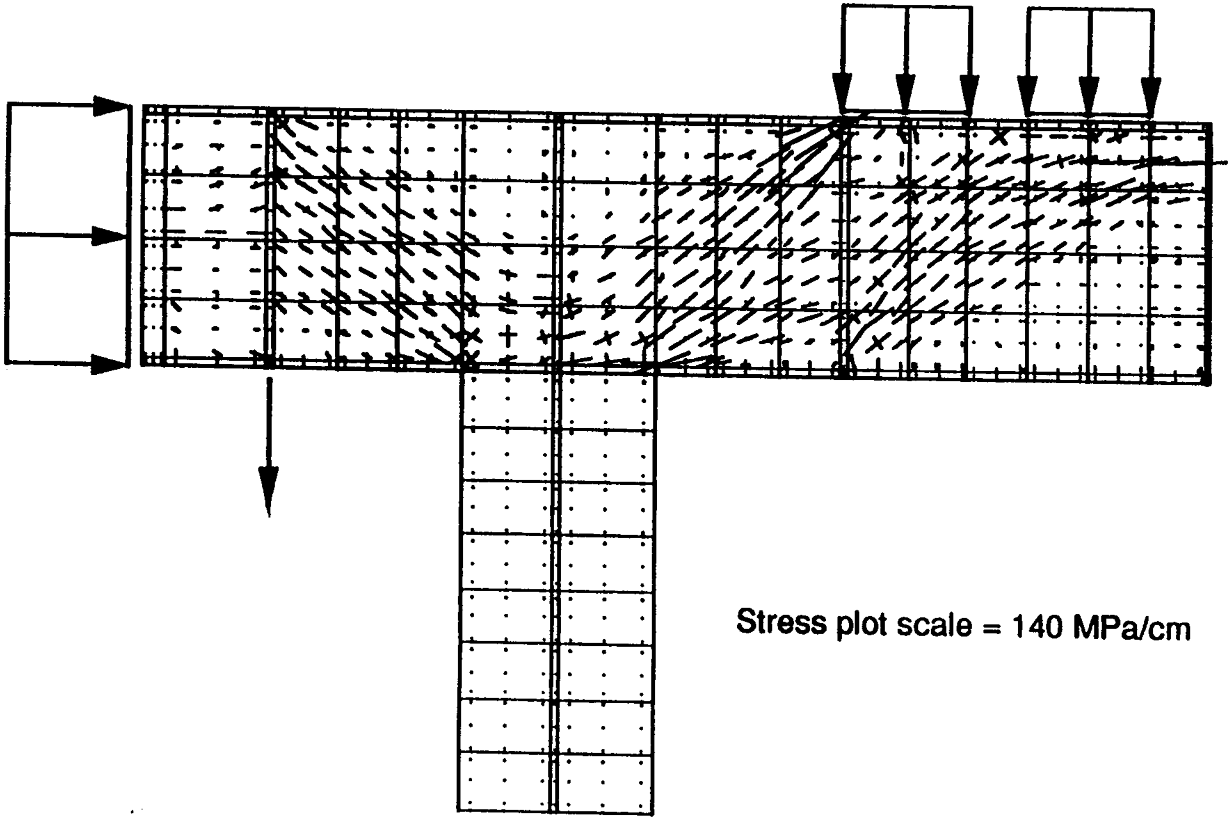

Figure 5.53 TF-1 local stresses for d = 5.0 mm

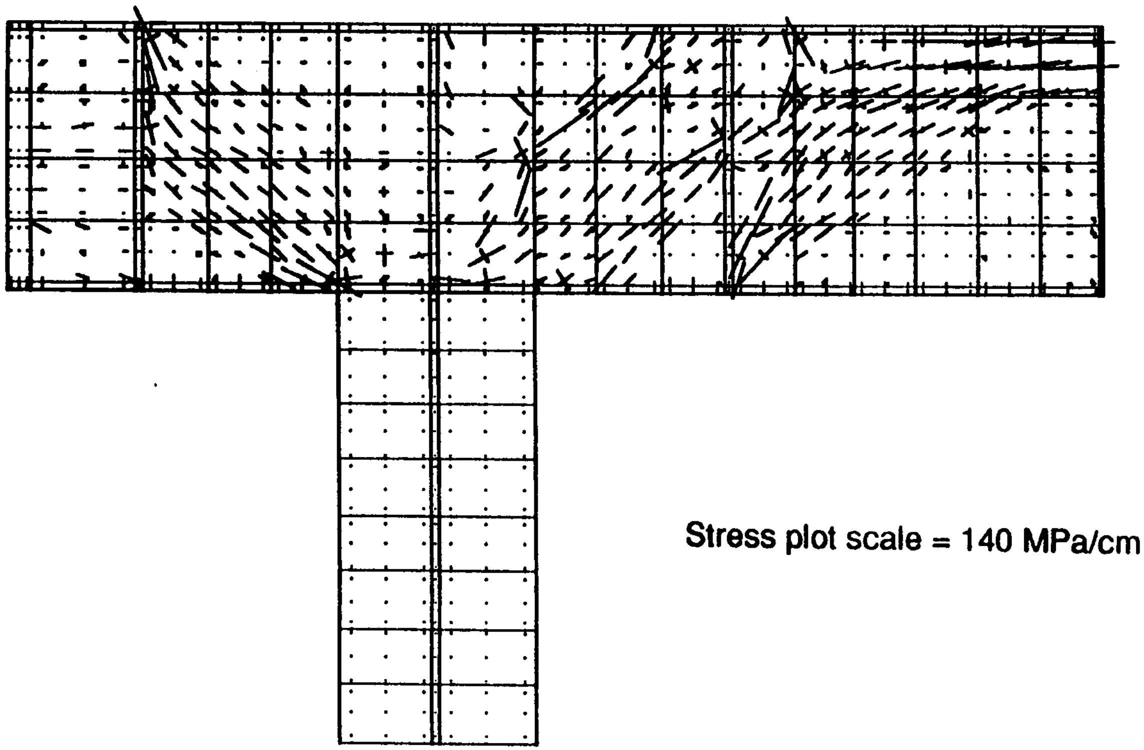

Figure 5.54 TF-1 local stresses for d = 40.0 mm

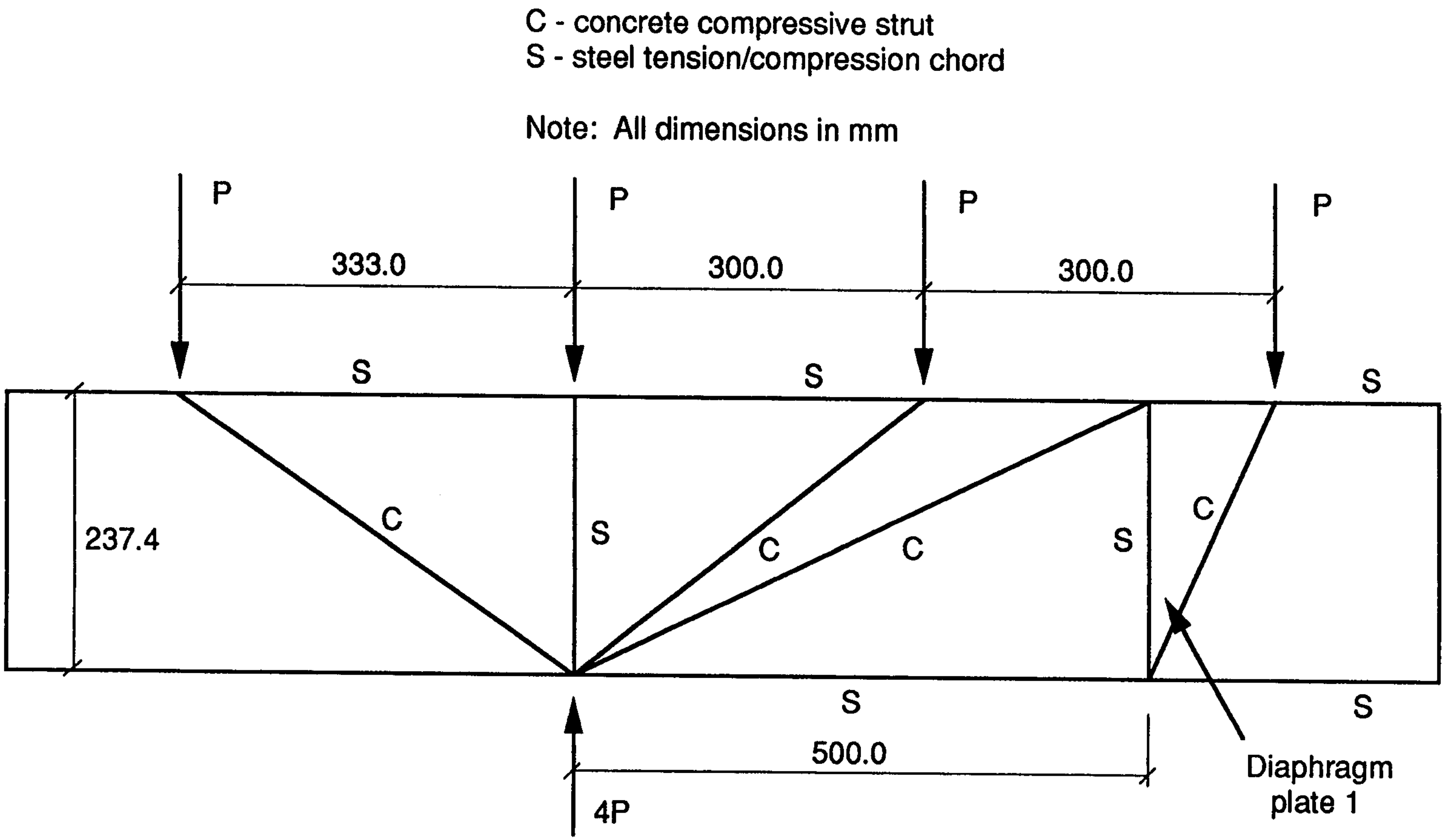

Figure 5.55 Strut and tie model for Specimen CF-4

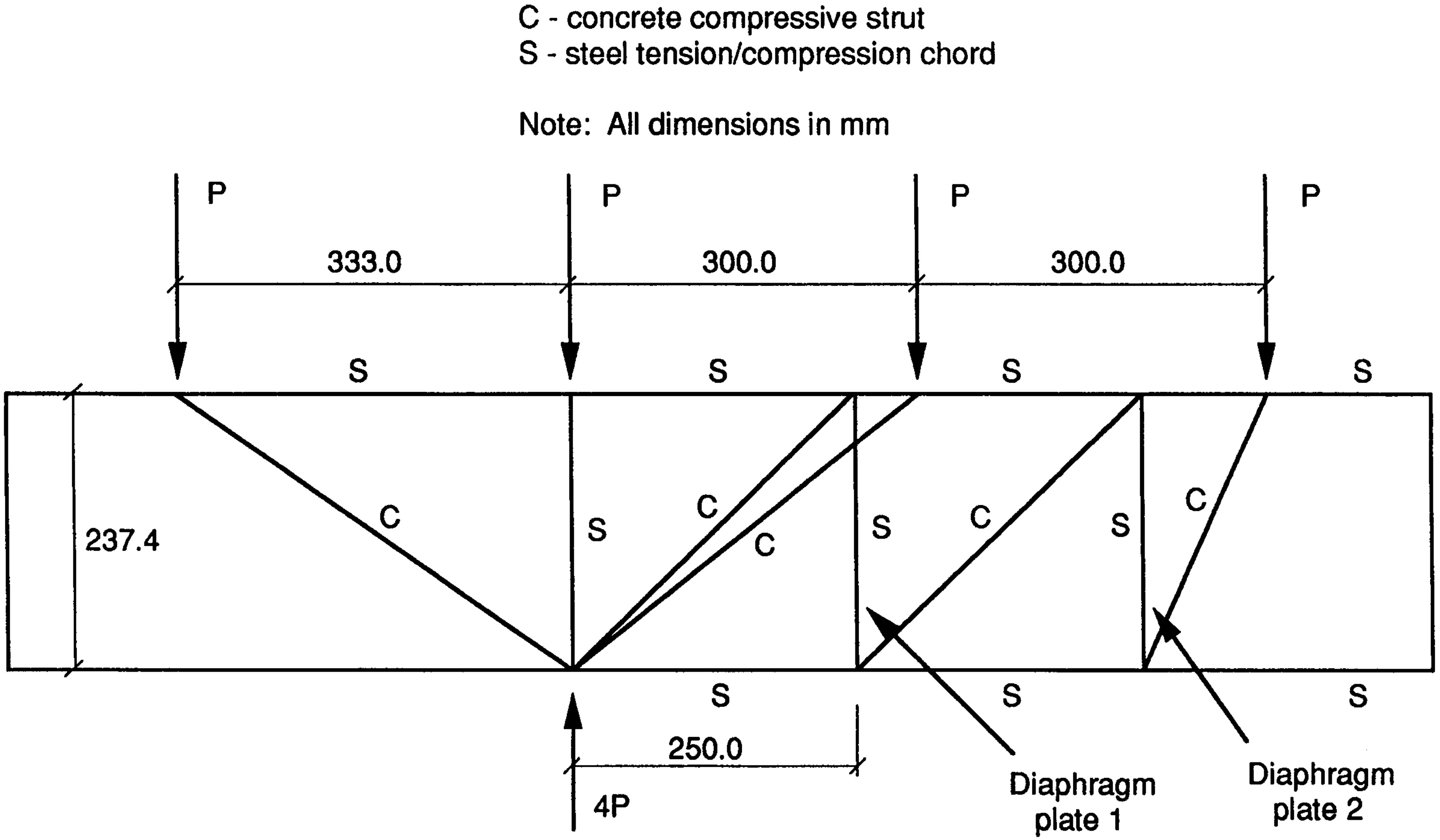

C - concrete compressive strut
S - steel tension/compression chord

Note: All dimensions in mm

Figure 5.56 Strut and tie model for Specimen CF-8

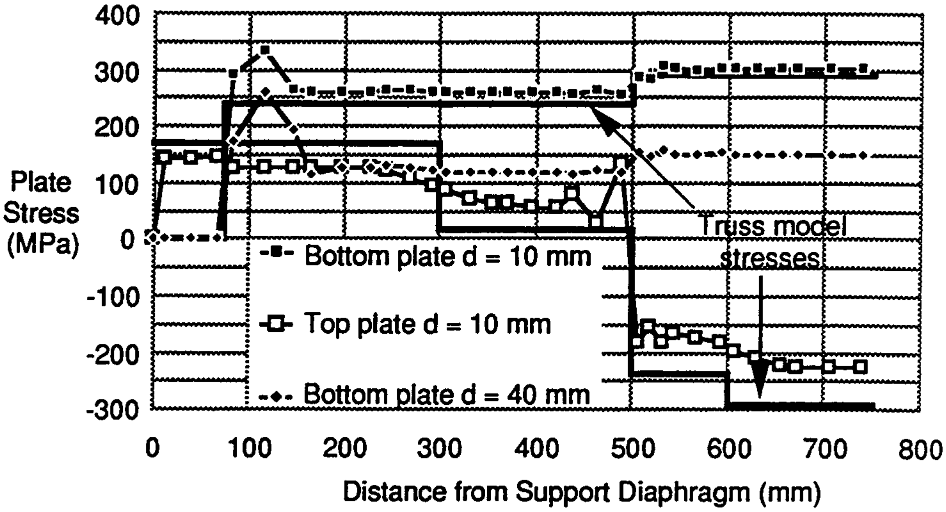

Figure 5.57 Plate stresses for Specimen CF-4

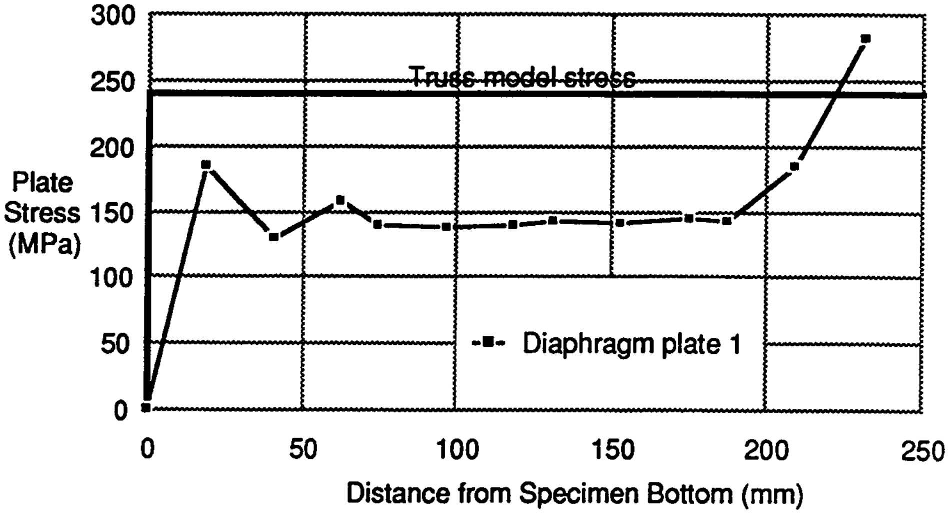

Figure 5.58 Diaphragm plate stresses for Specimen CF-4

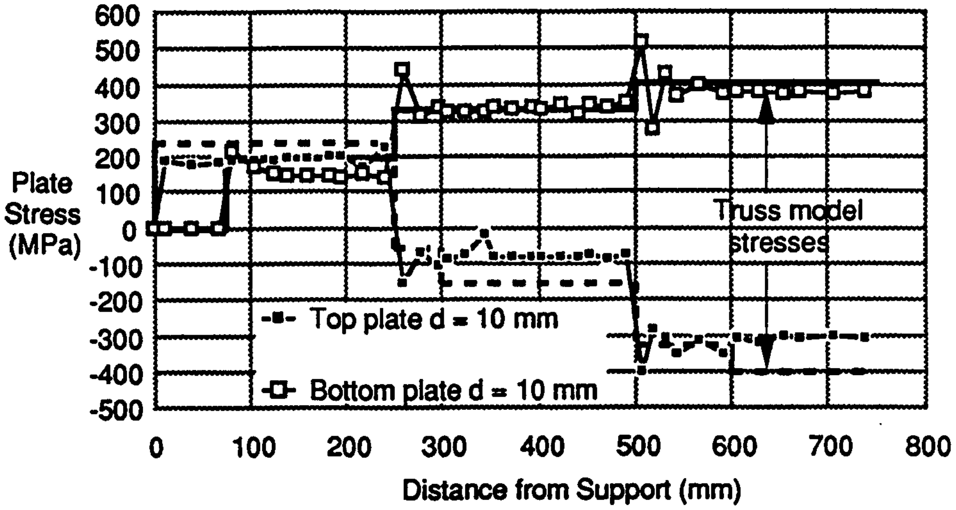

Figure 5.59 Plate stresses for Specimen CF-8

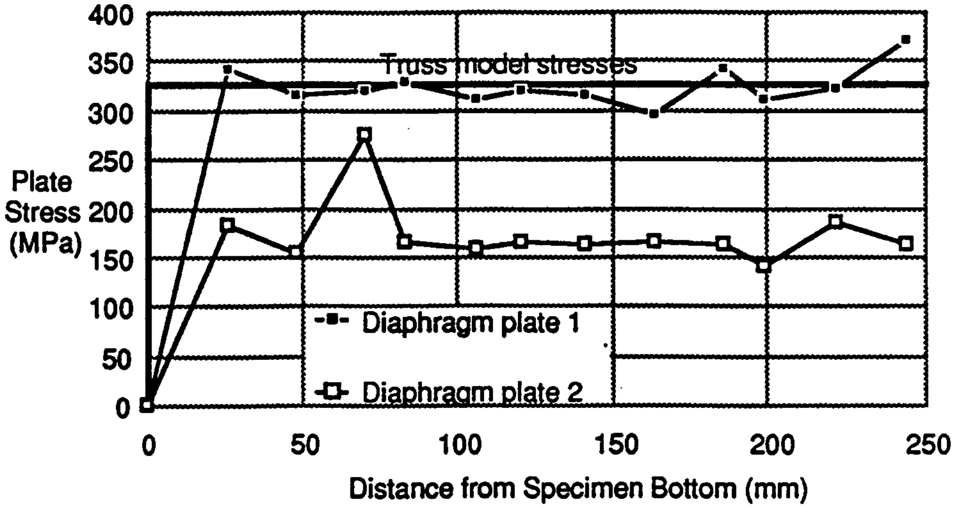

Figure 5.60 Diaphragm plate stresses for Specimen CF-8

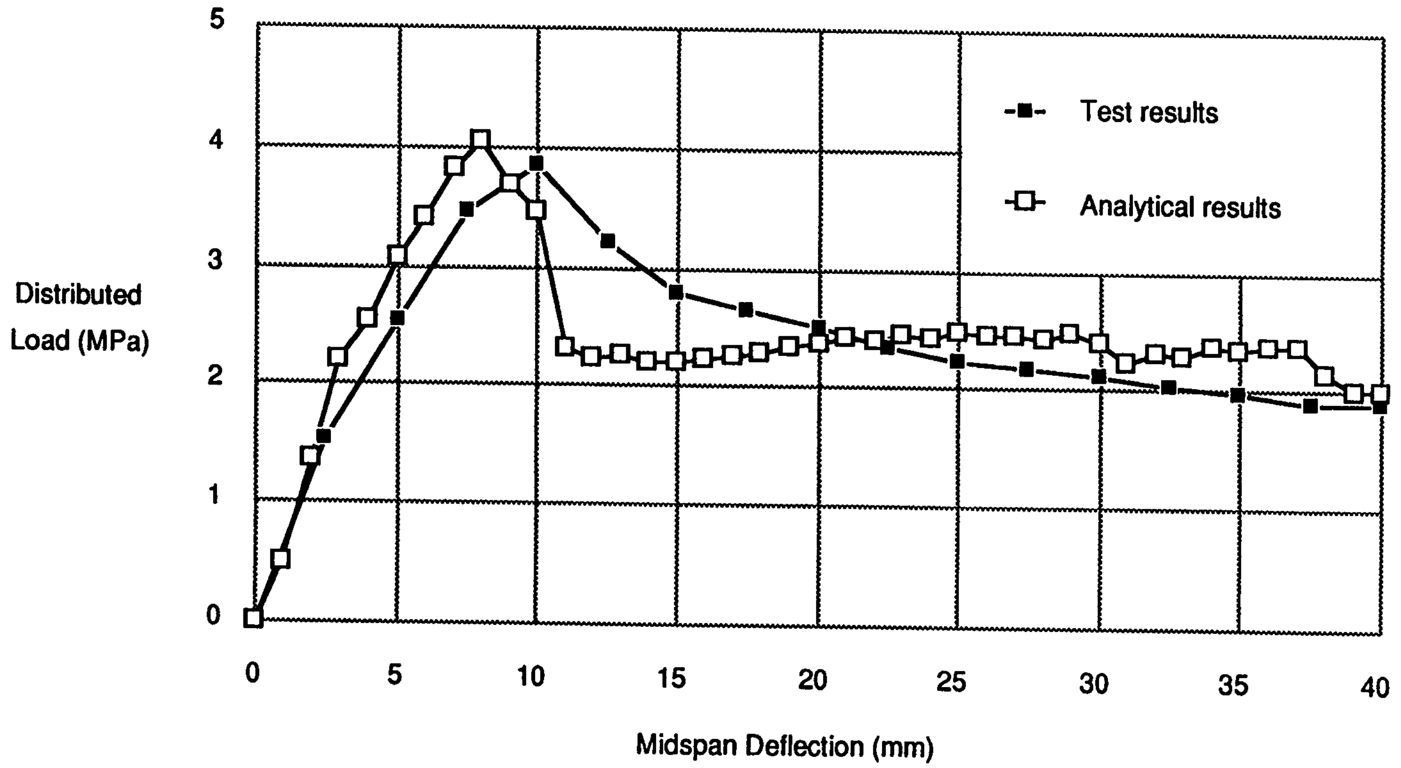

Figure 5.61 CF-5 load vs. midspan deflection plot

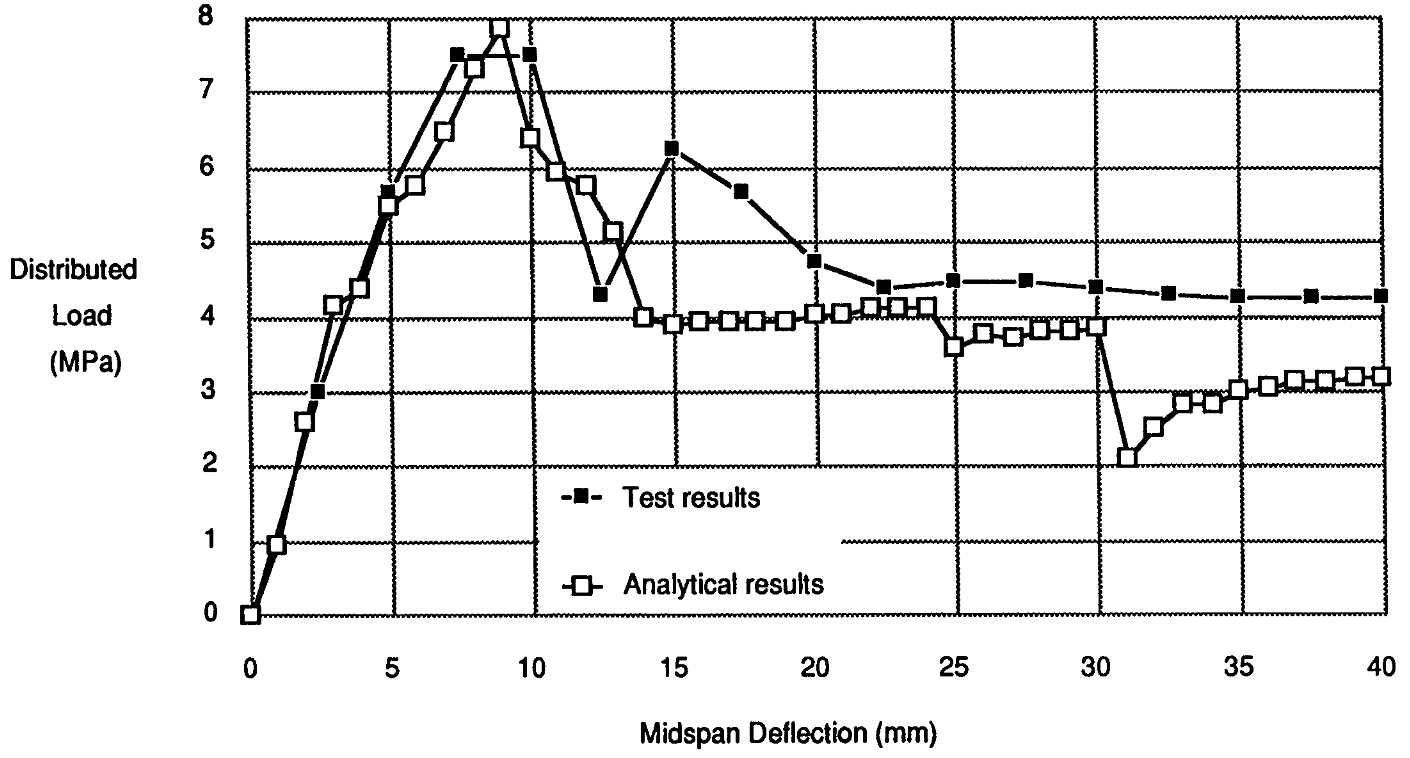

Figure 5.62 CF-13 load vs. midspan deflection plot

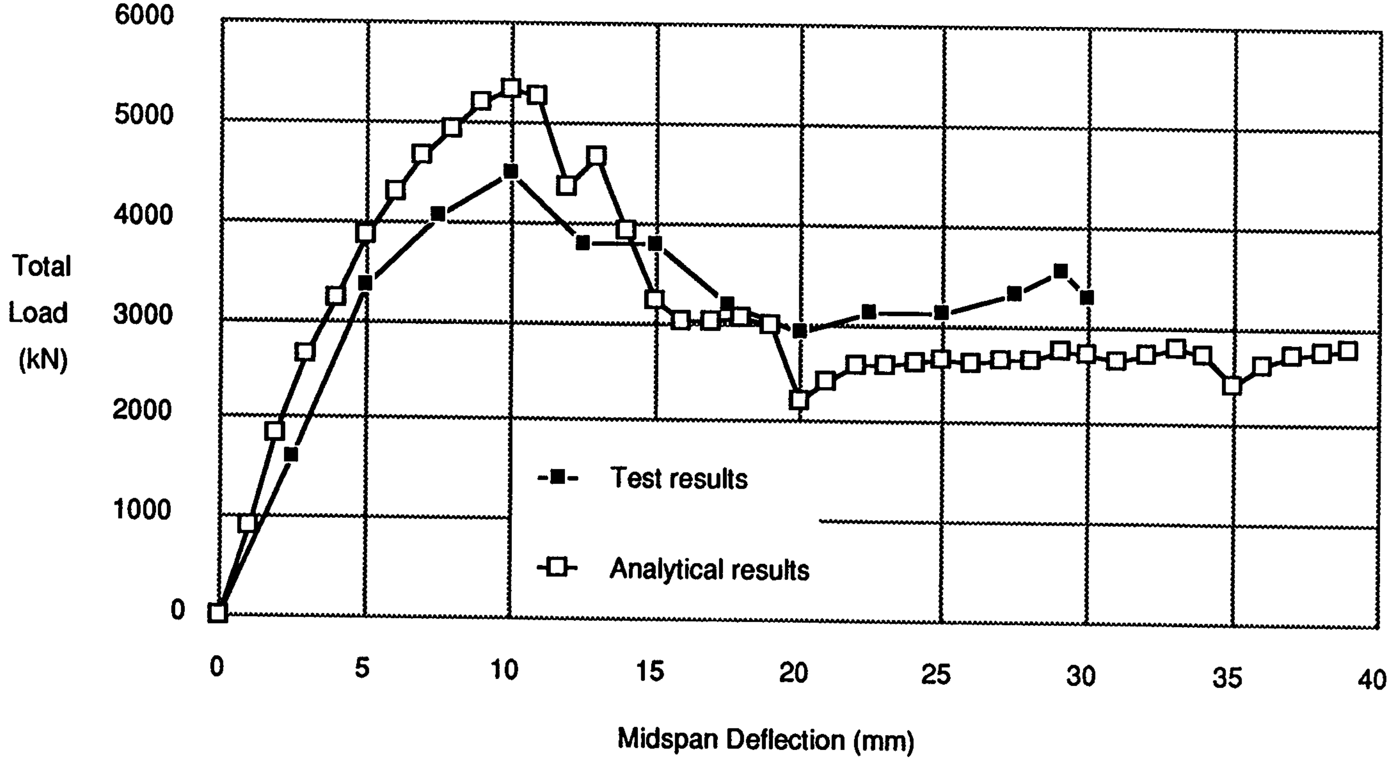

Figure 5.63 TF-2 load vs. midspan deflection plot

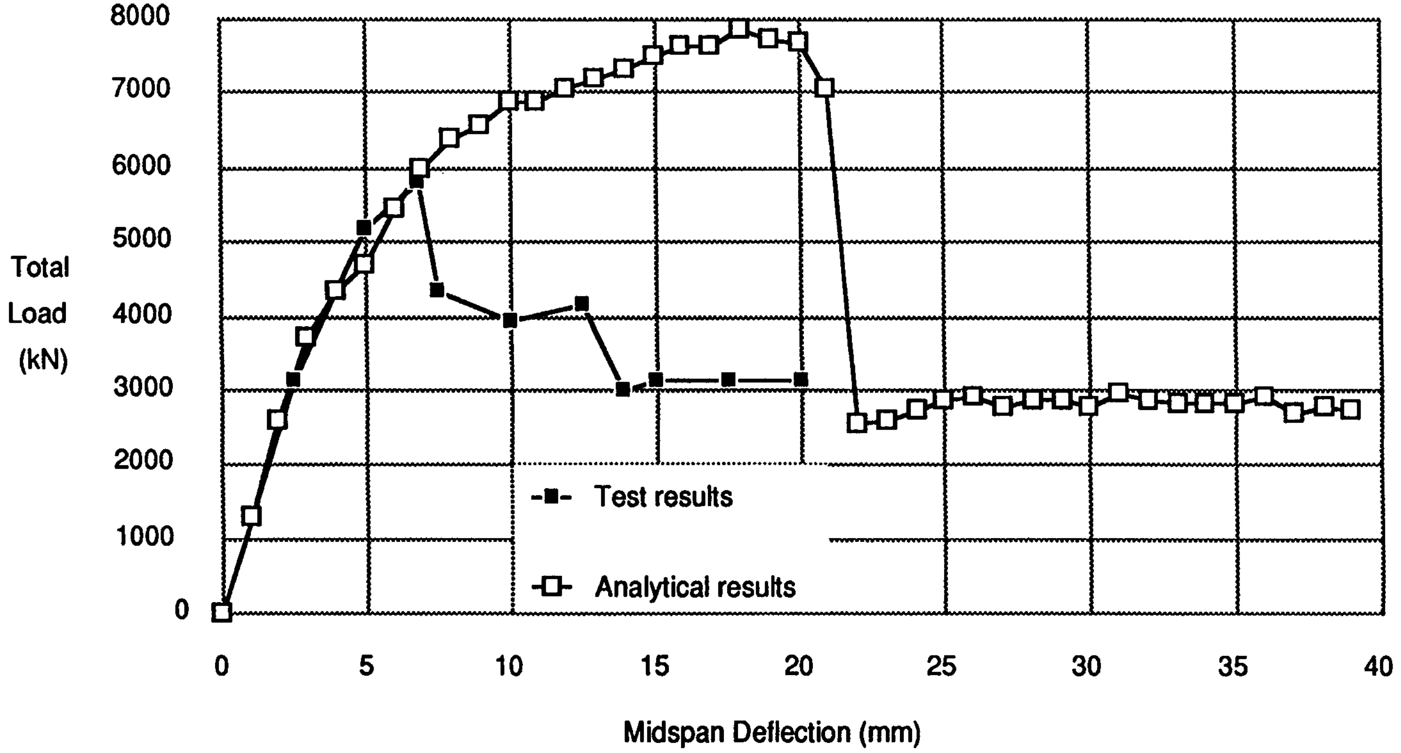

Figure 5.64 TF-4 load vs. midspan deflection plot

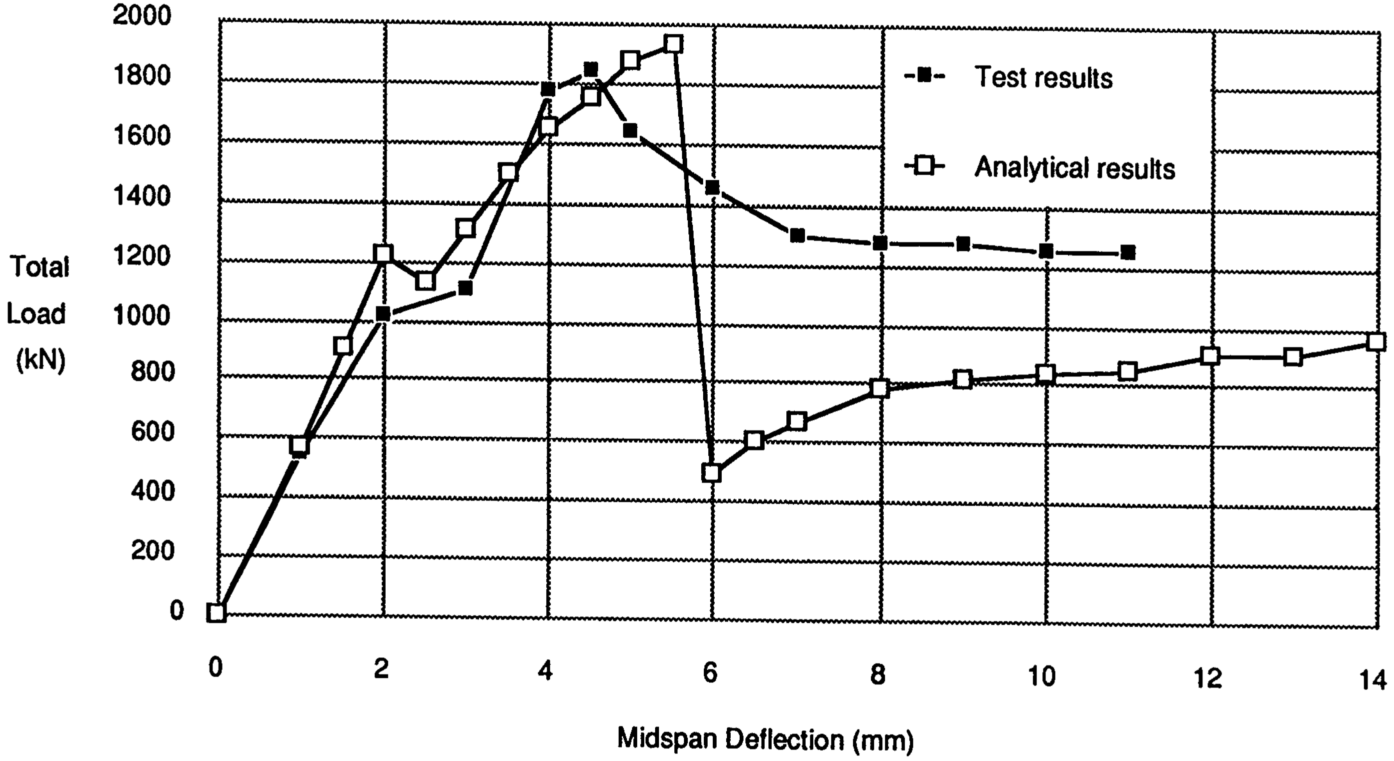

Figure 5.65 VTT3 load vs. midspan deflection plot

6.0 SUMMARY AND CONCLUSIONS

A literature review was performed summarizing the significant research regarding the design, testing, and analysis of composite ice resisting walls. It was concluded from examination of the current Canadian design standard (CSA S474-M1989) that an estimate of member ultimate strength and post-peak strength were essential for an adequate limit states design. Current design methods were found to concentrate principally on the member ultimate strength, and were found to lack generality. No design method was found to evaluate post-peak strength, except for the case of very thin (membrane) members.

Existing finite element analyses of composite ice resisting walls were found to concentrate mainly on the case of flexural failure, even though a substantial number of tested specimens failed in shear-compression. No evaluation of post-peak behaviour was presented in any previous finite element study.

A three dimensional hypoelastic concrete constitutive model was developed which is able to consider stress-strain behaviour in both the pre-peak and softening ranges. A secant method was adopted in order to enhance numerical stability, and the model included provisions for nonlocal (mesh dependent) effects due to softening in both tension and compression.

The softening characterization involved the use of an exponentially decaying descending branch in both tension and compression. The fracture energy approach used by Bazant and Oh (1983) was used as a basis for the rate of stress decrease. Since no data was available reporting uniaxial compressive fracture energy, a parametric study was performed using concrete cylinders to obtain an estimate of the compressive fracture energy. This was used in conjunction with effectiveness factor data reported by Neilsen (1980) to obtain a compressive uniaxial descending branch.

Sophisticated finite element models of selected walls from C-FER's database were developed. The selected walls represented a variety of structural configurations and loading types. The models included the interface between the steel and concrete by utilizing Lagrangian multiplier gap elements, and the steel was considered an elastic-plastic material. Post-peak behaviour was traced by using the displacement control method.

The models gave results which were consistent with experimentally observed behaviour. The analytical load versus midspan deflection curves were similar to those obtained from experiment. Nonlinear effects, such as diagonal cracks in the shear cells and initiation of crushing in shear critical areas, was duplicated in all eight analyses performed. The models predicted the failure mode correctly for all eight tests. Satisfactory overall test to predicted ratios were obtained for both ultimate strength and post-peak strength, with mean values of 0.93 and 1.09 respectively. The obtained solutions were numerically stable, thus indicating the robust nature of the concrete constitutive model.

Overall, the assumption of plane strain boundary conditions produced good results for both ultimate and residual load levels. This assumption may not be valid for the steel plates, as evidenced by the lack of a yield plateau in the analysis of specimen CF-8.

The gap elements adopted in the analysis gave results that were physically realistic. Areas of seperation and frictional slip were consistent with those reported in tests. The adopted friction coefficent of 0.5773 may have been too large; finite element results were generally stiffer in the pre-peak range. A value of 0.4 to 0.5 may be more appropriate for use.

In all of the analysed walls, the observed load carrying mechanism was similar to that of a strut and tie model. Principal stress trajectories, along with plate stresses obtained from a simple model, support this conclusion. After the peak load was reached, residual loads were sustained as a result of significant stress redistribution that occured in the concrete cells nearest to the support.

Severe bending was detected in the bottom steel plate at the support vicinity. This bending must be considered in the formulation of a successful design criteria.

The following is recommended for future work:

a) Extension of the proposed model to three dimensions. The current model supports plane stress, plane strain, and axisymmetric boundary conditions. For punching shear in extremely localized areas, and to determine the additional load capacity due to the surrounding slab, a full three dimensional analysis is recommended.

b) Evaluation of confinement effects on the compressive fracture energy. As indicated by Pramono and Willam (1990), a relatively small increase in confinement dramatically increases the compressive fracture energy. More research is required in this area.

c) Evaluation of concrete triaxial behaviour for high strength concretes. The predictions for the TF series, which were subjected to significant longitudinal compressive loads, were somewhat less successful than those of the CF series. This may have been due to the overestimation of confinement effects.

d) A numerical parametric study of composite walls comprised of various structural configurations and loadings. Such a study could be useful in determining optimal designs for various offshore conditions. In addition, the visualization of the flow of forces in the model could provide the designer with adequate guidance in the selection of an appropriate truss model to determine the ultimate loading.

REFERENCES

Adams, P.F., and Zimmerman, T.J.E. (1987). Design and Behavior of Composite Ice Resisting Walls. POAC '87, 9th International Conference on Port and Ocean Engineering under Arctic Conditions, pp. 23-40.

Adams, P.F. (1987). Steel/Concrete Composite Structural Systems. POAC '87, 9th International Conference on Port and Ocean Engineering under Arctic Conditions, pp. 1-2.

American Concrete Institute (1982). State of the Art Report on Finite Element Analysis of Reinforced Concrete. ASCE, 545 p.

Balakrishnan, S. and Murray, D.W. (1986). Finite Element Prediction of Reinforced Concrete Behaviour. Structural Engineering Report No. 138, Department of Civil Engineering, University of Alberta, Edmonton, Canada, 487 p.

Bangs, A.S. (1988). Techniques for the Analysis and Design of Composite Icewalls for Arctic Offshore Structures. Master of Engineering report, Texas A. and M. University, May, 60 p.

Bangs, A.S., and Machemehl, J.L. (1989). Composite Icewall Analysis and Design. Journal of Cold Regions Engineering, v. 3, No. 1, pp. 1-22.

Bathe, K.J. (1982). Finite Element Procedures in Engineering Analysis. Prentice Hall, 733 p.

Bathe, K.J., and Chaudhary, A. (1985). A Solution Method for Planar and Axisymmetric Contact Problems. International Journal for Numerical Methods in Engineering, v. 21, pp. 65-88.

Bazant, Z.P. and Oh, B.H. (1983). Crack Band Theory for Fracture of Concrete. Materiaux et Constructions, v. 16, No. 93, pp. 155-177.

Bazant, Z.P. (1984). Microplane Model for Strain-Controlled Inelastic Behaviour. Mechanics of Engineering Materials, C.S. Desai and R.H. Gallagher, eds., John Wiley and Sons, Inc., pp. 45-59.

Bazant, Z.P., and Prat, P.C. (1988). Microplane Model for Brittle-Plastic Material: I. Theory. Journal of Engineering Mechanics, ASCE, October, pp. 1672-1688.

Bazant, Z.P., and Prat, P.C. (1988). Microplane Model for Brittle-Plastic Material: II. Verification. Journal of Engineering Mechanics, ASCE, October, pp. 1689-1702.

Bazant, Z.P., and Ozbolt, J. (1990). Nonlocal Microplane Model for Fracture, Damage, and Size Effect in Structures. Journal of Engineering Mechanics, ASCE, November, pp. 2485-2505.

Canadian Standards Association (1984). CSA Standard CAN3-A23.3-M84 - Design of Concrete Structures for Buildings, Canadian Standards Association.

Canadian Standards Association (1989). CSA Standard S474-M1989 - Concrete Structures - Part iv of the Code for Design, Construction, and Installation of Fixed Offshore Structures, Canadian Standards Association.

Chen, W.F. (1982). Plasticity in Reinforced Concrete. McGraw-Hill, 474 p.

Chen, W.F., and Yamaguchi, E. (1985). On Constitutive Modelling of Concrete Materials. Seminar on Finite Element Analysis of Reinforced Concrete Structures, Tokyo, Japan, Society for the Promotion of Science, Tokyo.

Corder, P.R., and Wang, C.Y. (1990). Analysis of the Composite Icewall. Offshore and Arctic Operations Symposium, Jan., New Orleans, USA, ASME PD v. 29, p. 21-39.

Darwin, D., and Pecknold, D.A. (1974). Inelastic Model for Cyclic Biaxial Loading of Reinforced Concrete. Civil Engineering Studies, SRS No. 409, University of Illinois at Urbana-Champaign, Urbana, Illinois, July, 169 p.

De Borst, R. (1984). Application of Advanced Solution Techniques to Concrete Cracking and Non-Associated Plasticity. Numerical Methods for Non-Linear Problems, C. Taylor et. al. eds., v. 2, Pineridge Press, Swansea, United Kingdom, pp. 314-325.

De Borst, R. (1987). Computation of Post-Bifurcation and Post Failure Behaviour of Strain-Softening Solids. Computers and Structures, v. 25, pp. 211-224.

Desai, C.S., Zaman, M.M., Lightner, J.E., and Siriwardane, A.J. (1984). Thin-Layer Element for Interfaces and Joints. International Journal for Numerical and Analytical Methods in Geomechanics, v. 8, pp 19-43.

Elwi, A.E., and Murray, D.W. (1979). A 3D Hypoelastic Concrete Constitutive Relationship. Journal of Engineering Mechanics, ASCE, v. 105, pp. 623-641.

Elwi, A.E., and Murray, D.W. (1980). Nonlinear Analysis of Axisymmetric Reinforced Concrete Structures. Structural Engineering Report No. 87, Department of

Civil Engineering, University of Alberta, Edmonton, Alberta, Canada.

Elwi, A.E. (1990). SINAAPS Users Manual, Version 2.0. Center for Frontier Engineering Project Report 86-06, Edmonton, Alberta, Canada.

Gerwick, B.C., and Berner, D. (1987). Sandwich Composite Design - An Emerging Field. POAC '87 - 9th International Conference on Port and Ocean Engineering under Arctic Conditions, pp. 3-9.

Gopalaratnam, V.S., and Shah, S.P. (1985). Softening Response of Plain Concrete in Direct Tension. ACI Journal, May-June, pp.310-323.

Hassinen, P., Kouhi, J., Zimmerman, T.J.E., and Stephens, M.J. (1989). Static and Cyclic Load Tests of a Composite Ice-Resisting Wall. Report No. 965, Technical Research Center of Finland.

Herrman, L.R. (1978). Finite Element Analysis of Contact Problems. Journal of Engineering Mechanics, ASCE, v. 104 (EM5), pp.1043-1057.

Hillerborg, A., Modeer, M., and Petersson, P.E. (1976). Analysis of Crack Formation and Crack Growth in Concrete by Means of Fracture Mechanics and Finite Elements. Cement and Concrete Research, v. 6, pp. 773-782.

Katona, M.G. (1983). A Simple Contact-Friction Interface Element with Applications to Buried Culverts. International Journal for Numerical Methods in Geomechanics, v. 7, pp. 371-384.

Kemp, K.O., and Al-Safi, M.T. (1981). An Upper Bound Rigid Plastic Solution for the Shear Failure of Concrete

Beams Without Shear Reinforcement. Magazine of Concrete Research, v. 33, No. 115, June, pp. 96-102.

Kennedy, S.J., and Cheng, J.J. (1987). Behaviour of Transversely Loaded Continuous Steel-Concrete Composite Plates. Structural Engineering Report No. 150, Department of Civil Engineering, University of Alberta, Edmonton, Alberta, Canada, 239 p.

Kotsovos, M.D., and Newman, J.B. (1977). Behaviour of Concrete Under Multiaxial Stresses. ACI Journal, Proceedings, v. 74, No. 9, Sept., pp.443-446.

Kupfer, H., Hilsdorf, H.K., and Rusch, H. (1969). Behaviour of Concrete under Biaxial Stresses. ACI Journal, v. 66, No. 8, August, pp. 656-666.

Link, R.A., Elwi, A.E., and Scanlon, A. (1989). Biaxial Tension Stiffening Due to Generally Oriented Reinforcing Layers. Journal of Engineering Mechanics, ASCE, v. 115, No. 8, August, pp. 1647-1662.

Link, R.A., and Elwi, A.E. (1990). Localization and Mesh Dependency in Concrete under Compression. Proceedings, CSCE Annual Conference, Hamilton, Ontario, pp. .

MacGregor, J.G. (1988). Unpublished communication.

MacGregor, J.G. (1988). Reinforced Concrete Mechanics and Design. Prentice Hall, 799 p.

Massicotte, B., Elwi, A.E., and MacGregor, J.G. (1990). Tension Stiffening Model for Planar Reinforced Concrete Members. Journal of Structural Engineering, ASCE, v. 116, No. 11, pp. 3039-3058.

Matsuishi, M., Nishimaki, H., Takeshita, H., Iwata, S., and Subara, T. (1978). On the Strength of Composite

Steel-Concrete Structures of a Sandwich System (2nd report) - Nonlinear Analysis Using the Finite Element Method. Hitachi Zosen Technical Review, v. 39, No. 1, March, pp. 26-35.

Matsuishi, M., and Iwata, S. (1987). Strength of Composite Sandwich System Ice-Resisting Structures. POAC '87 - 9th International Conference on Port and Ocean Engineering under Arctic Conditions, pp. 59-70.

Neilsen, M.P. and Braestrup, M.W. (1978). Shear Strength of Prestressed Concrete Beams Without Web Reinforcement. Magazine of Concrete Research, v. 30, No. 104, Sept., pp. 119-128.

Neilsen, M.P. (1984). Limit Analysis and Concrete Plasticity. Prentice Hall.

Nojiri, Y., and Koseki, K. (1986). Structural Behaviour and Design Method of Steel/Concrete Composite Ice Walls for Arctic Offshore Structures. Offshore Technology Conference, Houston, Texas, May 5-8, Paper No. 5292, 8 p.

O' Flynn, B. (1987). Composite Ice-Resisting Walls. Ph.D. Thesis, University of Alberta, Edmonton, Alberta, Canada.

Owen and Hinton (1985). Plasticity in Finite Elements. McGraw-Hill.

PDA Engineering (1991). PATRAN Plus Users Manual. PDA Engineering.

Pramono, E., and Willam, K. (1989). Fracture Energy-Based Plasticity Formulation of Plain Concrete. Journal of Engineering Mechanics, ASCE, Nov., pp. 1183-1204.

Ramm, E. (1980). Strategies for Testing Nonlinear Response Near Limit Points. Europe-U.S. Workshop on Nonlinear Finite Element Analysis in Structural Mechanics, Bochum, U.S.

Ramm, E., and Kompfner, T.A. (1984). Reinforced Concrete Shell Analysis Using an Inelastic Large Deformation Finite Element Formulation. Proceeding of the International Conference on Computer Aided Analysis and Design of Concrete Structures, Split, Yugoslavia, pp. 581-598.

Rogowsky, D., and MacGregor, J.G. (1983). Shear Strength of Deep Reinforced Concrete Continuous Beams. Structural Engineering Report No. 110, Department of Civil Engineering, University of Alberta, Edmonton, Alberta, Canada.

Rots, J.G., Nauta, P., Kusters, G.M.A., and Blaauwendraad (1985). Smeared Crack Approach and Fracture Localization in Concrete. Heron, v. 30, No. 1, Delft University of Technology, The Netherlands.

Sanderson, T.J.O. (1988). Ice Mechanics - Risks to Offshore Structures. Graham and Trotman Limited, 253 p.

Stephens, M.J., and Zimmerman, T.J.E. (1990). The Strength of Composite Ice Resisting Walls Subjected to Combined Loads. Proceedings of the European Offshore Mechanics Symposium (EUROMS-90), Trondheim, Norway, August.

Truesdell, C. (1955). Hypo-elasticity. Journal of Rational Mechanics and Analysis. v. 4, 1955, pp. 83-133.

Wang, P.T., Shah, S.P., and Naaman, A.E. (1978). Stress-Strain Curves of Normal and Lightweight Concrete in Compression. ACI Journal, Nov., pp. 603-611.

Willam, K.J., and Warnke, E.P. (1975). Constitutive Model for Triaxial Behaviour of Concrete. IABSE Seminar on Concrete Structures Subjected to Triaxial Stresses, ISMES, Bergamo, Italy, IABSE Proceedings, v. 19.

Zsutty, T. (1968). Beam Shear Strength Prediction by Analysis of Existing Data. ACI Journal, v. 65, Nov.

Zimmerman, T.J.E. (1988). Private communication.

APPENDIX A - CONCRETE CYLINDER PARAMETRIC STUDY

As mentioned in Section 3.2.7, concrete compressive softening has been found to be dependent both numerically and experimentally upon specimen size. It is therefore necessary to adjust the finite element input descending branch to account for strain localization in compression as well as tension. Values for fracture energy in tension are commonplace, but crushing energies have yet to be evaluated for different concrete strengths.

Ideally, the energy of crushing, G_{cr}, should be obtained from a uniaxial test. Unfortunately, there are few uniaxial tests for which G_{cr} can be calculated. The common cylinder test is not uniaxial because of confinement effects and the load redistribution caused by longitudinal cracking.

A typical uniaxial cylinder test consists of a concrete cylinder situated between a loading platform and a loading head. The descending portion of the stress-strain curve is obtained by using stroke control on the loading apparatus. This can either be achieved by using a very stiff loading apparatus (Wang, et al., 1978), or by using a load sharing device such as a steel jacket (Shah, et al., 1981). Sulfur plattens are placed on the ends of the cylinder to ensure a uniform bearing surface.

Figure A.1 shows a typical stress-strain curve obtained from a cylinder test. Up to the ultimate strength, there is little visible damage in the material. After peak stress, large volumetric expansion occurs near the cylinder midheight, and large radial cracks occur. The expansion and cracking, shown in Figure A.2, are due to the loss in circumferential stiffness, because the concrete has no tensile capacity in this direction at peak stress. In addition, there is a conical undamaged region at the end caps, which is induced by the confining effect of the end platens. The cracking and bulging causes significant load redistribution in the cylinder, resulting in somewhat higher stresses in this region (see Figure A.2).

It is obvious that the stress distribution in Figure A.2 is far from uniaxial. However, there is an abundance of test data for standard cylinders. Therefore, it is proposed that cylinders be used to obtain an estimate of G_{cr}.

The method for calculating G_{cr} is as follows. For a purely uniaxial test, if the crushing energy, G_{cr}, is a material constant, and the area under the descending branch, A_c, is constant for a given concrete and a given cylinder configuration, then the following relationship can be written relating G_{cr} to A_c

$$A_c = \alpha_c G_{cr}, \qquad [A.1]$$

where α_c is a proportionality constant. Multiplying and dividing the right hand side of Equation A.1 by the sampling point spacing, h_c, the relation between the input and output areas can be written as

$$A_c = \alpha_c h_c \left(\frac{G_{cr}}{h_c} \right) = \alpha_c h_c A_{cd}. \qquad [A.2]$$

Equation A.2 relates the input area, A_c, required for a finite element analysis to obtain the correct uniaxial output area, A_{cd}. However, since a concrete cylinder test is not truly uniaxial, Equation A.2 must be modified to account for nonlinear effects due to confinement and cracking. A power law of the form

$$A_c = (\alpha_c h_c A_{cd})^n \qquad [A.3]$$

is adopted to account for these effects. Equation A.3 can be rearranged to form

$$A_{cd} = \frac{(A_c)^{1/n}}{\alpha_c h_c}. \qquad [A.4]$$

But

$$A_{cd} = \frac{G_{cr}}{h_c}. \qquad [A.5]$$

When Equation A.5 is substituted into Equation A.4, the final form of G_{cr} is obtained as

$$G_{cr} = \frac{(A_c)^{1/n}}{\alpha_c} . \qquad [A.6]$$

It remains to obtain the parameters α_c and n. It is possible to calculate the two constants from a finite element parametric study of a series of cylinders.

Two series of standard cylinder tests at two different uniaxial concrete strengths, f'_c, have been analysed using FEPARCS (an acronym for the Finite Element Analysis of Reinforced Concrete Structures). In both series, the sampling point spacing, h_c, and the compressive input area, A_{cd}, have been varied. The output areas obtained from the analyses, A_c, are plotted against $A_{cd}h_c$. From this plot, which is a form of Equation A.4, a least squares fit can be performed to obtain the two constants, α_c and n.

Three different meshes with increasing mesh refinement were analysed. Figure A.3 shows the mesh configurations used in the study. The approximate sampling (Gauss point) spacings are 16.67 mm for the coarse mesh , 10.0 mm for the intermediate mesh, and 5.0 mm for the fine mesh. Figure A.4 shows the boundary conditions used in the analysis. Due to axisymmetric considerations, only one quarter of the cylinder need be modelled. The loading head of the cylinder was fixed to reflect no slip conditions due to friction along this surface. The top of the cylinder was constrained to move as a straight line to simulate the effect of a rigid loading head. Loading was stroke (displacement) controlled, and the total Lagrangian formulation was used to include any unloading effects due to large displacements.

Table 1 summarizes the values of all input parameters for the two series. Two different concrete strengths, 53.5 MPa and 30 MPa, were used to determine if the results were sensitive to concrete strengths. The two concrete strengths were used with four different input areas for each of the three meshes, totalling 24 different analyses in all. Figure A.5 shows the input stress-strain curves used in the analyses for compression and tension. A linear descending branch was used in all analyses to avoid complications.

Figures A.6 through A.8 show the average stress-strain curves obtained from the coarse, intermediate, and fine meshes respectively for $f_c' = 53.5$ MPa. All analyses were able to attain ultimate strength equivalent to f_c'. It is concluded that using f_c' from a cylinder test is acceptable for use in a finite element analysis. It is also observed that the area under the output stress-strain curve increases with increasing G_{cr}. Although not shown here, the same conclusions were evident for $f_c' = 30.0$ MPa.

Figure A.9 is a plot of the deformed shape of two cylinders near the end of the analysis. The cylinder with $f_c' = 53.5$ MPa had $h_c = 10$ mm, and $A_{cd} = 1.338$ MPa, while the cylinder with $f_c' = 30.0$ MPa had $h_c = 10$ mm, and $A_{cd} = 1.338$ MPa. Before the ultimate strength is reached, little lateral bulging was observed in the cylinder. After the ultimate strength was reached, substantial central bulging was noticed. In addition, strain localization is present in these cylinders, as observed as localized deformation in the central region.

Figure A.10 shows the damaged regions for the cylinders described above. It is noted that there are vertical radial cracks along the length of the member, as evidenced by the diamond shapes. Softening appears to be uniformly distributed along the specimen length, and a conical undamaged region exists near the ends of the specimens.

From the above discussion, it is concluded that the finite element model is an adequate representation of concrete cylinder failures. Therefore, the results can be used in the determination of G_{cr}.

Figure A.11 is a plot of A_c versus h_cA_{cd}. A least squares fit of the data resulted in the following values for the constants α_c and n

$$\alpha_c = 0.00478, \tag{A.7a}$$

$$n = 0.80. \qquad [A.7b]$$

Substituting Equations A.7a and b into A.6 results in the final form of G_{cr}

$$G_{cr} = 209.2A_c^{1.25}. \qquad [A.8]$$

The crushing energy, G_{cr}, can now be determined by obtaining the area under the descending branch of a concrete cylinder.

Series	Strength (MPa)	Mesh h_c	Input Areas , A_{cd}
1	53.5	16.67, 10.0, 5.0	0.334, 0.669, 1.003, 1.338
2	30	16.67, 10.0, 5.0	0.375, 0.750, 1.125, 1.500

Table A.1 Input parameters for mesh refinement study

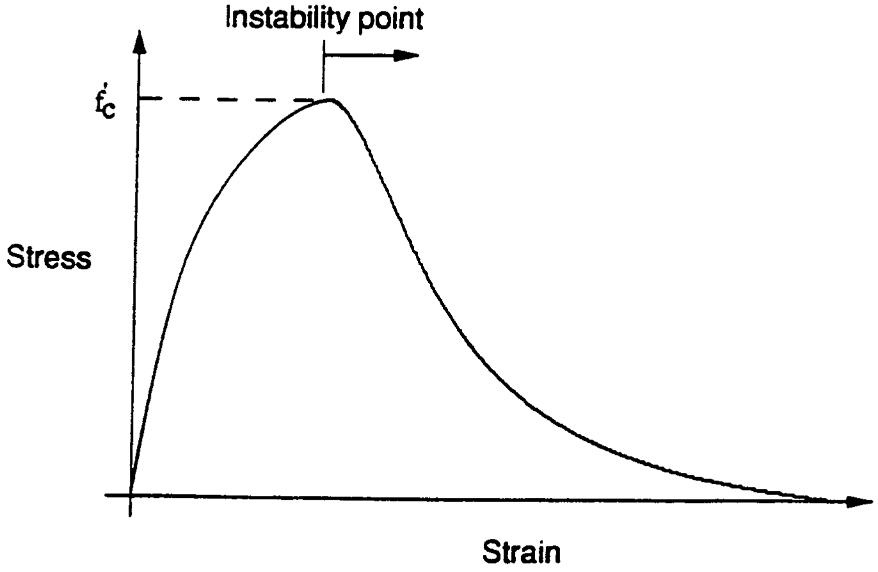

Figure A.1 Concrete compressive stress-strain curve

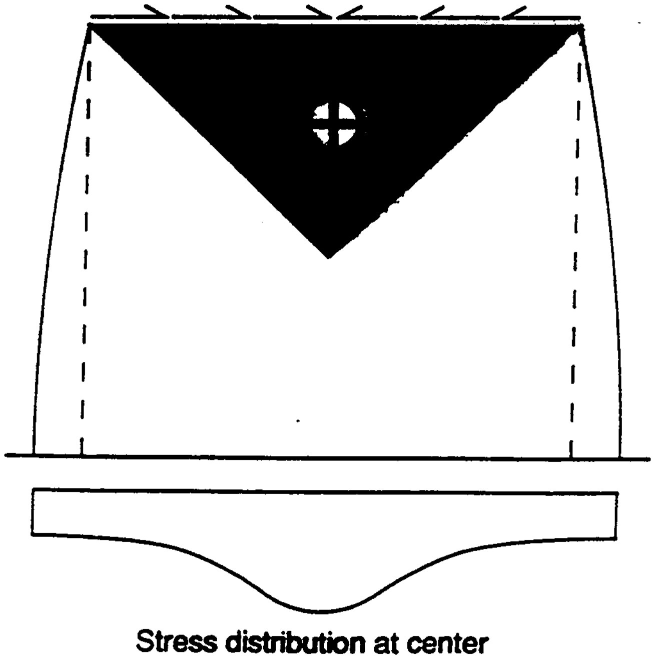

Figure A.2 Confinement and deformation effects

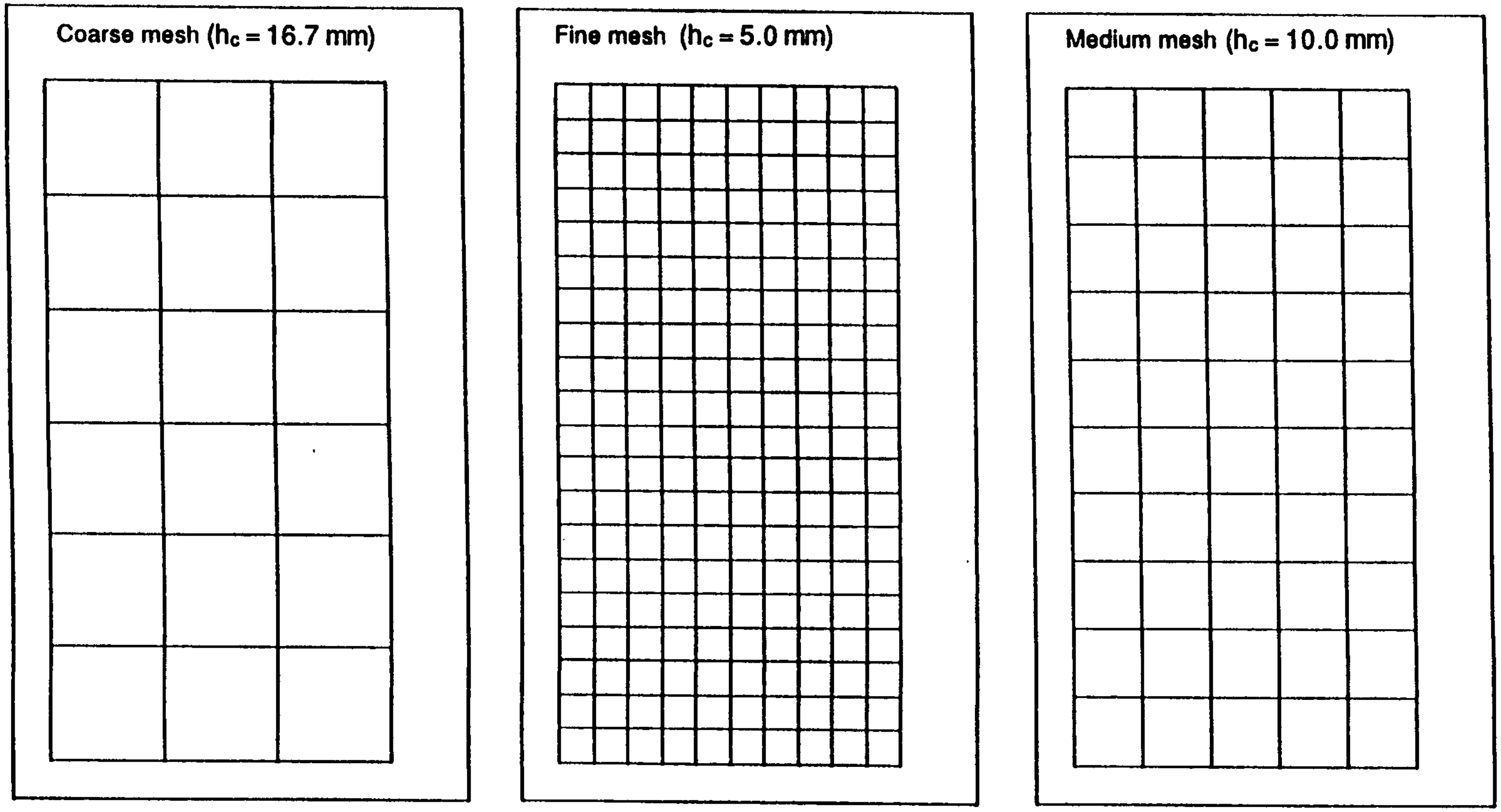

Figure A.3 Parametric study meshes

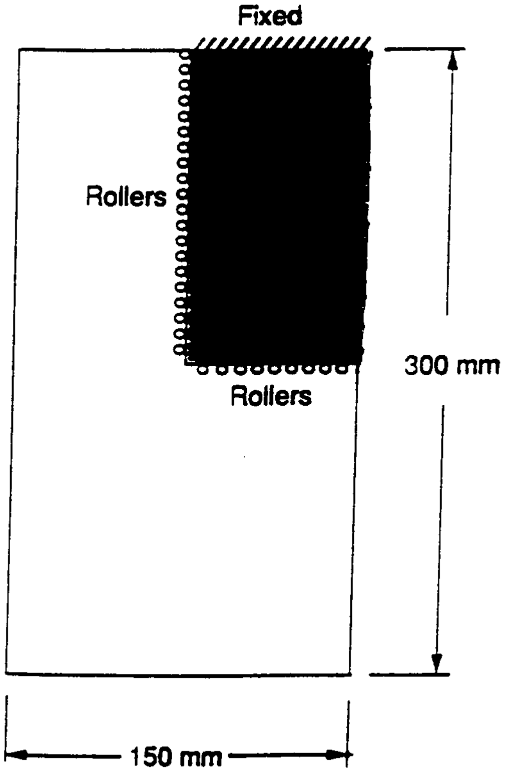

Figure A.4 Cylinder boundary conditions

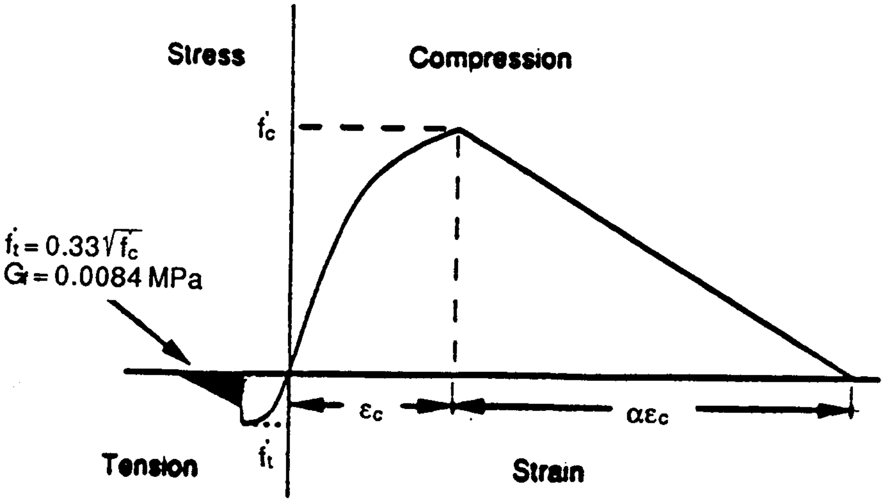

Figure A.5 Input stress strain curve

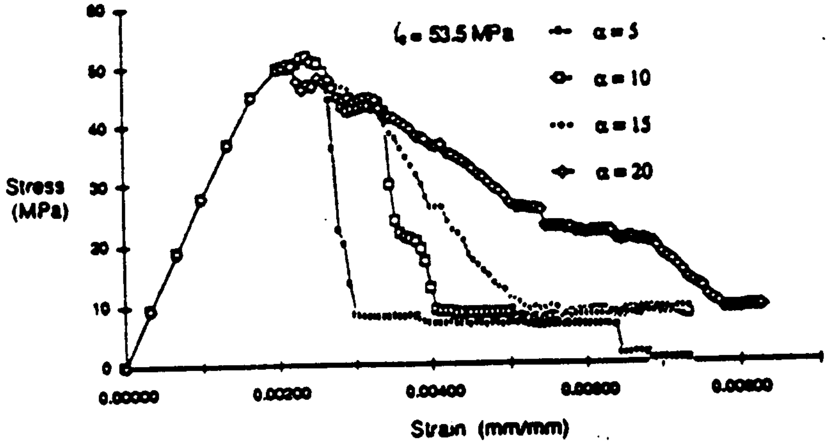

Figure A.6 Stress strain curves for coarse mesh

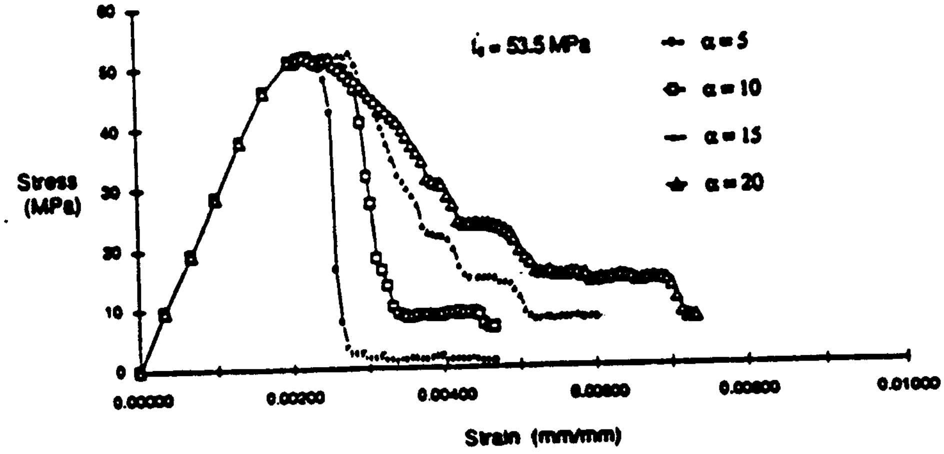

Figure A.7 Stress strain curves for intermediate mesh

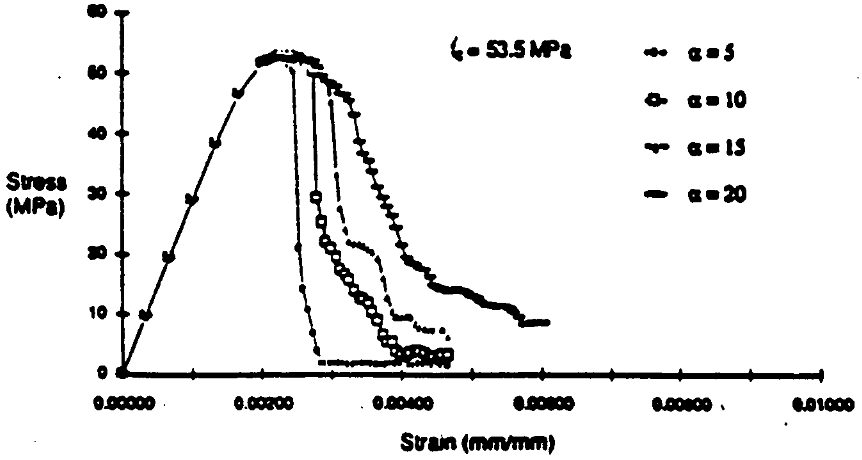

Figure A.8 Stress strain curves for fine mesh

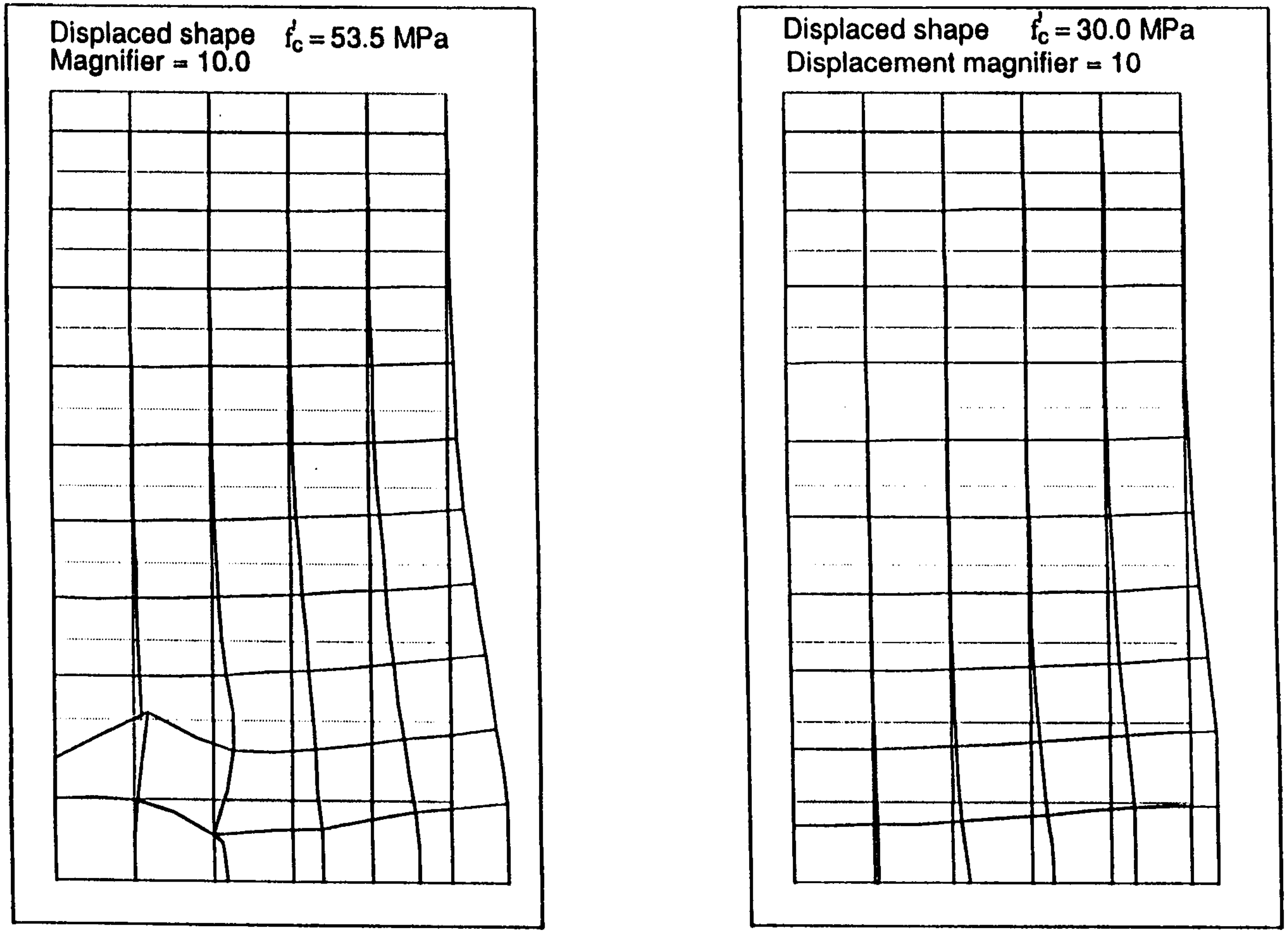

Figure A.9 Cylinder deflected shapes

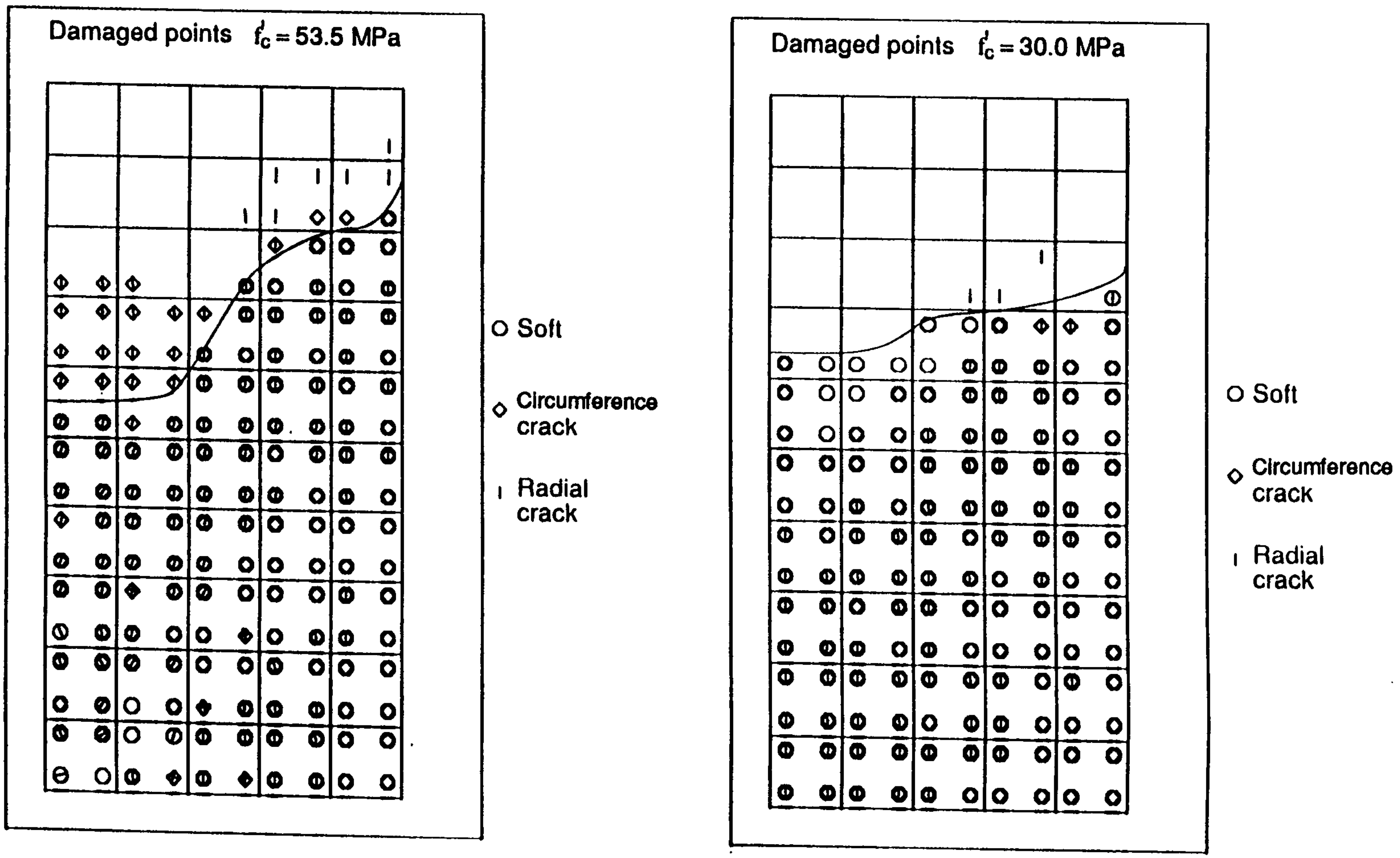

Figure A.10 Cylinder nonlinear effects

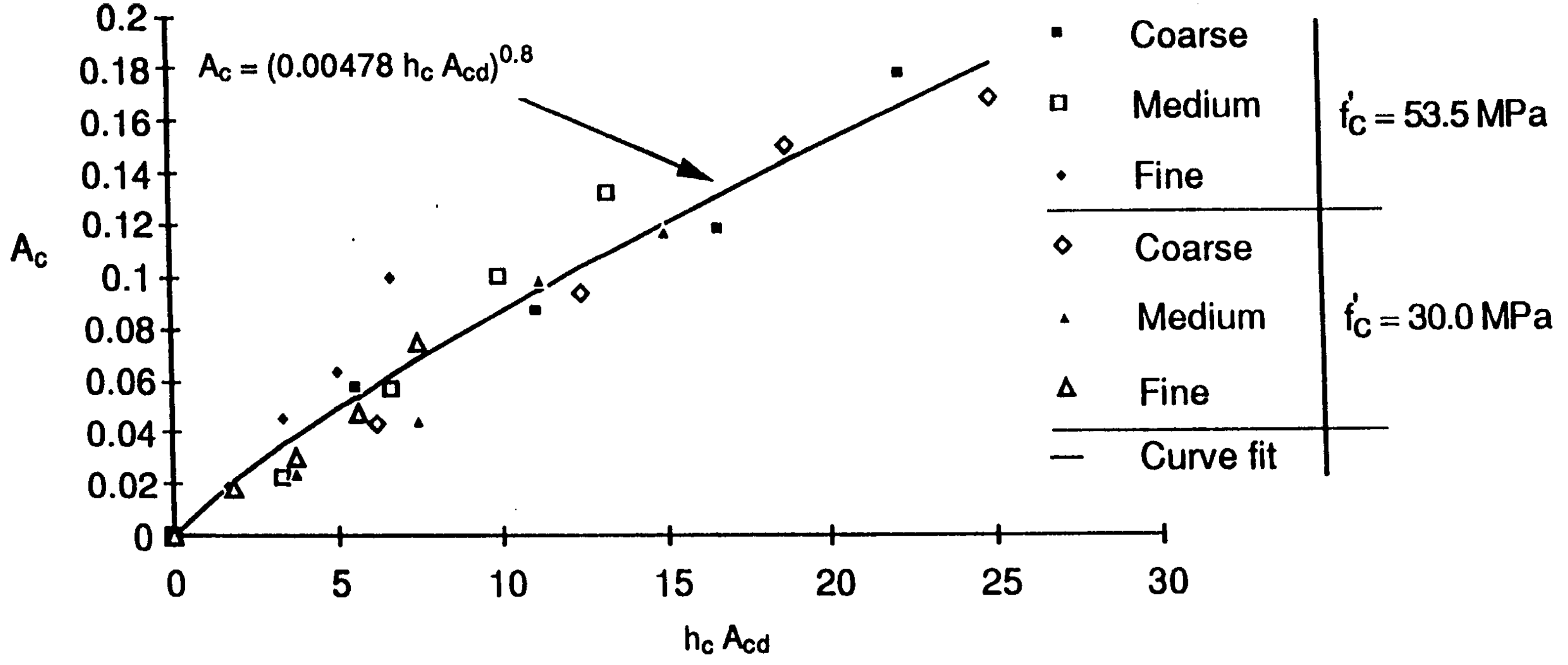

Figure A.11 Curve fit for A_c

RECENT STRUCTURAL ENGINEERING REPORTS

Department of Civil Engineering
University of Alberta

153. *Compressive Behavior of Gusset Plate Connections* by S.Z. Hu and J.J. Cheng, July 1987.

154. *Development of Structural Steel Design Standards* by P.J. Marek and D.J.L. Kennedy, October 1987.

155. *Behaviour of Bolted Joints of Corrugated Steel Plates* by R.W.S. Lee and D.J.L. Kennedy, January 1988.

156. *Masonry Veneer Wall Systems* by W.M. McGinley, J. Warwaruk, J. Longworth and M. Hatzinikolas, January 1988.

157. *Stability of Concrete Plates* by A.O. Aghayere and J.G. MacGregor, February 1988.

158. *The Flexural Creep Behaviour of OSB Stressed Skin Panels* by P.C.K. Wong, L. Bach and J.J. Cheng, April 1988.

159. *Ultimate Strength of Eccentrically Loaded Fillet Welded Connections* by D.F. Lesik and D.J.L. Kennedy, May 1988.

160. *Fatigue Strength of Coped Steel Beams* by M.C.H. Yam and J.J. Cheng, June 1988.

161. *Analysis of Concrete Panels* by B. Massicotte, A.E. Elwi and J.G. MacGregor, July 1988.

162. *Behavior and Design of Reinforced Concrete Ice-Resisting Walls* by R.M. Ellis and J.G. MacGregor, November 1988.

163. *An Analysis of the Performance of Welded Wide Flange Columns* by D.E. Chernenko and D.J.L. Kennedy, December 1988.

164. *Nonlinear Dynamic Analysis of Caisson-Type Offshore Structures* by I.R. Soudy and T.M. Hrudey, March 1989.

165. *NORCO - A Program for Nonlinear Finite Element Analysis of Reinforced Concrete Structures - Users' Manual* by S. Balakrishnan, A.E. Elwi and D.W. Murray, April 1989.

166. *An Eigenvector-Based Strategy for Analysis of Inelastic Structures* by J. Napoleao, Fo., A.E. Elwi and D.W. Murray, May 1990.

167. *Elastic-Plastic and Creep Analysis of Casings for Thermal Wells* by S.P. Wen and D.W. Murray, May, 1990.

168. *Erection Analysis of Cable-Stayed Bridges* by Z. Behin and D.W. Murray, September 1990.

169. *Behavior of Shear Connected Cavity Walls* by P.K. Papanikolas, M. Hatzinikolas and J. Warwaruk, September 1990

170. *Inelastic Transverse Shear Capacity of Large Fabricated Steel Tubes,* by K.H. Obaia, A.E. Elwi and G.L. Kulak, April 1991.

171. *Fatigue of Drill Pipe* by G.Y. Grondin and G.L. Kulak, April 1991.

172. *The Effective Modulus of Elasticity of Concrete in Tension* by Atif F. Shaker and D.J. Laurie Kennedy, April 1991.

173. *Slenderness Effects in Eccentrically Loaded Masonry Walls* by Muqtadir, Mohammad A., Warwaruk, J. and Hatzinikolas, M.A., June 1991.

174. *Bond Model For Strength of Slab-Column Joints* by Scott D.B. Alexander and Sidney H. Simmonds, June 1991.

175. *Modelling and Design of Unbraced Reinforced Concrete Frames* by Yehia K. Elezaby and Sidney H. Simmonds, February 1992.

176. *Strength and Stability of Reinforced Concrete Plates Under Combined Inplane and Lateral Loads* by Mashhour G. Ghoneim and James G. MacGregor, February 1992.

177. *A Field Study of Fastener Tension in High-Strength Bolts* by G.L. Kulak and K. H Obaia, April 1992.

178. *The Flexural Behaviour of Concrete-Filled Hollow Structural Sections* by Yue Qing Lu and D.J. Laurie Kennedy, April 1992.

179. *Finite Element Analysis of Distributed Discrete Concrete Cracking* by Budan Yao and D.W. Murray, May 1992.

180. *Finite Element Analysis of Composite Ice Resisting Walls* by R.A. Link and A.E. Elwi, June 1992.